



TECHNISCHE
UNIVERSITÄT
WIEN

DIPLOMARBEIT

Electrochemical Properties of LiFePO₄ Thin-Film Electrodes

Ausgeführt am Institut für

Chemische Technologien und Analytik
der Technischen Universität Wien

unter der Anleitung von

Univ.-Prof. Dipl.-Phys. Dr. rer. nat. Jürgen FLEIG
Univ.-Ass. Andreas BUMBERGER, MSc.

durch

Matthias KOGLER, BSc.

Matrikel-Nr.: 01501652

Wien, November 2021

(Matthias Kogler)

Vorwort

„Ge Hiasi, das interessiert doch keinen. Sag lieber, du machst irgendwas mit Menschenrechten!“ (Gugel, 2020)

Liebe/r Leser*in!

Sollten Sie nach Erblicken des Titels die Meinung meines besten Freundes teilen und in der folgenden Arbeit lieber *Irgendwas über Menschenrechte* erfahren, muss ich Sie leider enttäuschen. Ihnen kann ich wärmstens die Hintergrundliteratur zur Problematik der Rohstoffgewinnung empfehlen. Menschenrechte spielen hier eine zentrale Rolle.

Bei all jenen, die sich nicht vom Thema haben abschrecken lassen, bedanke ich mich für das Interesse und wünsche viel Spaß bei der Lektüre. Möge sie aufschlussreich und lesenswert sein.

Apropos Bedanken! Natürlich ist diese Arbeit und insbesondere der Weg dahin nicht alleine zu bewältigen gewesen. Deshalb möchte ich diese Gelegenheit nutzen, mich bei Menschen zu bedanken, welche ihren Teil zu dem Projekt Studienabschluss beigetragen haben.

Als Erstes möchte ich mich bei Prof. Jürgen Fleig bedanken, der mir nicht nur diese Diplomarbeit in seiner Arbeitsgruppe ermöglichte, sondern auch in einem nicht unkomplizierten Jahr, stets Zeit für wichtigen Input zu meiner Arbeit gefunden hat.

Ein großer Dank gebührt Andreas Bumberger, ohne dessen Unterstützung es meine Arbeit in dieser Form nicht geben würde. Nicht nur inhaltlich, sondern auch optisch ohne all diese REM und TEM Aufnahmen, würden die folgenden Seiten ohne sein Zutun weit weniger ansprechend und informativ sein.

Weiters möchte ich Joseph Ring danken, der nicht nur den Büroalltag weitaus angenehmer gestaltet hat, sondern mir auch bei allen möglichen Problem hilfsbereit zur Seite gestanden ist.

Darüber hinaus möchte ich mich bei der gesamten Arbeitsgruppe dafür bedanken, dass in einem Jahr, geprägt von Abstandsregeln und Masken, ein angenehme und unterstützende Zusammenarbeit möglich war.

Selbstverständlich gibt es auch außerhalb des universitären Umfelds Menschen, denen ich für ihre Unterstützung, ihre Freundschaft dankbar bin.

Nici, leider habe ich kein passendes, gesellschaftstaugliches Zitat gefunden. Du musst dich also mit der bloßen Erwähnung zufrieden geben. Danke für die unzähligen Jahre Freundschaft!

Natürlich darfst auch du, Nina, nicht fehlen. Gerade am Anfang des Studiums haben die vielen Gespräche über Gott und die Welt, ob in der WG oder auf Wandertag, geholfen, anstrengende und nervenaufreibende Zeiten zu überstehen.

Ich möchte mich außerdem bei all jenen bedanken, die die Zeit meines Studiums mit ihrer Freundschaft bereichert haben, auch wenn sie vielleicht nur einen Teil des Weges mit mir gegangen sind. Trotz der Veränderungen die es gebracht, trotz der Nerven die es gekostet hat, bin ich dankbar für alles, was das letzte Jahr mir beschert hat.

Zum Schluss noch ein Wort an die Familie. Diese kann man sich bekanntlich nicht aussuchen, besonders nicht die Schwester. Ich glaube, ich hätte es aber weitaus schlimmer treffen können. Danke, dass du mich als Bruder aushältst!

Den größten Dank möchte ich an meine Eltern richten. Nicht nur als Hauptsponsoren, sondern auch als Unterstützer in jeglicher Hinsicht haben sie meine Studium in dieser Form erst möglich gemacht.

Abstract

Whether as stationary storage device or as a vehicle battery, since its first introduction in 1997 by Padhi et al, LiFePO_4 (LFP) has established itself as an environmentally benign and cost-effective alternative to conventional cathode materials (e.g. LiCoO_2) in the sector of lithium-ion batteries. These benefits, however, are countered by comparatively low performance figures, which can be ascribed to poor electronic and ionic transport properties. Although intrinsic characteristics of this nature are disadvantageous for commercial application, they do allow for a detailed examination of the fundamental diffusion kinetics.

In order to generate a system suitable for investigating the transport processes, LFP thin-films were deposited on various single-crystal substrates by means of RF magnetron sputtering, whereby the optimisation of the deposition process played a key role. Structural techniques were used to characterise the layers in terms of texture and morphology, and selected thin-film electrodes were subsequently investigated electrochemically.

LFP thin-films were successfully prepared on SrTiO_3 (STO) (100) single-crystals, hence Nb:STO (100) was used as an electrically conductive substrate. However, the formation of a porous interlayer caused by interdiffusion of strontium and iron during the deposition was observed, which led to an impairment of the investigations in cross-plane geometry. This was counteracted on the one hand by changing the measurement geometry to in-plane and on the other hand by applying a buffer layer.

In-plane impedance measurements at temperatures up to 450 °C allowed a separate investigation of electronic and ionic transport properties, with results obtained being congruent with the literature.

By applying a $\text{LaNi}_{0.5}\text{Co}_{0.5}\text{O}_3$ (LNCO) layer between Nb:STO and LFP, an electrochemically active LFP thin-film electrode could be characterised for the first time, which showed reversible behaviour in cyclic voltammetry experiments. This result serves as an essential reference point for further research in this field.

Kurzfassung

Ob als stationärer Speicher oder als PKW-Batterie, LiFePO_4 (LFP) hat sich seit der ersten Erwähnung 1997 durch Padhi et. al als umweltfreundliche und kostengünstige Alternative zu konventionellen Kathoden-Materialien (z.B. LiCoO_2) im Bereich der Lithium-Ionen Batterien etabliert. Den Vorteilen stehen jedoch vergleichsweise geringe Leistungsdaten gegenüber, welche auf schlechte elektronische und ionische Transporteigenschaften zurückzuführen sind. Wenngleich sich intrinsische Merkmale dieser Art nachteilig auf eine kommerzielle Nutzung auswirken, so ermöglichen sie jedoch eine detaillierte Betrachtung der zugrundeliegenden Diffusionskinetik.

Um nun ein geeignetes System für die Untersuchung der Transport-Prozesse zu generieren, wurden LFP Dünnschichten mittels RF Magnetron Sputtering auf verschiedenen Einkristall-Substraten abgeschieden, wobei die Optimierung des Herstellungsprozesses eine zentrale Rolle einnahm. Mit Hilfe struktureller Methoden wurden die Schichten hinsichtlich Textur und Morphologie charakterisiert und ausgewählte Dünnschichtelektroden in weiterer Folge elektrochemisch untersucht.

LFP Dünnschichten wurden erfolgreich auf SrTiO_3 (STO) (100) Einkristallen hergestellt, weshalb Nb:STO (100) als elektrisch leitendes Substrat zur Anwendung kam. Hierbei konnte jedoch die Bildung einer porösen Zwischenschicht, verursacht durch Interdiffusion von Strontium und Eisen während der Abscheidung, beobachtet werden, was zu einer Beeinträchtigung der Untersuchungen in Cross-Plane Geometrie führte. Dem konnte einerseits durch Wechsel der Messgeometrie auf In-Plane und andererseits durch den Einsatz einer Pufferschicht entgegengewirkt werden.

In-Plane Impedanzmessungen bei Temperaturen bis $450\text{ }^\circ\text{C}$ haben eine separate Betrachtung von elektronische und ionische Transporteigenschaften ermöglicht, wobei die erhaltenen Ergebnisse mit der Literatur kongruent sind. Durch Applizierung einer $\text{LaNi}_{0.5}\text{Co}_{0.5}\text{O}_3$ (LNCO) Schicht zwischen Nb:STO und LFP konnte erstmals eine elektrochemisch aktive LFP Dünnschichtelektroden charakterisiert werden, welche bei Untersuchungen mittels Zyklovoltammetrie reversibles Verhalten zeigte. Dieses Resultat dient als essentieller Ausgangspunkt für weiterführende Forschung auf diesem Gebiet.

Contents

Vorwort	i
Abstract	iii
Kurzfassung	iv
1 Introduction	1
1.1 Lithium-Ion Batteries	2
1.2 Olivine-type LiFePO ₄	5
1.3 Motivation and Aim	9
2 Theoretical Background	10
2.1 Electrochemical Impedance Spectroscopy	10
2.1.1 Randles Circuit	13
2.1.2 Transmission Line	14
2.2 Radio-Frequency Magnetron Sputtering	15
2.3 Contact Resistance of Pt/Nb:STO	17
3 Experimental Methods	18
3.1 Introduction.	18
3.2 Preparation of LiFePO ₄ Thin-Films.	18
3.2.1 Sapphire.	20
3.2.2 STO	21
3.2.3 Nb:STO	22
3.2.4 Conductive Coatings	23
3.2.5 Alternative Conductive Substrates	26
3.3 Structural Characterisation.	28
3.4 Electrochemical Characterisation	29
3.4.1 Liquid Cell	30
3.4.2 Microcontact Setup	33

4	Results and Discussion	37
4.1	Structural Evaluation	37
4.1.1	Sapphire.	37
4.1.2	STO	40
4.1.3	Nb:STO	52
4.1.4	SRO/LNCO	55
4.1.5	Alternative Conductive Substrates	61
4.1.6	Cross-Section Analysis.	64
4.2	Conclusion of the Thin-Film Preparation	70
4.3	Electrochemical Characterisation	71
4.3.1	Liquid Cell	71
4.3.2	Microcontact Setup	76
5	Conclusion	84
	List of Abbreviations	86
	List of Figures	88
	List of Tables	93
	Bibliography	94

1 Introduction

Overcoming the climate crisis is one of most demanding challenges modern society has to deal with. Impacts of global warming, for instance droughts, floods and other weather extremes are piling up and with the past five years being the warmest since recording, the European Green Deal is the top political priority. In order to achieve the ambitious goal to become climate neutral by 2050, several measures were set in place. [1] These include investments in the areas of renewable energy and energy efficiency as well as the reduction of greenhouse gas emissions (GHG) by at least 55% by 2030 compared to 1990 levels. In 2021, a further step was taken to treat these targets as obligations rather than ambitions with the introduction of the package of proposals called "fit for 55". [2] The focus of action lies, among others, on the transport sector, as greenhouse gas emissions from this segment have not followed the general trend of decreasing emissions. According to the European Environment Agency, transport was responsible for one third of greenhouse gas emissions in 2017, with road transport accounting for the largest share (around 72 %). [3, 4] In order to pursue decarbonisation of this sector, electrification of transport will therefore be of crucial importance.

Despite the large contribution of this sector, the largest source of GHG emissions in the EU is the power sector, which therefore needs to be given greatest attention. The key to reducing emissions and ultimately establishing a carbon-neutral European energy system are renewable energy sources. However, the variability of some renewables, e.g. wind and solar power, and their dependence on time of day, the seasons and the weather, leads to the difficulty that electricity is generated when the resource is available, but not necessarily when electricity is needed. Therefore, these challenges require a solution to balance supply and demand in an efficient and cost-effective way. [5] One possible way to address these difficulties is through smart energy storage systems. On the one hand, they are capable of compensating these intermittencies of renewable energies and, on the other hand, they can play an important role in the decarbonisation of other economic sectors. [6]

Storage can take place using several different systems with different underlying principles (mechanical, thermal, chemical, electrical and electrochemical). Although pumped hydro storage, as a mechanical approach, accounts for a major share with 97 % in 2017, other technologies, especially those linked to the increase of renewable energies, are on the rise.

In fact, one of the most promising and emerging storage solutions, which is also of great importance in the process of electrification of the transport sector, is of an electrochemical nature: batteries. [6] With the increasing demand of electric vehicles (EVs), home storage devices, grid-scale storage solutions etc., batteries are expected to play an important role in the approach of the energy question. As a result of these developments, the production costs of electric vehicle batteries are expected to reduce dramatically by 2030, which is presumably going to provide an additional boost towards meeting the targets specified by the European Commission in the "Strategic Action Plan for Batteries". [7, 8]

1.1 Lithium-Ion Batteries

In general, a battery, consisting of multiple electrochemical cells, is a device that converts chemical energy to electrical energy, or vice versa, using redox reactions. [9] The main representatives and the fastest growing battery technologies are lithium-ion batteries (LIBs). Since Sony commercialised the first LIB in 1991 [10], research has come a long way to improve the performance of the electrochemical cells. Although materials and properties have evolved, LIBs, then and now, consist of largely four components: two electrodes (anode and cathode), electrolyte and separator. The exact mechanism during the charge/discharge process differs slightly depending on the materials used, but the fundamental working principle can be explained as depicted in figure 1.1.

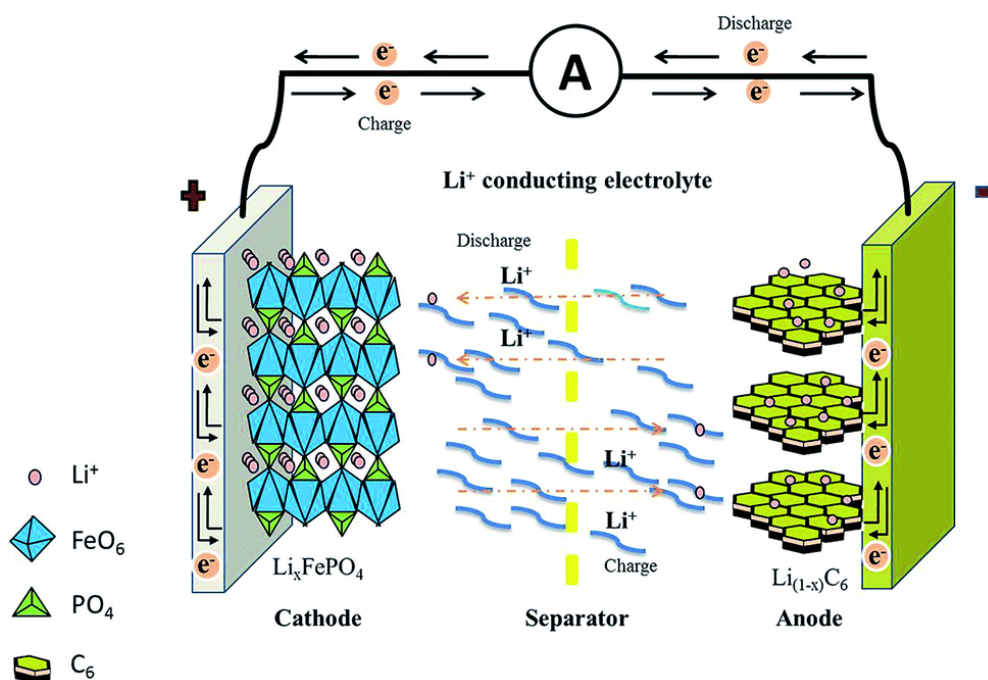
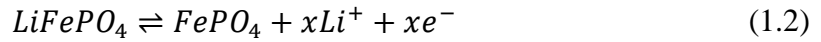


Figure 1.1: Schematic illustration of a typical lithium-ion battery. [11]

When the cell is at discharge state, all of the Li^+ -ions are found in the positive electrode i.e. the cathode (e.g. Li_1FePO_4), while the anode (e.g. graphite C) is empty. At this point, it has to be mentioned that the nomenclature of the electrodes (i.e. cathode and anode) are defined for the discharge process and are thus also maintained for the charge process. During charging Li^+ -ions originating from the positive electrode shuttle through the electrolyte, which is only permeable for ions, and enter the negative terminal. At the same time, electrons are released and, because of the electron-blocking electrolyte, they have to migrate through an external circuit connecting the two electrodes. The purpose of the separator is to prevent a short circuit of the electrodes. When fully charged, the cell is at high potential due to the difference in Li chemical potentials of the anode and cathode. This gradient serves as a driving force for the discharge, where the stored chemical energy is converted into electrical energy. [12] In this process, reduction of the positive electrode by capturing of electrons takes place, while oxidation proceeds at the negative terminal and vice versa for the charge process. The chemical reactions for charge (left to right) and discharge can be expressed by the following equations, with help of the system graphite C// LiFePO_4 .



LIBs are predominant in the field of portable electronic devices and are penetrating the market of electric vehicles and grid-energy storage. Their supremacy compared to other secondary batteries is mainly due to their high energy densities, higher working voltage and long service life. [9, 12, 13] However, in order to adopt LIBs for further markets and applications, several other parameters need to be matter of intense research. In addition to high energy densities, specific capacity, charge-discharge rates, cost, cycle life, safety and environmental impact need to be considered. Whereas high energy density is crucial for portable electronics, for example, more value is placed on factors such as cost, safety or cycle life for grid-energy storage. It stands to reason that improvements in performance can be achieved through innovations in the materials used in the cell, but since different applications require different properties, cell engineering is just as important. [14]

Table 1.1 gives a brief overview of various anode and cathode materials and their electrochemical properties, where the practical capacity is that, which is commercially available.

Table 1.1: Characteristics of conventional anode and cathode materials.[9, 15-17]

Electrode	Potential vs. Li/Li⁺ [V]	Theoretical Specific Capacity [mAh g⁻¹]	Practical Specific Capacity [mAh g⁻¹]
Anode			
Li metal	0	3860	-
Graphite	0.1	372	360
Li ₄ Ti ₅ O ₁₂	1.55	175	160
Cathode			
LiFePO ₄	3.45	170	160
LiCoO ₂	3.9	274	~150
LiMn ₂ O ₄	4.1	148	~130
LiNi _x Mn _y Co _z O ₂ *	3.8	280	160-190

* $x + y + z = 1$

As already stated above, certain criteria must be met for anode and cathode in order to maximise the performance of the LIB. Anodes and cathodes must provide a low and high redox potential compared to Li/Li⁺, respectively, as this leads to a high cell voltage. To achieve high gravimetric capacity, active anode materials should be as light and accommodate as much Li as possible, whereas sufficient electronic and ionic conductivities are prerequisite for optimising the cell performance. Not only for safety but also for environmental reasons, stability (chemical, thermal, mechanical) must be ensured at all times. This includes reversibility in terms of reaction with lithium ions over many cycles, increasing charge/discharge efficiency. Overall structural integrity is an important point, otherwise intercalation of Li-ions could be hindered. Looking for example at Li metal and Graphite as representatives, it is obvious that Li metal has the lower reduction potential with respect to Li/Li⁺ and lithium metal batteries (LMB) provide higher theoretical energy densities than competitors. But due to safety (stability of electrolyte) and structural (growth of dendrites during cycling) issues, graphite for most applications is preferable to Li metal as an anode.

Not only from a cost point of view the criteria for anode and cathode active materials are comparable, but also regarding conductivity and dense packing, allowing high power and high capacity per weight/volume, respectively. Stability is also of crucial importance with cathodes, so as unwanted side reactions with the electrolyte can cause major safety problems. Moreover, degradation of the material leads to a loss in efficiency. In order to provide good cycle life for the cell, it should display reversible behaviour over the entire range of the insertion/extraction process, implying minimal changes in volume of the hosts crystal lattice (e.g. 6% in LiFePO₄/FePO₄).

Having determined the requirements for appropriate electrode materials, also the electrolyte needs to be examined more closely. The primary task is the transport of lithium ions from one electrode to the other during charge/discharge. For this purpose, mainly liquid electrolytes consisting of a salt and an organic solvent are used. Proton-containing solvents, e.g. water or ethanol, are not suitable for common LIBs. Because the range within those solvents undergo electrochemical reactions is 2-4 V vs. Li/Li^+ , it lies in the operating range of commercial lithium batteries (0-4.5 V). Further developments in the field of electrolytes include ionic liquids, gel polymers and solid polymer, but herein we will focus on liquid electrolytes.

Alongside a high ionic conductivity of at least 10^{-3} S/cm and a negligible electronic conductivity, stability is a constant theme when designing a battery. As mentioned above, chemical and electrochemical resistance towards the electrodes and other components is just as important as high thermal stability. Ambient temperatures of -20 to 60 °C have to be withstood for reliable use. On top of that, high ignition or flash points are favoured, since during short circuits the temperature can rise to a critical level. Commonly used electrolytes are comprised of lithium salts, for instance LiPF_6 , LiBF_4 or LiClO_4 and organic solvents, such as ethylene carbonate, dimethyl carbonate and diethyl carbonate. [9, 12, 18, 19]

In view of the current situation, it must be emphasized once again that, above all, environmental and safety aspects are a decisive criterion for the materials used in lithium-ion batteries. Low cost, environmentally benign, and high operational safety are inevitable properties for materials of the future. Being a relevant member of this group, LiFePO_4 , a promising but also well-established cathode material, serves as a pivotal research topic of this thesis.

1.2 Olivine-type LiFePO_4

In 1997 Padhi et al. were the first to describe LiFePO_4 (LFP) as a potential cathode material for LIBs. [20] Iron (Fe) as an abundant metal has the advantage over cobalt (Co) that it is cheaper and more environmentally benign. Although the composite material offers further benefits, such as high cycling stability, thermal stability, non-toxicity and good compatibility with various electrolyte systems, considerable disadvantages with respect to commercial application cannot be neglected. The operating voltage of 3.45 V vs. Li/Li^+ is smaller, compared to common transition metal oxide batteries (cf. Table 1.1), however the main drawback are the transport properties, i.e. low electronic and ionic conductivity.

Nevertheless, with approaches like size reduction and carbon coating, substantial effort was made to enhance the poor intrinsic conductivity, in order to establish LFP cells as standard for different applications. These include, among other things, grid-scale as well as home energy storage and battery packs for electric vehicles (e.g. Tesla Model 3). [21-23]

The particular transport properties of LFP can be illustrated by taking a look at the crystal structure (Fig 1.2). The material belongs to the olivine family (M_2XO_4) and crystallizes in the orthorhombic cell in the space group Pnma. As depicted in figure 1.2 corner-shared FeO_6 -octahedra are alternately linked together in the bc-plane, while LiO_6 -octahedra form chains by sharing edges. Neighbouring layers of FeO_6 are bridged together via PO_4 tetrahedra. The structure suggests that ionic as well as electronic transport only takes place along one axis, namely the b-axis, resulting in poor transport properties. However, experimental studies from Amin et al. [24] suggest, that this anisotropy does not apply for large single crystals. Here, similar values were observed along the b- and c-axis for electronic (10^{-5} S/cm at 150 °C) and ionic (10^{-9} S/cm at 150 °C) conductivity, respectively, proposing a 2D transport mechanism. This theory is supported by studies conducted through Malik et al. Fe_{Li} - Li_{Fe} antisite defects are assumed to be those, with the lowest formation energy. Therefore, by blocking a 1D transport channel for Li^+ , the defect would cause the ion to circumvent the site, resulting in a 2D or even 3D transport mechanism. [25, 26]

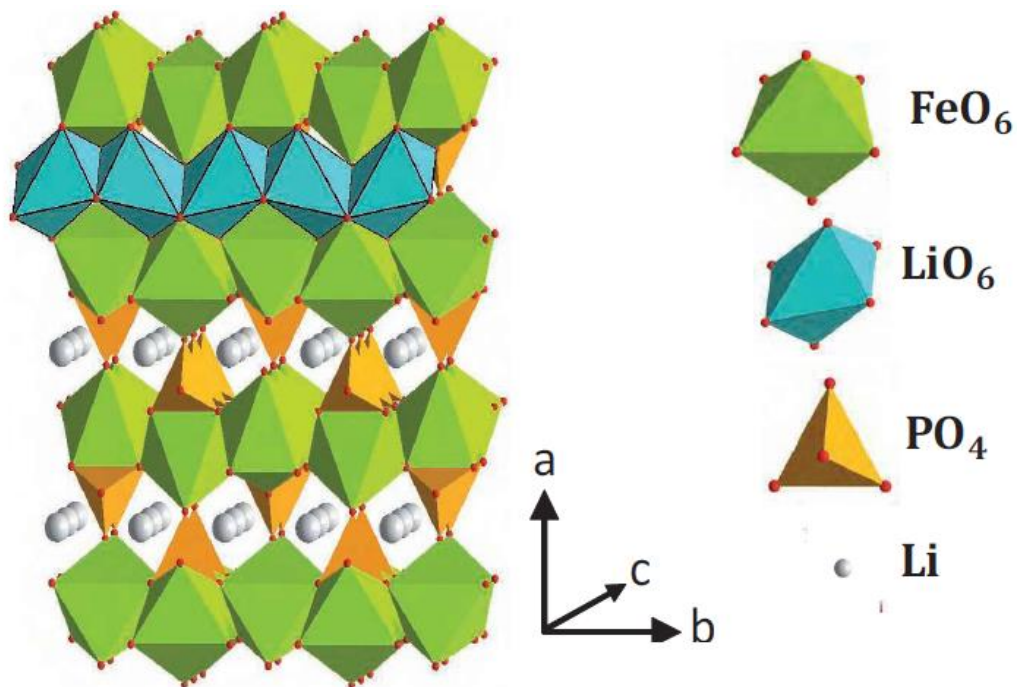


Figure 1.2: Crystal structure of LiFePO₄. [27]

Arrhenius plots (Fig. 1.3) calculated from nominally pure LiFePO_4 single-crystals illustrate the anisotropy as well as underlining the discrepancy between electronic and ionic conductivity, which is up to four orders of magnitude. Activation energies were found to be similar for each direction regarding electronic transport (0.6 eV), whereas those energies for ionic conduction show the expected behaviour (0.62 eV b-c axis, 0.74 eV a axis). [28]

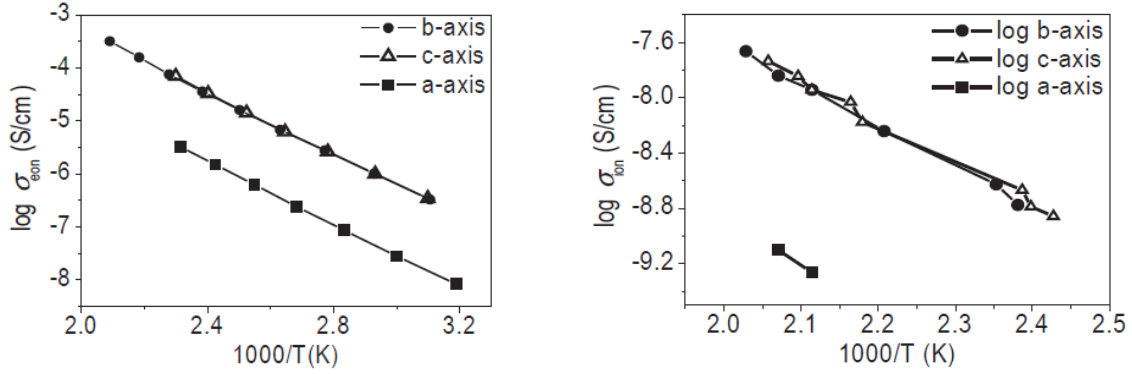


Figure 1.3: Arrhenius plot for electronic (left) and ionic (right) conductivity for nominally pure LiFePO_4 [27]

Despite the demanding transport properties, the chemical structure of LFP offers a multitude of characteristics that make it stand out for use as a positive active material. It is well-known that LFP shows a two-phase coexistence of LiFePO_4 and FePO_4 upon cycling, accompanied by a flat voltage plateau over a wide range of the (de)lithiation process. Since both compounds exhibit the same crystal structure, with the decrease in unit cell volume of FePO_4 compared to LiFePO_4 is only 6%, the process is highly reversible. [9, 27] The charge/discharge behaviour can be derived from the Gibbs free energy. As the chemical potential for a two-phase equilibrium remains constant, the corresponding voltage curve features a flat profile during the two-phase transition. [29] Before we take a closer look at the phase-transition models, the phase diagram should be examined more closely (Fig. 1.4.). One defining characteristic of Li_xFePO_4 ($0 < x < 1$) is its large miscibility gap at room temperature, over nearly the entire lithium composition range x , with $\sim 0.11 < x < \sim 0.95$. [30] This gap is reported to vanish upon heating and the system of $\text{LiFePO}_4/\text{FePO}_4$ coexistence gradually transforms into a solid solution of Li_xFePO_4 , which decomposes above ~ 500 °C into non-olivine phases as demonstrated by Delacourt et al. When cooling this solid solution below 140 °C, it separates into a mixture of four olivine-type phases. [31] This complex mixture converts into LiFePO_4 and FePO_4 sluggishly at room temperature. [32] It is worth mentioning that particle size can significantly change the phase diagram, especially the miscibility gap, of LFP, with nanoscale particles expected to reduce this gap, due to the big specific surface.

For the process of two-phase lithium intercalation, there are now several models describing the $\text{LiFePO}_4/\text{FePO}_4$ transition, but despite the numerous studies, there is no consensus on the exact mechanism. [33] Among the proposed models is the ‘domino cascade’ [34] where the particles are considered either fully lithiated or delithiated and the interfacial zone moves rapidly inside the crystallite like a wave in the a-direction on intercalation/deintercalation. Furthermore, there is the ‘core-shell’ or ‘shrinking-core model’ [35] where the insertion mechanism is not only determined by the strong anisotropy of the Li^+ diffusion, but also by the length of the diffusion path. The extraction starts at the surface of the particles and the $\text{LiFePO}_4/\text{FePO}_4$ interface migrates towards the centre. In this scenario, a core of unconverted LiFePO_4 remains, resulting in a loss of capacity. Li et al. proposed a hybrid phase-transition model, as a combination of the above mentioned models. [36] Herein, the LFP particle starts with the domino cascade approach, and soon becomes core-shell controlled as the charge process continues.

As already mentioned, there is no unanimous opinion on which model has unrestricted validity. However, it is becoming apparent that particle size plays a major role. For example, the phase transition of nanoparticles can best be described with the cascade model, since it is mainly the strong anisotropy that comes into play here. For larger particles, on the other hand, where additional factors such as Li-ion diffusion in the particle must be taken into account, the transition mechanism is found to be best explained with the core-shell or hybrid model. [37]

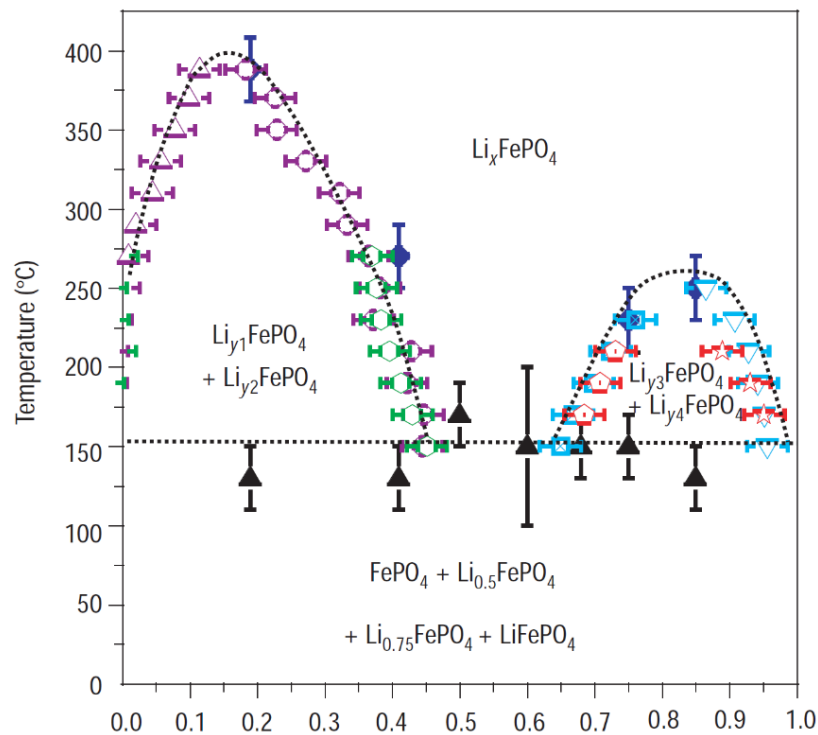


Figure 1.4: Phase distribution diagrams of LiFePO_4 . [31]

1.3 Motivation and Aim

As already discussed in the previous sections, lithium ion batteries with LiFePO_4 as cathode material have already established themselves as standard for a wide number of applications. Nevertheless, detailed knowledge of the underlying mechanisms is still lacking in some fields of research. Therefore, the motivation of this work was to bring more light into one of these not yet fully understood areas. The aim of this thesis was to extract charge-state dependent material parameters from electrochemical impedance spectra of thin-films in order to obtain a more profound understanding of the transport kinetics of electrons and Li-ions in LFP. To analyse the impedance data, there are approaches from different fields of research. Looking at the investigation of transport kinetics from the perspective of classical Li-ion research, one works under the assumption that the predominant driving force in the material is a gradient of lithium concentration. Since the conductivity of electrons is typically much higher than that of ions, electronic contributions are not considered in this scenario. The standard model to address this case is the so-called Randles Circuit. In the field of solid-state ionics, however, the approach is based on mixed ionic-electronic conductors (MIEC), so that the driving force is determined by both a gradient in composition and an electric potential difference. This is referred to as ambipolar diffusion. With the transmission line model, which is utilised in this case, both electronic and ionic contributions are now taken into account. Therefore, the objective was to create a system where the classical model of the Randles Circuit is no longer sufficient and the transmission line model has to be applied. Due to its poor electronic properties, which cannot be disregarded, LFP is therefore a very good candidate for this purpose.

Since the crystallographic orientation is of utmost importance here, LFP thin films were prepared by RF magnetron sputtering, as single crystals of the required size are not accessible and porous electrodes would generate a system too complex to interpret the impedance data using fit methods. The preparation of the films was subjected to an optimisation process, whereby particular attention was given to the choice of substrate. The thin films produced were continuously investigated structurally and electrochemically.

2 Theoretical Background

2.1 Electrochemical Impedance Spectroscopy [38-40]

Electrochemical impedance spectroscopy (EIS) is an enormously powerful and valuable tool for studying the characteristics of an electrochemical system in a non-destructive manner. Experimentally, a small amplitude AC voltage is applied to a system in equilibrium and the corresponding current response is then recorded. This is done over a wide frequency range, in order to enable the separation of different physical processes through their different time constants. The ratio between the current response and the voltage perturbation is the impedance, i.e. the frequency-dependent AC resistance of an electrical system. Although EIS is a comparatively simple method in terms of measurement, the interpretation of the recorded spectra and consequently of the processes in the system is not trivial.

A common approach to gain qualitative and quantitative information is to fit the impedance data with an equivalent circuit. Therefore, every such system can be characterised by a combination of resistive, capacitive and inductive elements. With the exact knowledge of the processes present, a suitable equivalent circuit can be modelled so that the electrode properties are reflected by the fitting parameters. But even without the precise knowledge of the system, the spectra can be parameterised in order to subsequently enable an electrochemical interpretation of the underlying reaction model.

The applied AC voltage $U(t)$, expressed as a sinusoidal function of time, can be described as

$$U(t) = U_0 \sin(\omega t) \quad (2.1)$$

with U_0 being the amplitude and ω the angular frequency (2.2), with f the frequency of the AC voltage.

$$\omega = 2\pi f \quad (2.2)$$

The response signal $I(t)$ of a linear system, with small amplitude excitation (U_0), has the form

$$I(t) = I_0 \sin(\omega t + \phi) \quad (2.3)$$

where the sinusoidal current exhibits the same frequency, but is shifted in phase (ϕ). Derived from Ohm's law (2.4) the impedance (Z) of a system can be illustrated by equation 2.5.

$$R = \frac{U}{I} \quad (2.4)$$

$$Z = \frac{U(t)}{I(t)} = \frac{U_0 \sin(\omega t)}{I_0 \sin(\omega t + \phi)} \quad (2.5)$$

Expressed as a complex function, this results in

$$Z = \frac{U_0 e^{i\omega t}}{I_0 e^{i(\omega t - \phi)}} = Z_0 e^{i\phi} = Z_0 (\cos \phi + i \sin \phi) \quad (2.6)$$

Therefore, the impedance can at any time be described by a real and imaginary part. Expressed as the absolute value of the impedance $|Z|$ (2.7), Z' (real part) corresponds to the sum of the ohmic resistances, while Z'' (imaginary part) reflects those contributions which experience a phase shift. For visualisation, a Nyquist plot can be used, where each data point is the vector representation of an impedance value, consisting of real part (Z'), imaginary part (Z'') and the phase angle (ϕ)

$$|Z| = \sqrt{Z'^2 + Z''^2} \quad (2.7)$$

In order to simulate the characteristics of a system, i.e. to fit the impedance data obtained, an equivalent circuit is modelled from various circuit elements. The simplest of these is the resistance R (2.8), where the impedance is independent from the frequency and the current does not exhibit a phase shift. With a capacitor (2.9), on the other hand, the current obtained is 90° out of phase with respect to the voltage, while the resistance decreases with increasing frequency. C here denotes the capacitance. An inductor (2.10) behaves in exactly the opposite way to a capacitor. Here, too, the current experiences a phase shift of 90° , but with a different sign, as the resistance increases with the frequency. L is the inductance.

$$Z_R = R \quad (2.8)$$

$$Z_C = \frac{1}{i\omega C} \quad (2.9)$$

$$Z_L = i\omega L \quad (2.10)$$

However, electrochemical processes often deviate from the ideal behaviour, which is why additional elements are necessary to describe the response of the system.

$$Z_{CPE} = \frac{1}{Q(i\omega)^n} \quad (2.11)$$

Equation 2.11 illustrates the constant phase element (CPE), which can be understood as a non-ideal capacitor. Herein n is the constant phase, $(-90 * n)^\circ$. For $n = 1$, the element becomes a capacitor with $Q = C$, whereas $n = 0$ corresponds to an ideal resistor $Q = R^{-1}$. When parallel to a resistor, the actual capacitance of the CPE can be estimated according to 2.12.

$$C = (R^{1-n}Q)^{\frac{1}{n}} \quad (2.12)$$

A further circuit element that is used for modelling diffusion transport behaviour is the Warburg impedance Z_W . For semi-infinite diffusion conditions, under the assumption of infinite diffusion layer thickness, Z_W has the form

$$Z_W = A\omega^{-\frac{1}{2}} - iA\omega^{-\frac{1}{2}} \quad (2.13)$$

where A is the Warburg coefficient. If diffusion however is spatially limited, either naturally or by design, then one refers to it as finite diffusion. Two types can be distinguished. The finite space (“open”) Warburg and the finite length (“short”) Warburg element. The general form of “open” (2.14) and “short” (2.15) Warburg, respectively, is illustrated below.

$$Z_{open} = Z_0(i\omega\tau)^{-\frac{1}{2}} \coth(i\omega\tau)^{-\frac{1}{2}} \quad (2.14)$$

$$Z_{short} = Z_0(i\omega\tau)^{-\frac{1}{2}} \tanh(i\omega\tau)^{-\frac{1}{2}} \quad (2.15)$$

The two variables Z_0 and τ depend on the system under consideration. The response of the open Warburg, depicted in a Nyquist plot, is reflected at high frequency in a straight line with a slope of 45° , which implies that the kinetics of the system are almost entirely limited by the diffusion process. At low frequencies, however, there is an increase in phase angle due to the onset of finite length effects, such as blocking boundaries, resulting in capacitor-like behaviour. This type of Warburg impedance is particularly relevant for the study of diffusion kinetics in electrode materials for LIBs. In the case of the short Warburg, in contrast, the impedance approaches the value Z_0 at low frequencies resulting in a half tear-drop shape of the spectrum. This phenomenon is observed, for instance, when diffusion takes place through a layer of finite length.

2.1.1 Randles Circuit

Now consider a simple system of an electrode immersed in an electrolyte. The AC response of this system, where charge transfer as well as diffusion of the electroactive species occurs, can be modelled by the equivalent circuit depicted in figure 2.1, the Randles Circuit. This illustration is valid for the diffusion of a metal into an oxide electrode, but only under the assumption that the driving force in the system is a gradient in composition and electronic contributions are neglected.

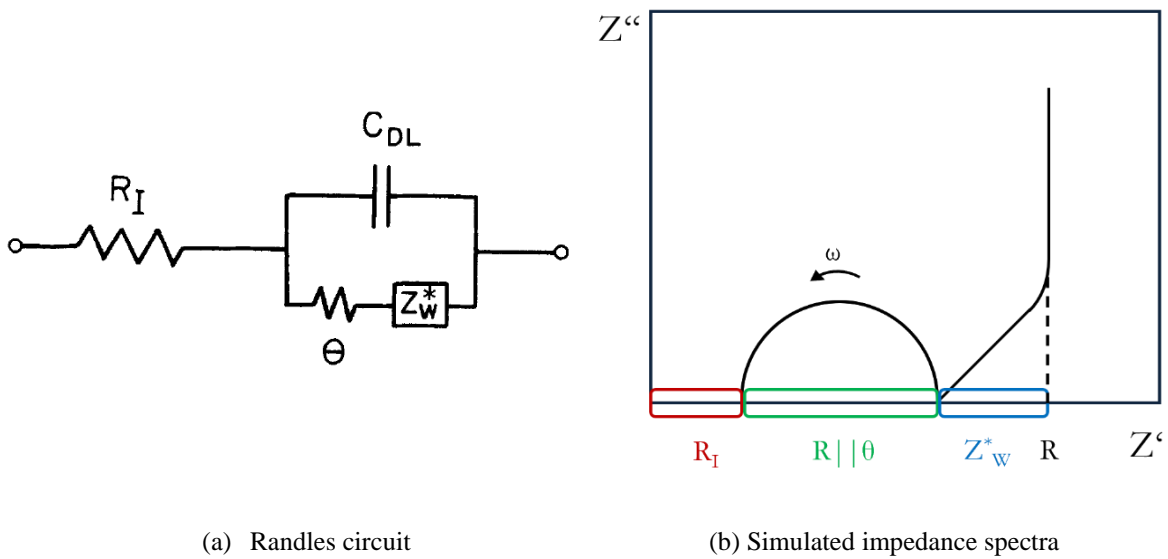


Figure 2.1: Illustration of the Randles circuit (a) [39] and simulated impedance spectra of the model (b).

R_I is the series combination of ionic resistance of electrode and electrolyte, C_{DL} denotes the double-layer capacitance of the electrode-electrolyte interface, θ is the charge transfer resistance and Z_w^* is the above discussed Warburg impedance for finite space diffusion conditions. Figure 2.1 shows a general form of the AC response illustrated in a Nyquist diagram. At high frequencies, an offset can be observed which is due to the ohmic resistance R_I . This value represents the high frequency intercept of the semicircle, derived from the parallel combination of C_{DL} and θ . The 45° straight line is described by the Warburg element, whereby at very low frequencies a transition to a perpendicular line can be observed, resulting in a limiting resistance R . In general, with a suitable, i.e. high diffusion coefficient, as is the case in this example, a good distinction can be made between the individual limiting processes in the investigated system. At low frequencies, charge transport is predominant, represented by the semicircle, while at medium frequencies the process is diffusion controlled, towards the limiting resistance, due to finite space effects at very low frequencies.

2.1.2 Transmission Line

As stated above, this equivalent circuit is only valid under the assumption that diffusion is driven solely by a gradient in composition and not by an electric field. That is, electron transport does not contribute to the total resistance, with $R_{\text{eon}} \rightarrow 0$. However, these assumptions do not apply to the transport properties of LFP, which is why a more general model has to be used to describe the diffusion processes. With the approach of the transmission line, it is taken into account that the diffusing electroactive species is not only exposed to a chemical potential gradient but also to an electric field. Thus, mixed conducting behaviour can be studied.

The generalised expression of the transmission line of the two systems relevant for this thesis electrode|MIEC|electrode and electrode|MIEC|electrolyte, respectively, is represented in figure 2.2 (derived from Lai et al. [40]). Here, Z_A , Z_C and Z_B , Z_D are the terminal impedances corresponding to the impedance of the electrode|MIEC (electrolyte|MIEC) interface for ion and electron transfer, respectively. R_{ion} and R_{eon} are the resistances in the ionic and electronic rail, respectively, whereas C_{chem} represents the chemical capacitance, a feature directly related to ambipolar diffusion. Hence, it illustrates the connection between ionic and electronic diffusion given by the local electroneutrality condition.

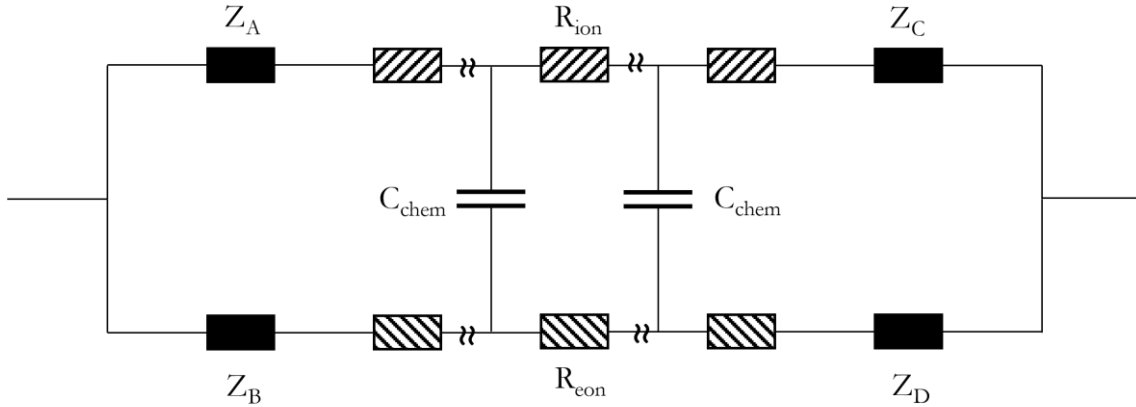


Figure 2.2: Generalised equivalent circuit for a mixed ionic and electronic conductor.

By applying the appropriate boundary conditions for the terminal Z_{A-C} , the equivalent circuit can now be adapted to the two systems of interest. For a detailed topology of the transmission line for both cases, see section 3.4.

2.2 Radio-Frequency Magnetron Sputtering

In order to be able to subsequently investigate diffusion kinetics in LFP, it was of utmost importance to produce thin-film electrodes with a defined composition and known crystallographic orientation. Therefore, special attention was paid to the fabrication of the thin films and the optimisation of these. According to the literature [41-44], radio-frequency (rf) magnetron sputtering is a suitable method for manufacturing the sample electrodes in the desired quality.

This deposition technique, which belongs to the group of PVD (physical vapour deposition) processes, is known for its ability to produce smooth surfaces with excellent mechanical properties and is of particular importance when roughness, grain size, stoichiometry and other quality requirements are given more importance than the deposition rate. In a PVD process in general, the material to be deposited, the target, is converted into atomic particles by the thermal physical process of collision. These particles are then directed under low pressure onto the substrate, where they form a physical coating. [45]

The working principle of rf magnetron sputtering is described as follows. The energetic ions (typically Ar^+) for the bombardment of the target, are generated in a glow discharge plasma. During this sputtering process, not only target ions are emitted, but also secondary electrons, which play an important role in maintaining the plasma. By using magnetrons, these secondary electrons can be trapped on a circular trajectory close to the target, which significantly increases the probability of an electron-atom collision and thus results in a higher ionisation efficiency. The enhanced plasma density in the vicinity of the target also leads to increased sputter rates and consequently also deposition rates. The magnetic field of the magnetron, which extends parallel to the target surface, results from the arrangement of the magnets. One pole is positioned in the centre of the target, while a second pole, consisting of a ring of magnets, is placed along the outer edge. This causes the typical erosion patterns on the target surface. (Fig. 2.3) [46]

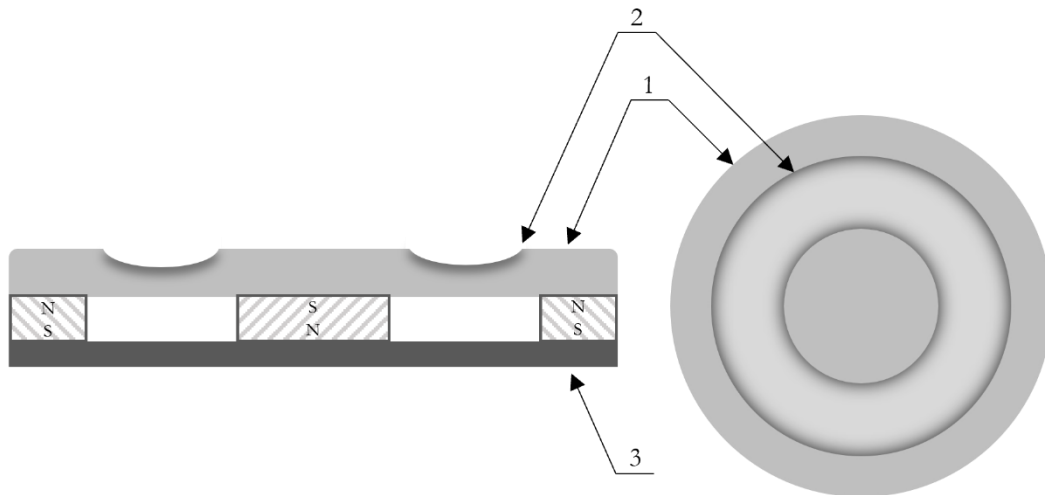


Figure 2.3: Schematic illustration of magnetron sputter target. 1 – target, 2 – magnetic circuit, 3 – erosion zone.

A further difference respectively advantage to other sputtering processes is the use of radio frequency, which occurs at the frequency internationally used for rf power supply equipment, that is 13.56 MHz. Due to the high-frequency alternating field, ions and electrons are accelerated alternately in both directions, whereby ions can no longer follow the oscillation from a certain frequency due to their inertia. This leads to an increased number of collisions of the electrons with the argon atoms, which in turn enhances the plasma density. As a result, it is possible to operate at lower pressure with equal sputtering rates compared to DC sputtering. [45] Nevertheless, rf magnetron sputtering also entails several requirements. In addition to the basic demand for a high vacuum to ensure the mean free path of the particles, the high power and use of radio frequency means that sufficient cooling of the target and adequate electrical shielding must be ensured.

The deposition of the particles on the substrate normally takes place at room temperature and in order to enable optimal layer growth, the samples are heated afterwards, i.e. post-annealed. A special feature of the sputtering system used in this work is that the substrate in the vacuum chamber can be brought to a desired temperature by an integrated heater. This initiates direct crystallisation during the deposition process, which not only saves time by eliminating a work step, but also optimally increases quality of the produced thin-films.

2.3 Contact Resistance of Pt/Nb:STO

Due to the experimental setup of the electrochemical investigation methods, it is necessary that the electrode, or more precisely the substrate on which it is deposited, is electrically contactable. An electrically conductive substrate that showed very good results in terms of the quality of the electrode layer was niobium doped SrTiO₃ (Nb:STO) single crystal, whereas a platinum (Pt) wire was used to contact this substrate. For details please refer to the Experimental section. However, this interface exhibited a very high resistance, which in this configuration overlapped the actual features that were to be measured.

As a result of this metal-perovskite junction Pt/Nb:STO, a Schottky barrier with rectifying character is formed during contact, which has the effect that the electron flow from the semiconductor to the metal is easier than the conduction in the opposite direction. Mechanistically, when the two materials are brought together, the Fermi levels are aligned (in thermal equilibrium), resulting in a band bending at the interface. This bending in turn results in a potential barrier, the Schottky barrier. (Fig. 2.4) [47]

The barrier height for Pt/Nb:STO junction is reported to be ~ 1 eV, which might be a potential reason why well-controlled electrochemical studies are not achievable. [48-50] Therefore, it is necessary to modify this contact, either by using a buffer layer such as SrRuO₃ (SRO) or LaNi_{1-x}Co_xO₃ (LNCO), which aims to improve the interface resistance, or by using other materials as substrate or electrode. [51]

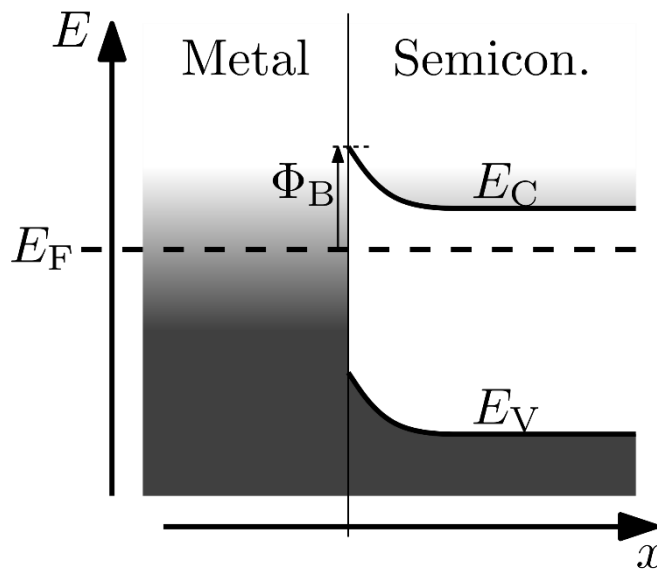


Figure 2.4: Schematic illustration of a Schottky contact of a metal and a n-type semiconductor. Φ_B – barrier height, E_F – Fermi-niveau, E_C – lower level of the conduction band, E_V – upper level of the valence band. [52]

3 Experimental Methods

3.1 Introduction

The experimental part of this work can essentially be divided into two sections, whereby in the first step, the focus of the experiment was on the fabrication of LFP thin films by RF magnetron sputtering and the optimisation of the deposition process. Depending on the requirements, different substrates were used as a basis, with non-conductive materials such as sapphire (Al_2O_3) and STO being used for preliminary tests and the determination of optimal deposition parameters, respectively. The knowledge gained was then applied to the production of defined layers on electrically conductive substrates, which include Nb:STO, glassy carbon and various conductive coatings (Pt, SRO, LNCO). The manufacturing and optimisation process has been subjected to continuous quality control by characterising the deposited layers using methods such as x-ray diffraction (XRD), scanning electron microscopy (SEM), transmission electron microscopy (TEM) optical light microscopy and profilometry. Further on, suitable thin-film electrodes, which were expected to have electrical contactability due to the substrate selected, were used for electrochemical investigations. The aim was to carry out these investigations at different states of charge of the electrodes, i.e. at varying lithium content. For this reason, along with the characterisation (EIS, CV), efforts were made to perform charging cycles in aqueous electrolyte.

3.2 Preparation of LiFePO_4 Thin-Films

The preparation of the LiFePO_4 thin-films was carried out by means of RF magnetron sputtering. The device on which this work was conducted was developed in-house by AG Fleig and was subject to constant further development during the course of this work. These additional refinements focused in particular on the type and geometry of the heating element. As the heating unit also served as a sample stage, the shape, position and design of this device were crucial for successful deposition. Throughout the project, it became apparent that not only the deposition temperature has a significant impact on the layer quality, but also that a homogeneous temperature distribution in the substrate is of considerable importance. Initially, a heating element consisting of a platinum wire laid in serpentine with a corundum plate as a cover was used, hereinafter referred to as heater-type A (Fig 3.1 a) This configuration showed a uniform heating of the corundum stage and transmitted this behaviour onto the substrate.

Due to application-specific problems, among others concerning the heating power, this element was replaced by a new unit consisting of a spiral of wound platinum wire with a fused silica disc as sample support (~ 0.2 cm) (hereinafter type B), (Fig 3.1 b) whereby this disc was coated with $(\text{La}_{0.6}\text{Sr}_{0.4}\text{FeO}_3)$ LSF on the rear side as an update to ensure better heat transfer to the substrate (hereinafter type C). In the beginning, this setup showed sub-optimal behaviour, especially with regard to the temperature distribution in the sample support and therefore in the substrate, but this has been improved by further refinement with an additional LSF layer.

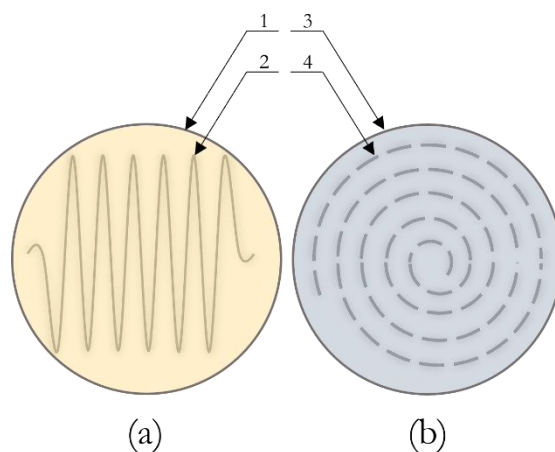


Figure 3.1: Schematic illustration of the different heating units. (a) Corundum sample stage, on top of meandering platinum wire (heater-type A). (b) Fused silica disc, with wound platinum spiral (heater-type B/C).

1 – corundum sample holder, 2 – platinum wire, 3 – fused silica disc, 4 – platinum spiral

In order to be able to determine the current temperature of the heater, a thermocouple type S was located in the middle of the element, close to the sample (sample stage). The values could be obtained via an Omega Pt control panel, which could be accessed via dedicated software (ElchiTools) on the computer. The temperature of the heater was controlled by adjusting the power, either via the software or manually by regulating the voltage or current. In order to determine the actual temperature of the substrate with respect to the thermocouple temperature, a calibration was carried out for each heater type for the respective material. For this, the surface temperature of the reference substrate YSZ (emissivity coefficient $\varepsilon = 0.9$) was measured with a pyrometer and related to the temperature read from the thermocouple. Apart from the temperature, the heating and cooling rates, the deposition time, the sputter pressure, the argon gas flow and the sputter-power were also subject to optimisation. Deposition parameters were taken from the literature [41-44] and adapted to the given setup. In the following sections, you will find a detailed summary of the relevant substrates, as well as an overview of the parameters used for the deposition of the thin-films.

The deposition process, however, was more or less identical for each sample and can be described as follows. As target material LiFePO_4 (2"×0.125", Advanced Engineering Materials, China) was used, with a distance from the substrate to the target of 6 cm. Since erosion zones were formed during the sputtering process (see Fig. 2.3), from a certain point onwards the target was smoothed with a fine sandpaper before each deposition to ensure reproducibility. Prior to the initial deposition, each substrate was thoroughly cleaned to remove contaminations from the surface. For the first few samples, this was done by wiping the surface with an ethanol-soaked cleanroom tissue. To ensure a more thorough cleaning, however, it was quickly switched to treating the substrates for 10 min in ethanol in an ultrasonic bath and then blow drying them with nitrogen. Next, the vacuum chamber with the inserted substrate was evacuated to a pressure of $\sim 10^{-5}$ mbar and then the sample was heated to the desired temperature at a defined rate. This rate was initially regulated automatically by a programme (ElchiTools). After modification of the system, this was done manually by changing the applied voltage or current. A mass flow controller (MFC) was used to adjust the argon gas flow, as a argon atmosphere was required to avoid the formation of foreign phases at high temperatures through oxidation. The unit in which the argon flow is specified is standard cubic centimetres per minute (sccm). The sputter pressure was adjusted by opening or closing the gate valve (valve between vacuum chamber and turbopump). After a certain pre-sputter time (10-20 min) at a given power, in order to clean the surface of the target, the deposition started, whereby the duration here resulted from the desired layer thickness. For this purpose, the approximate deposition rate was calculated by determining the layer thickness of certain samples via a SEM cross-section, from which the deposition rate could then be derived. Once the process was completed, the sample was cooled down at a defined rate to roughly room temperature and subjected to structural characterisation.

3.2.1 Sapphire

In order to establish the basic parameters for the deposition of LFP in preliminary tests and to study the influence of the temperature in more detail, sapphire (0001) single crystals ($10 \times 10 \times 0.5$ mm³, Crystec Germany) were used as substrates. These offer the advantage that they are recyclable and therefore more cost-effective than other single crystals. In table 3.1 the general deposition parameters are listed. Depositions at substrate temperatures between 450 and 650 °C were carried out, with steps of 50 °C.

Table 3.1: Parameters for deposition of LFP on Al₂O₃ single crystals.

Al₂O₃	
Temperature [°C]	450 – 650
Sputter pressure [mbar]	2.5×10 ⁻²
Sputter power [W]	60
Argon gas-flow [sccm]	15
Pre-sputter time [min]	10
Deposition time [s]	120
Heating / Cooling rate [°C/min]	60 / 30

3.2.2 STO

Various versions of STO single crystals (Crystek Germany) were used as substrates for the production of LFP thin films. Due to the transferability of the findings to Nb:STO as a conductive material or as a basis for conductive coatings, intensive research was carried out to optimise the deposition on this material. In order to achieve different crystallographic orientations of the fabricated layers (i.e. altered transport properties), single crystals with orientations (100) and (110) were selected. The substrates were of the size 10x10x0.5 and 5x5x0.5 mm³, respectively. Based on the parameters determined in the preliminary tests (Table 3.1), further optimisation was carried out. Due to the change of the heating element in the development of the sputtering device, this optimisation concentrated mainly on the deposition temperature. However, the deposition time, which has a significant influence on the layer thickness, was also varied, as well as the heating rate and the argon flow. While reducing the former allows for a better temperature equilibrium of the substrate, increasing the latter can counteract a possible oxygen leak in the setup. Table 3.2 provides an overview of the various parameters used, but for specific values, please consult section 4.1.2.

Table 3.2: Parameters for deposition of LFP on STO single crystals.

SrTiO₃	
Temperature [°C]	500 – 625
Sputter pressure [mbar]	2.5×10^{-2}
Sputter power [W]	60
Argon gas-flow [sccm]	15 / 45
Pre-sputter time [min]	15
Deposition time [s]	20 – 120
Heating / Cooling rate [°C/min]	60 (30) / 30

3.2.3 Nb:STO

Niobium doped STO (0.5 wt % Nb, Crystec Germany) single crystals (100) served as a conductive substrate, which were intended to enable electrical contactability of LFP. The deposition on the single crystals ($5 \times 5 \times 0.5 \text{ mm}^3$) was conducted with the following parameters, varying only the film thickness (i.e. deposition time). (Tab. 3.3)

Table 3.3: Parameters for deposition of LFP on Nb:STO single crystals.

Nb:SrTiO₃	
Temperature [°C]	550
Sputter pressure [mbar]	2.5×10^{-2}
Sputter power [W]	60
Argon gas-flow [sccm]	15
Pre-sputter time [min]	15
Deposition time [s]	20 / 60
Heating / Cooling rate [°C/min]	60 / 30

3.2.4 Conductive Coatings

The conductive coatings SrRuO₃ (SRO) and LaNi_{0.5}Co_{0.5}O₃ (LNCO) were utilised in two different contexts. Firstly, based on the findings of the electrochemical investigations carried out (4.3.1), they were intended to serve as a buffer layer between Pt and Nb:STO to reduce the contact resistance of this junction (see section 2.3) and secondly, they were to provide an electrically conductive substrate between STO and LFP. Later investigations using TEM (4.1.6) suggest that this coating could also be applied as a potential protection layer against interdiffusion between STO and LFP. However, this will not be discussed in detail in this thesis. The coatings were produced by PLD (pulsed laser deposition, for details see further below). In a preliminary test, it became apparent that SRO was not stable under the given sputtering process conditions (argon atmosphere, high temperatures), which is why the focus was placed on LNCO as the material of choice and SRO was only of secondary importance.

To act as a buffer layer between Pt and Nb:STO, LNCO was deposited on the backside of a single-side polished Nb:STO (100) single crystal. Subsequently, 200 nm Pt was sputtered onto the LNCO layer at room temperature (BAL-TEC Med 020 Coating System), covering the edges with a mask to prevent Pt from contacting the sides of the single crystal. Table 3.4 contains the parameters for the preparation of the platinum layer. Next, LFP was deposited on the polished front side of the Nb:STO substrate. The parameters can be taken from table 3.3, with a sputter time of 60 min and a heating rate of 30 °C/min.

To create a conductive layer between STO and LFP, LNCO was first deposited on the front side of a STO (110) resp. (100) single crystal (5×5×0.5 mm³) by PLD. Since STO is a non-conductive substrate, Pt paste (Tanaka 7% terpineol) had to be applied to one edge of the crystal to establish electrical contact between the front and back surfaces, as this was necessary for electrochemical characterisation. The paste was dried for ~1h at 120 °C and afterwards 200 nm Pt was sputtered onto the back side of the substrate (table 3.4). Further on, LFP was deposited on the LNCO layer, the parameters of which can be found in Table 3.5. The SRO layer was applied in the same manner (parameter table 3.6).

Table 3.4: Parameters for deposition of platinum (200 nm).

Platinum	
Argon pressure [mbar]	2×10^{-2}
Sputter current [mA]	100
Pre-sputter time [s]	30
Deposition time [s]	322
Layer thickness [nm]	200

Table 3.5: Parameters for deposition of LFP on STO (110)|LNCO and STO (100)|LNCO.

STO LNCO	(110)	(100)
Temperature [°C]	500 / 550 / 600	550
Sputter pressure [mbar]	2.5×10^{-2}	2.5×10^{-2}
Sputter power [W]	60	60
Argon gas-flow [sccm]	15	15
Pre-sputter time [min]	15	15
Deposition time [min]	77	38
Heating / Cooling rate [°C/min]	30 / 30	30 / 30

Table 3.6: Parameters for deposition of LFP on STO|SRO

STO SRO	
Temperature [°C]	550
Sputter pressure [mbar]	2.5×10^{-2}
Sputter power [W]	60
Argon gas-flow [sccm]	15
Pre-sputter time [min]	15
Deposition time [s]	39
Heating / Cooling rate [°C/min]	30 / 30

PLD

The LNCO and SRO layers were deposited on the STO (100) and (110) single crystals, respectively, using pulsed laser deposition (PLD) technique. The parameters are summarised in Table 3.7. For the deposition of the LNCO layers, a target with the composition $\text{LaNi}_{0.5}\text{Co}_{0.5}\text{O}_3$ was used, which was prepared via a standard Pechini synthesis method, while the SrRuO_3 was commercially acquired (pldtargets.com). The temperature calibration used was performed on a YSZ single crystal.

Table 3.7: Parameters for PLD deposition of SRO and LNCO.

	LNCO	SRO
Substrate-target distance [cm]	6	7.5
Heater power [%]	70	53
Temperature [°C]	700	600
pO ₂ [Pa]	4	13
Pre-ablation [pulses @ Hz]	250 @ 2	450 @ 10
Deposition [pulses @ Hz]	4000 @ 2	15000 @ 10
Cooldown [°C/min]	15	4
Laser fluence [J/cm ²]	1	1

3.2.5 Alternative Conductive Substrates

With SRO and LNCO as electrically conductive coatings, an alternative to Nb:STO as a support material was already discussed in the previous section. In the following, however, two further candidates will be introduced, both of which offered interesting properties. On the one hand a layer system of Pt|Ti|Al₂O₃|Pt and on the other hand glassy carbon.

Glassy carbon (10x10x1 mm, SIGRADUR®, HTW Germany) possesses very interesting properties, such as good electrical conductivity, high thermal-chemical and high-temperature resistance. The disadvantages for the application in the context of this project include the poor wetting by melts, as this impedes the adhesion of the LFP layer. Nevertheless, attempts were made to produce a thin film on this substrate under various conditions. A summary of the parameters can be found in Table 3.6. The second approach to be discussed is Pt|Ti|Al₂O₃|Pt. Here, the double layer Pt/Ti forms the back side while Pt on the front side provides the foundation for the deposition of LFP. Sapphire forms the support in the middle. At room temperature, 5 nm Ti (titanium) was sputtered onto the back of a sapphire (0001) single crystal (5×5×0.5 mm) (BAL-TEC Med 020 Coating System), whereby this layer acted as an adhesive base for the subsequent Pt layer (100 nm). On the front side, 200 nm were hot deposited (1000 °C) onto the Al₂O₃ single crystal to obtain a defined, smooth Pt surface. See table 3.7 for the deposition parameters of the metals. These crystals were then coated with Pt paste (Tanaka 7% terpineol) on one edge and dried for ~1h at 120 °C. The values in Table 3.8 depict the parameters for the deposition of LFP on the Pt layer.

Table 3.8: Parameters for deposition of LFP on glassy carbon.

Glassy carbon	
Temperature [°C]	550 / 600 / 650
Sputter pressure [mbar]	2.5×10^{-2}
Sputter power [W]	60
Argon gas-flow [sccm]	15
Pre-sputter time [min]	15
Deposition time [min]	120
Heating / Cooling rate [°C/min]	60 / 30

Table 3.9: Parameters for deposition of titan and platinum.

	Ti	Pt
Argon pressure [mbar]	7.3×10^{-2}	2×10^{-2}
Sputter current [mA]	100	100
Pre-sputter time [s]	300	30
Deposition time [s]	55	161 / 322
Layer thickness [nm]	5	100 / 200

Table 3.10: Parameters for deposition of LFP on platinum.

Platinum	
Temperature [°C]	500 / 550 / 600
Sputter pressure [mbar]	2.5×10^{-2}
Sputter power [W]	60
Argon gas-flow [sccm]	15
Pre-sputter time [min]	15
Deposition time [min]	60 / 120
Heating / Cooling rate [°C/min]	60 / 30

3.3 Structural Characterisation

The layer preparation was permanently accompanied by structural characterisation methods in order to monitor the quality and to be able to apply the knowledge gained to the optimisation of the process. These techniques were X-ray diffraction (XRD), scanning electron microscopy (SEM), transmission electron microscopy (TEM), profilometry and optical microscopy.

The XRD measurements were carried out at the X-Ray Centre (XRC) of the Vienna University of Technology. The interpretation of the diffraction patterns focused in particular on the texture, i.e. crystallographic orientation of the layers and the phase composition. Three different methods were applied for this purpose:

1. Diffractograms in Bragg-Brentano geometry were acquired from each layer as a standard. ($\text{Cu}_{K\alpha}$, PANalytical Xpert Pro, 10-90 °)
2. In order to eliminate dominant reflexes of the substrate in diffractograms of very thin layers, a number of samples were measured in grazing incidence (GID) mode. ($\text{Cu}_{K\alpha}$, Empyrean PANalytical)
3. To investigate in particular the behaviour of the SRO and LNCO layers under sputtering conditions, temperature-dependent non-ambient XRD measurements were carried out (argon atmosphere, T to 700 °C, $\text{Cu}_{K\alpha}$, Anton Paar XRK 900, PANalytical Xpert Pro)

SEM measurements were performed at the USTEM (Vienna University of Technology) using an FEI Quanta 250 FEGSEM, by J. Ring and A. Bumberger, where the morphology was determined by scattered secondary electrons (SE). Also TEM (USTEM FEGTEM F20) characterisations were carried out through A. Bumberger. The surface roughness was examined with a profilometer of the type DektakXT (Bruker) and the optical light microscope was of the company Zeiss.

3.4 Electrochemical Characterisation

Samples with adequate layer quality on a suitable substrate, i.e. electrically contactable, were subsequently used for electrochemical investigation. For this purpose, two different experimental setups were used, which are discussed in further detail below. The first was a "liquid cell" configuration (section 3.4.1), which was designed to simulate an electrochemical cell with an aqueous electrolyte, while the second was a microcontact setup in which the measurements were carried out in a controlled gas atmosphere (section 3.4.2). Considering these techniques in terms of the measurement direction, the first case is referred to as cross-plane geometry. This indicates that the material properties (e.g. transport of charge carriers) are investigated perpendicular to the sample surface. In theory, this geometry enables altering the charge state of the LFP electrode, as ions as well as electrons can be extracted from or incorporated into the material. For this purpose, however, electrically permeable substrates, very thin sample layers and low contact resistances at the interfaces are required, which makes practical implementation increasingly difficult. In-plane geometry, on the other hand, is referred to as when the direction of measurement is parallel to the surface of the specimen. This is the case for electrodes that are located on the sample surface. The advantage here is that no electrically conductive substrate is required and the experimental effort is comparatively low. However, since the microelectrodes used are pure electron conductors, i.e. perfectly blocking for ions, the lithium stoichiometry cannot be varied, which represents a significant drawback. A schematic representation of cross-plane and in-plane geometry is given in figure 3.2.

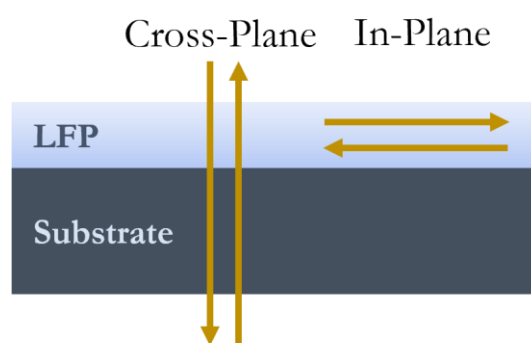


Figure 3.2: Schematic illustration of cross-plane and in-plane measurement geometry

3.4.1 Liquid Cell

Figure 3.3 shows a schematic layout of the cell. An Ag/AgCl (Ag wire in sat. KCl) electrode was used as a reference (RE). The potentials vs. Ag/AgCl were converted to those vs. Li/Li⁺, knowing that the potential of Ag/AgCl electrode is 3.24 V vs Li/Li⁺. A porous Li_xCoO₂-coating on an yttria-stabilised zirconia (YSZ) (100) single crystal (10×10×0.5 mm³) coated on both sides with Ti/Pt (5/100 nm) was used as counter electrode (CE), the capacity of each electrode being known. The working electrode (WE) was the respective sample to be investigated. Both CE and WE were contacted via the rear side with the help of a Pt wire and a glass fibre separator (VWR Germany), sandwiched between CE and WE prevented the two from being shorted. Aqueous electrolytes were LiCl and LiNO₃ (both 1M), respectively. All three electrodes were connected to the computer via a workstation (BioLogic, SP-200 potentiostat with EIS option) where a wide range of electrochemical investigations could be controlled via the EC-Lab® (BioLogic) software.

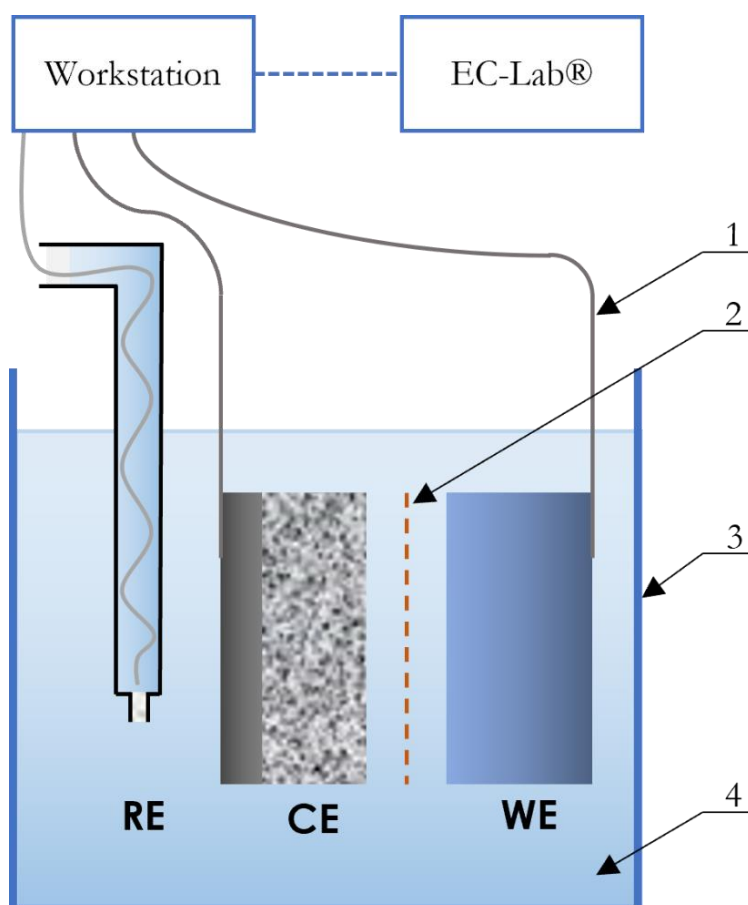


Figure 3.3: Schematic representation of the "liquid cell". RE – reference electrode, CE – counter electrode, WE – working electrode, 1 – platinum wire, 2 – separator, 3 – beaker, 4 – aqueous electrolyte

Cyclic Voltammetry

The cyclovoltammetric measurements were performed within the same setup as described in section 3.4.1. The obtained current response, which was generated by applying a linearly increasing (decreasing) potential to the working electrode, was plotted against the actual voltage (measured vs. RE). The voltage steps were 0.05 and 0.1 mV/s, respectively, with limits of 1.0 V and -0.2 V (vs. RE). Two complete scans were performed for each step size value.

Charge-Discharge Experiments

To perform the cycle experiments, i.e. altering the Li content of the thin film, a charge/discharge current was applied to the working electrode (positive/negative sign) and the measured voltage response was recorded over time. The magnitude of the current was estimated using the C-factor [h^{-1}]. This factor is derived from the capacity [mAh] of the LFP thin film electrodes, which can be obtained from the mass [g], calculated via the crystallographic density, assuming a perfectly dense film and the theoretical specific capacity of LiFePO_4 (170 mAh/g). The values of the specific currents were in the range of 20-500 nA. A cut-off limit of > 0.9 V and < 0.1 V for the charge and discharge step was set, corresponding to a potential of 4.14 V and 3.34 V vs. Li/Li^+ , respectively. This frame was defined because of the equilibrium potential of LFP (3.45 V vs. Li/Li^+), considering reasonable overpotentials. A rest step was programmed at the beginning of the cycle to record the initial open-circuit voltage.

Cross-plane Impedance Spectroscopy

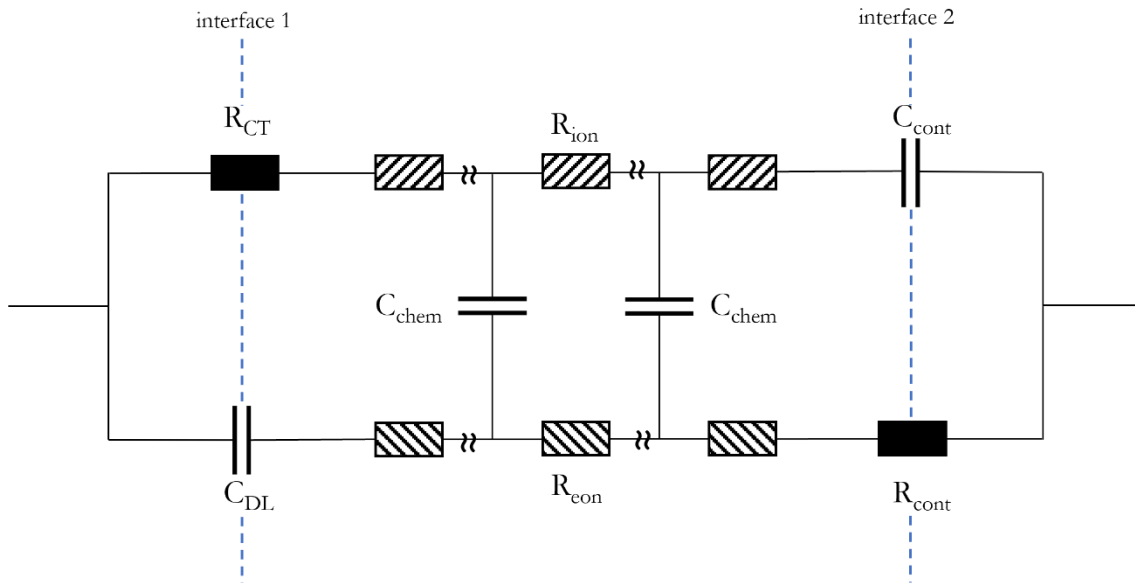


Figure 3.4: Transmission line equivalent circuit for electrolyte|MIEC|electrode, derived from figure 2.2.

Figure 3.4 illustrates the specified equivalent circuit model for the interpretation of the given system, which can be derived by applying the appropriate boundary conditions to terminals Z_{A-C} of figure 2.2. [40, 53, 54] Interface 1 and 2 represent the boundary areas of electrolyte|LFP and LFP|electrode (current collector), respectively. Following the assumption that the electrolyte behaves like a pure ion conductor, this results in an electron-blocking characteristic of the interface 1. Consequently, charge transfer at this boundary only takes place via Li-ions. These properties are represented by a charge-transfer resistance (R_{CT}) in the ionic and a double-layer capacitance (C_{DL}) in the electronic rail, respectively. The current collector, in contrast, is a pure electron conductor, which is why interface 2 has a blocking effect for ions. The electron transport across this interface is represented by the contact resistance (R_{cont}), while the behaviour of the ion rail is symbolised by a capacitor (C_{cont}). For the impedance measurements, the PEIS (potentiostatic EIS) tool of the EC-Lab software was used. An alternating voltage with an amplitude of 20 mV was applied and the impedance was measured in a frequency range of 1 MHz to 1 mHz, with 6 data points per decade.

3.4.2 Microcontact Setup

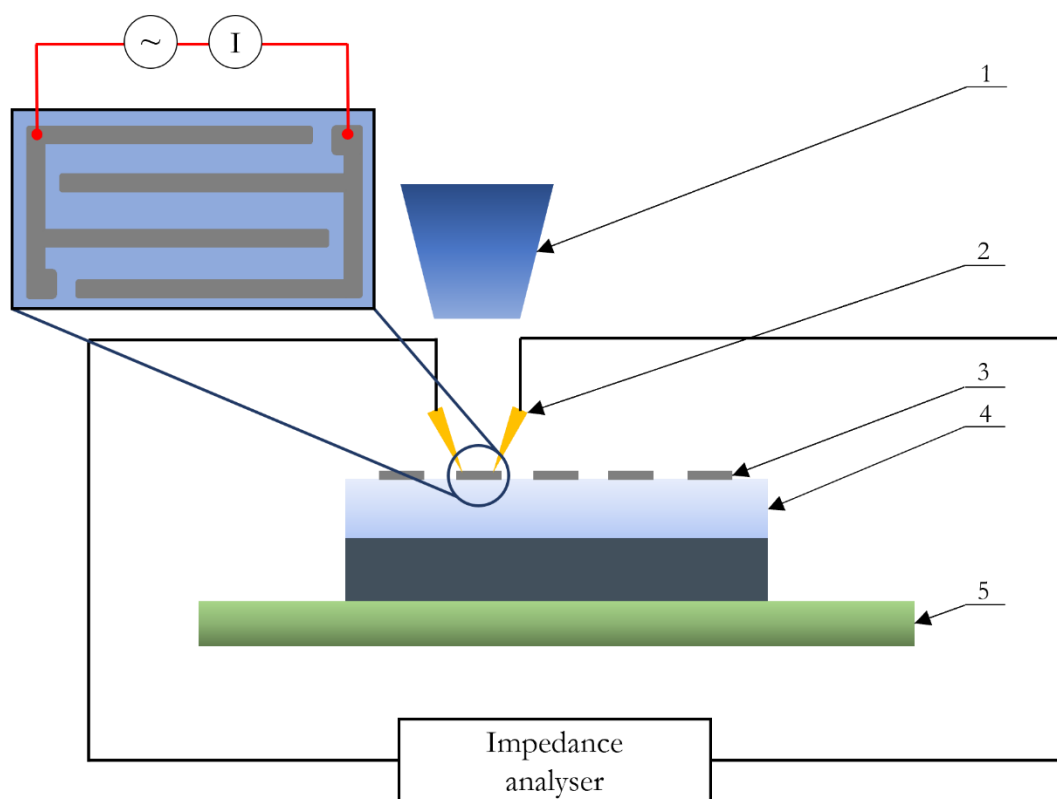


Figure 3.5: Schematic illustration of the microcontact measurement setup. 1 – microscope, 2 – adjustable micromanipulator with gold-plated steel needle, 3 – platinum electrode, 4 – LFP thin-film on substrate, 5 – heating stage

The measurement setup for the in-plane impedance measurements is shown schematically in figure 3.5. A vacuum microcontact arrangement was used, which allowed measurements to be performed in an inert gas atmosphere at different temperatures. The sample was placed in a vacuum chamber on a corundum heating plate coated with platinum. In order to be able to contact the sample, platinum finger microelectrodes were attached across the LFP thin-film surface (see section Photolithography for details). These platinum electrodes were then contacted via gold-plated steel needles, which were attached to movable micromanipulator. Due to the small area of the current collectors, the manipulators were controlled manually via software, while the positioning was monitored by a microscope equipped with a camera. To create an argon atmosphere, the chamber was evacuated several times and then argon was passed through the chamber at a constant overpressure, with the gas flow being monitored with a bubble counter. Measurements were carried out at different temperatures, starting at room temperature up to 450 °C set temperature, increasing in 50 °C steps, whereby the sample went through several heating and cooling cycles.

The first complete temperature cycle was performed with only one single microelectrode, while further temperature measurements were performed by measuring a large number of electrodes at one temperature and then cooling the sample back down to RT. This allowed observation of the stability of the layer under the influence of temperature, but it also resulted in the problem that repeated contacting of the current collectors damaged the platinum layer, which meant that not all electrodes could be measured at every temperature step.

Photolithography

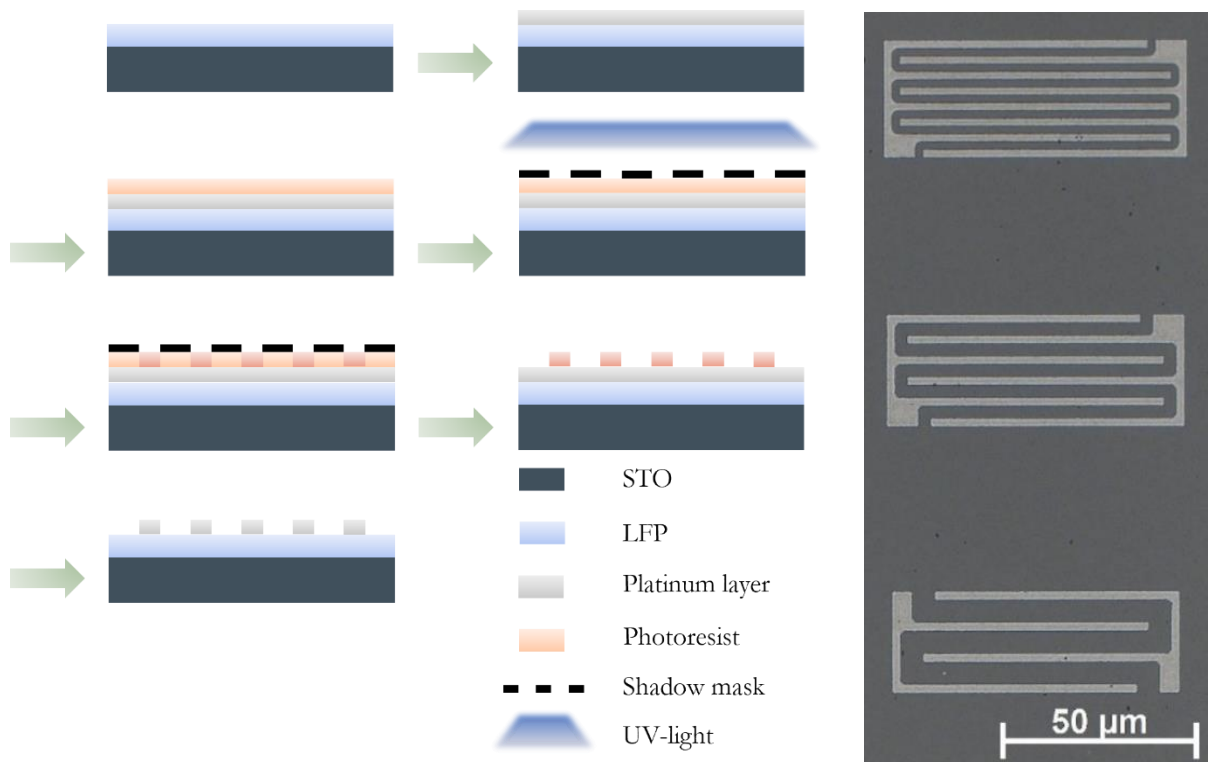


Figure 3.6: Workflow of ion beam etching photolithography (left) and fabricated platinum microelectrodes (right).

Platinum finger microelectrodes were deposited on the LFP sample (~50 nm LFP on STO (100)) surface by means of ion beam etching photolithography. The design of the microelectrodes was taken from Nanning et. al. (2017) [55]. The distances between the fingers of the current collectors measured 10, 15 and 28 μm, respectively, as shown in figure 3.6 (right), whereas on the left, the workflow of the lithography process is illustrated.

At first, a 5 nm titanium and 100 nm platinum layer were deposited on the sample, using the parameters of table 3.9. Then, the preparation was taken to a clean room to prevent contamination by dust. The sample was coated with 100 μ l photoresist (ma-N 1420 MicroResist Technology, Germany) using a spin coater (SCC-200 KLM, Schaefer Technology, Germany) with a rotation speed of 100 rpm and afterwards baked at 105°C for 2 minutes to pre-cure the coating. The surface was covered with a shadow mask to ensure that only the patterns of the microelectrodes were exposed to UV-light (40 sec, USH-350DP, 350W, Ushio Inc. Japan). This led to cross-linking of the polymer, which subsequently allowed unexposed parts of the photoresist to be removed with the help of a developer solution (60 sec, ma-D 533s, MicroResist Technology, Germany). After cleaning in deionised water for 15 sec, the success of the structuring was reviewed under the microscope. As there were still undeveloped areas, the sample was again swivelled in the developer solution for 5 sec and cleaned in de-ionised water for 15 sec. A summary of the parameters can be found in Table 3.11. The uncovered platinum areas were now removed by means of ion beam etching. For this purpose, the sample was transferred to a vacuum chamber and the etching process was carried out with a diffuse argon plasma, as (For parameters see Tab. 3.12). Finally, residual photoresist was removed by treatment with ethanol. Figure 3.6 (right) displays the result of the process, in the form of three representative electrodes.

Table 3.11: Parameters used for photolithography

Photolithography	
Photoresist [μ l]	100
Spin coater speed [rpm]	100
Temperature [°C]	105
Heating duration [min]	2
UV light exposure [s]	40
Developing time [s]	65

Table 3.12: Parameters used for ion beam etching.

Ion beam etching	
Working pressure [mbar]	9.4×10^{-4}
Beam voltage [V]	400
Beam current [mA]	15
Acceleration voltage [V]	80
Etching time [min]	24

In-plane Impedance Spectroscopy

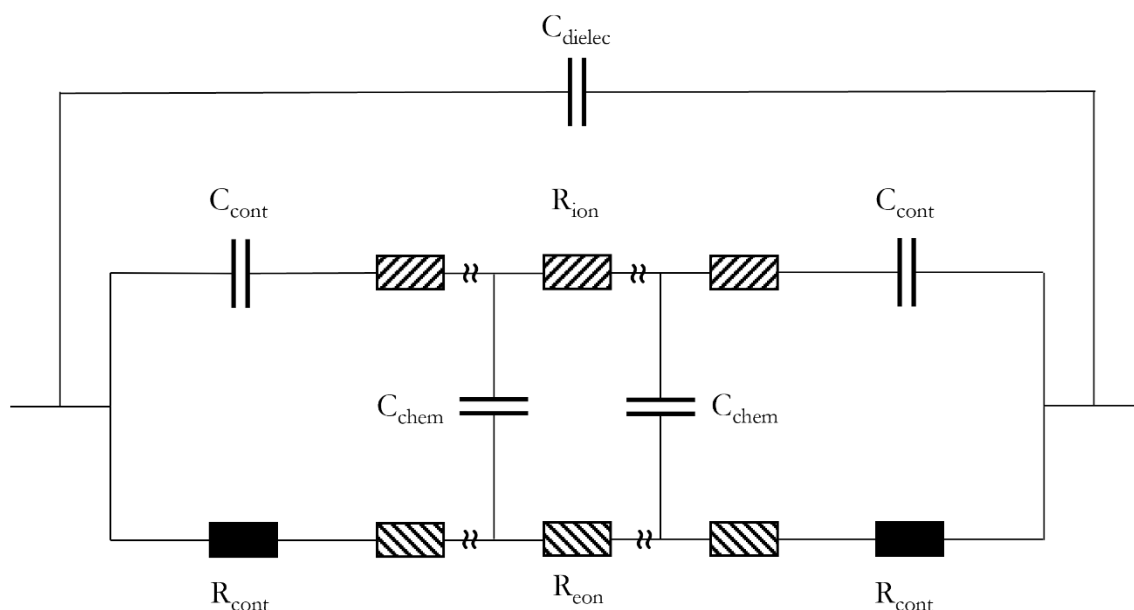


Figure 3.7: Transmission line equivalent circuit for electrode|MIEC|electrode, derived from figure 2.2.

The equivalent circuit for interpreting the transport phenomena in the given system is depicted in figure 3.7. As we have a symmetrical cell, consisting of electrode|LFP|electrode, the respective end points in the transmission line are to be considered equivalent. The terminals of the electronic rail can be represented as contact resistances, as this is where the exchange of electrons between the LFP and the platinum current collector takes place. However, this current collector behaves in an ion-blocking manner, represented by capacitors in the ionic rail. Therefore, in this measurement setup, the lithium content of the LFP thin-film cannot be altered. C_{dielec} denotes the dielectric capacitance of the whole sample consisting of substrate and LFP thin-film. At room temperature, due to the poor electronic and ionic conductivities, the respective contributions to the impedance cannot be separated, which is why only one semicircle can be observed in the impedance spectrum. This can be described by an $R||C$ element, where R is the total resistance (electronic and ionic) and C is the dielectric capacitance of the substrate.

For recording the impedance spectra a Alpha-A High Performance Frequency Analyzer with a POT/GAL Electrochemical Test Station (Novocontrol, Germany) was used. The applied voltage amplitude was 10 mV and measurements were carried out in a frequency range of 1 MHz to 10 mHz with 5 data points per decade.

4 Results and Discussion

4.1 Structural Evaluation

The fabrication of the LFP thin films was accompanied by structural investigation methods in order to monitor the quality of the layers and to incorporate the findings into the optimisation process. The results of this analysis for the respective substrates are presented in the following. A main aspect of the optimisation process was the determination of the optimal deposition, i.e. substrate temperature, as this turned out to be highly critical. This factor was further intensified by the modification of the heating element of the sputtering system throughout the course of this thesis.

4.1.1 Sapphire

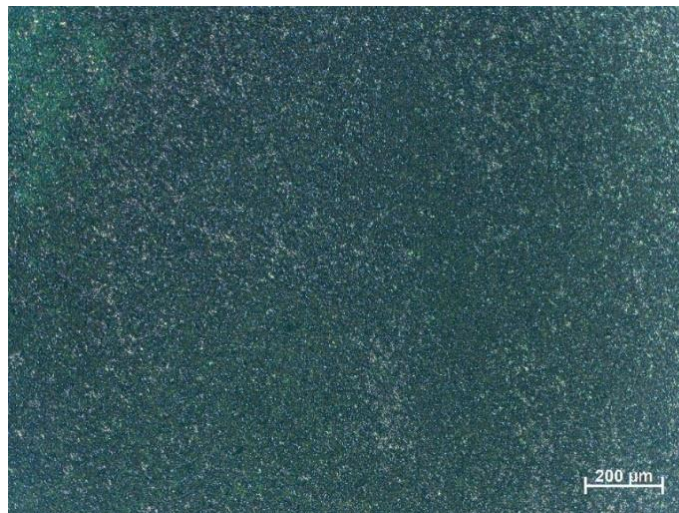


Figure 4.1: Image of an LFP layer deposited at 650 °C on Al_2O_3 (0001) taken via an optical light microscope.

In order to initially study the behaviour of LFP during deposition by RF magnetron sputtering, depositions at different substrate temperatures were carried out on sapphire (0001) single crystals. The heating element used here was heater-type A (corundum, with platinum wire running in serpentine underneath). Figure 4.1 gives an exemplary image of an LFP sample deposited on Al_2O_3 , taken via light microscope, while in figure 4.2 a comparison of the fabricated layers by means of XRD diffractograms is shown. These diffractograms were recorded in Bragg-Brentano geometry with $\text{CuK}\alpha$ radiation at an angle of $10\text{-}90^\circ$, as were most of the subsequent samples presented in this report. The dotted lines indicate the positions of the occurring LFP reflexes, on the basis of which the influence of the temperature can be observed.

It can be concluded that crystallisation of LiFePO_4 structure does not occur at too low a temperature ($450\text{ }^\circ\text{C}$), as no reflexes can be assigned here, therefore the sample is assumed to be amorphous. At high temperatures ($> 550\text{ }^\circ\text{C}$), foreign phase peaks are predominant in the materials diffraction pattern, while those of LFP show little or no intensity. This observation is reinforced by a visual evaluation of the surface texture, as it can be seen in figure 4.1 that no uniform thin film has formed. The diffractograms of the samples at $500\text{ }^\circ\text{C}$ and $550\text{ }^\circ\text{C}$ respectively suggest that crystalline LFP is present, although no preferred orientation can be discerned. Figure 4.3 highlights the two diffractograms. Peaks originating from the substrate are marked with (s), those from LFP with (*) and (°) stands for reflexes which can be assigned to FePO_4 . This comparison shows that the foreign phase FePO_4 is not as present at a deposition temperature of $550\text{ }^\circ\text{C}$, while distinct LFP reflexes can be determined. Features at approximately 15° and 25° , respectively, could not be assigned to a specific phase. Based on these findings, it was concluded that a substrate temperature of $500\text{-}550\text{ }^\circ\text{C}$ is required to promote crystallisation during deposition. However, it was also evident that sapphire (0001) was not suitable as a substrate for defined, crystallographically oriented LFP thin films.

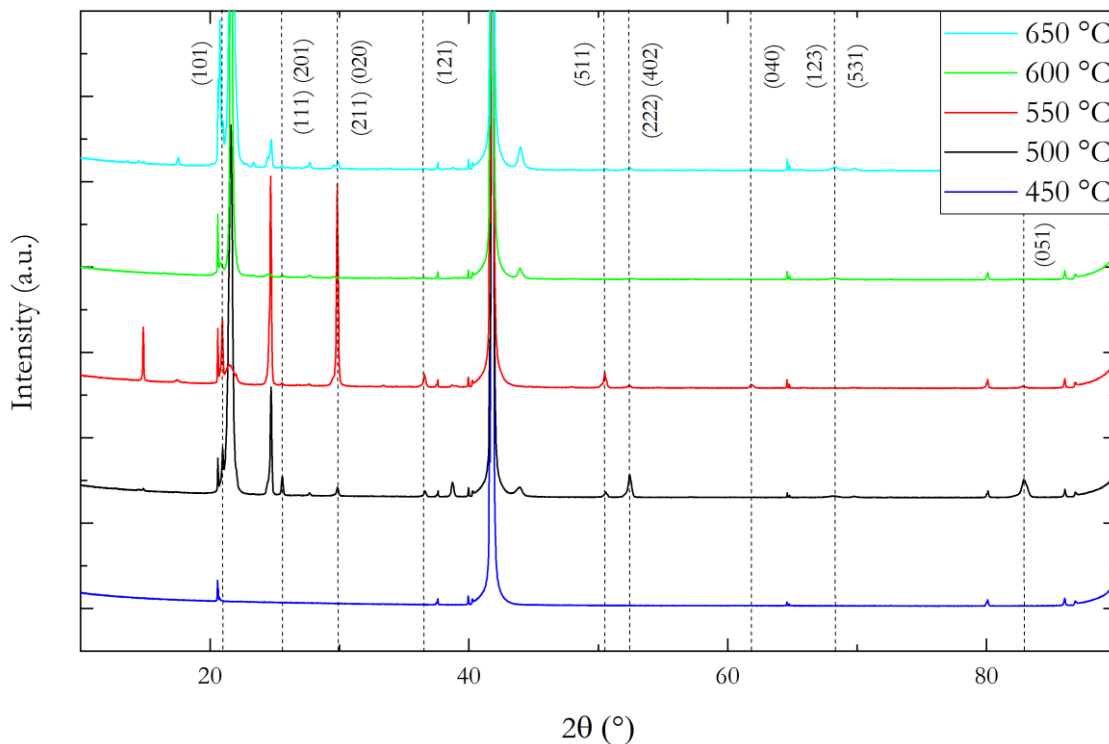


Figure 4.2: Comparison of X-Ray diffractograms of LFP deposited on Al_2O_3 for different deposition temperatures. Reflexes originating from LFP are indicated by the dotted lines.

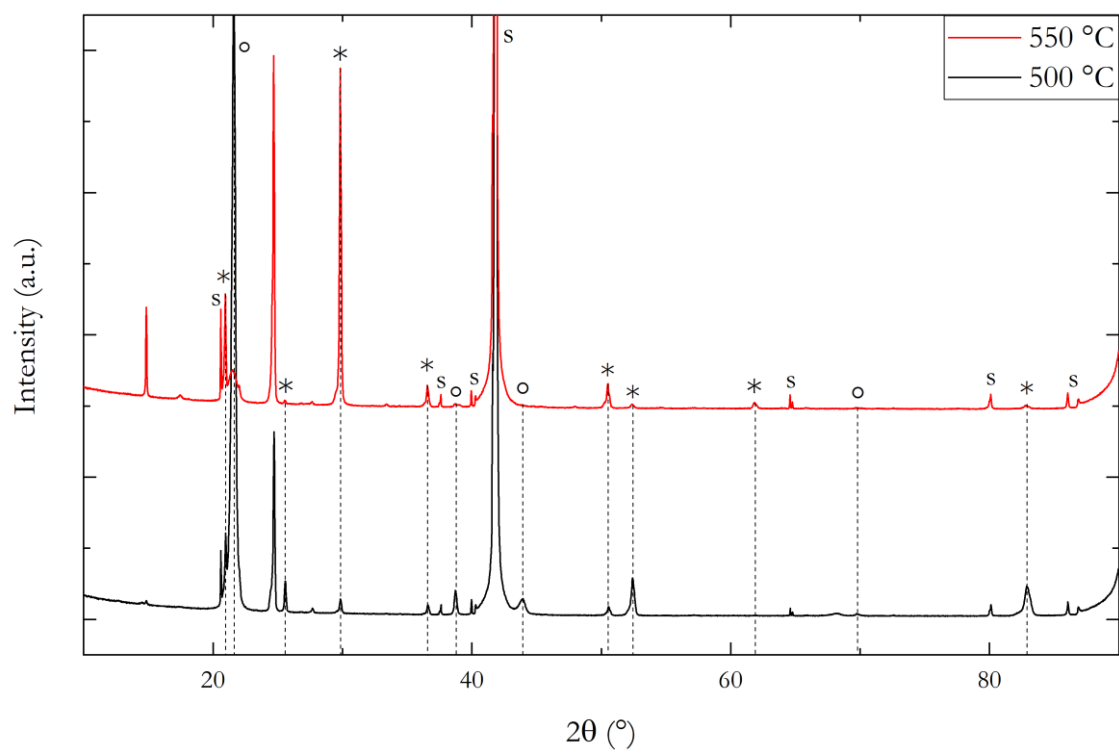


Figure 4.3: X-Ray diffractograms of LFP deposited on Al_2O_3 for deposition temperatures of 550 °C (red) and 500 °C (black), respectively. Reflexes originating from the substrate are marked with (*), while (s) is assigned to LFP and (°) to FePO_4 .

4.1.2 STO

STO (100)

STO (100) and (110) single crystals (5×5 and 10×10 mm²) were used for the further preparation and optimisation of the LFP thin films, with STO (100) being discussed in the first section and STO (110) as a substrate in the following. During the optimisation process, the heater setup was modified, which is why the influence of the temperature and, in particular, the type of heater will be treated in the following. Another point that will be dealt with shortly is the effect of argon flow on potential oxygen leakage, as it was assumed that this would promote the formation of foreign phases. In the first deposits, heater-type A was used. From the preliminary tests on Al₂O₃, it could be concluded that a deposition temperature of 500-550 °C favours the crystallisation of LFP in the desired form. It also showed that the process cannot take place at too low a temperature, therefore for further depositions on STO it was decided to orientate towards the upper limit, i.e. at 550 °C. Figure 4.4 shows the logarithmic representation of the diffractograms of samples deposited at 550 °C on STO (100) (10×10 mm²) for 120, 60 and 20 min, respectively. The symbol Δ indicates the reflexes of the foreign phase Fe₂O₃, while the numbers triplets in brackets () indicate distinct LFP reflexes. The segment between 55-80° is not shown for the purpose of simplicity.

The comparison (Fig. 4.4) shows that under given conditions, Fe₂O₃ can be identified as the foreign phase instead of FePO₄ compared to sapphire (Section 4.1.1). From the LFP reflections, a preferred orientation of the layer on STO (100) can be derived, which is defined by peaks for the crystallographic planes (410) and (820). In figure 4.5, the diffraction pattern of LFP on STO (100) (550 °C, 60 min) is highlighted and peaks were assigned to substrate (s), Fe₂O₃ (122) (Δ) and LFP (). While the preferred orientation of the thin-film in the (410) plane can be highlighted in this plot, it can also be observed that the number of foreign-phase peaks is lower compared to the layer with twice the thickness (120 min, Fig. 4.4). This is presumably due to the fact that a reduction in the layer thickness is accompanied by a general decrease in the intensity of the sample reflections. Compared to the layers produced on sapphire, the phase composition of the samples on STO is noticeably reduced in complexity, but nonetheless unassignable features are present.

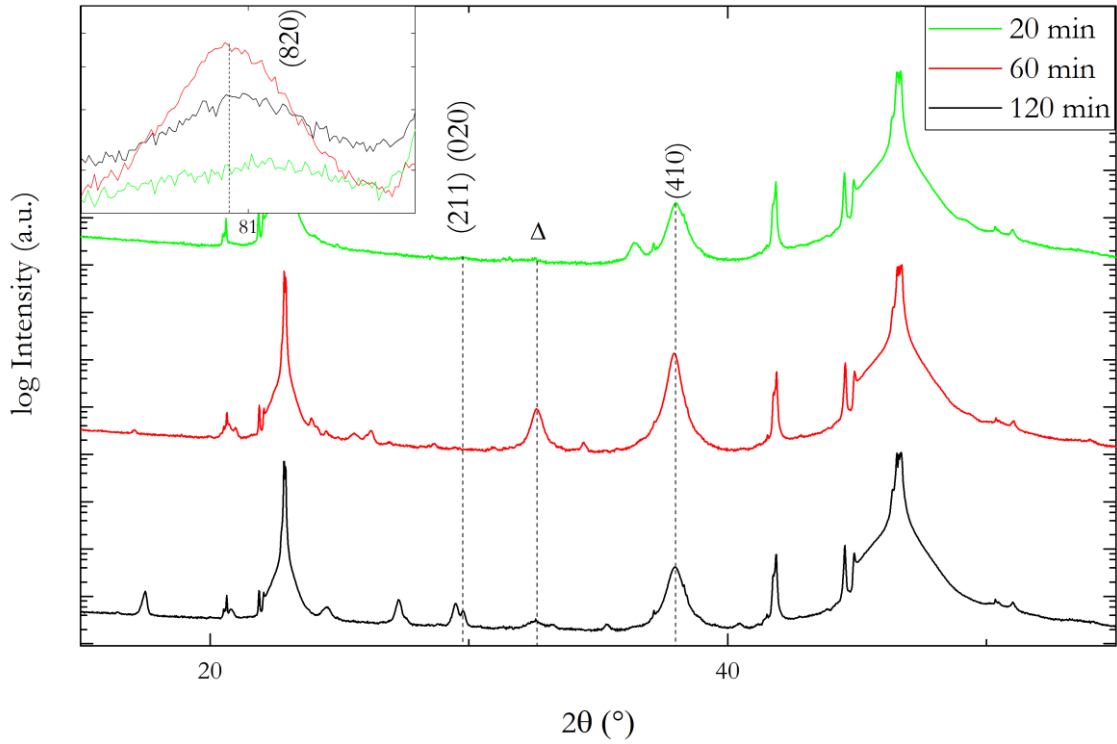


Figure 4.4: Diffractograms of LFP deposited on STO (100) (550 °C) for deposition times of 120 (black), 60 (red) and 20 min (green) . The symbols indicate the reflexes of the respective phases : () – LFP, Δ – Fe_2O_3

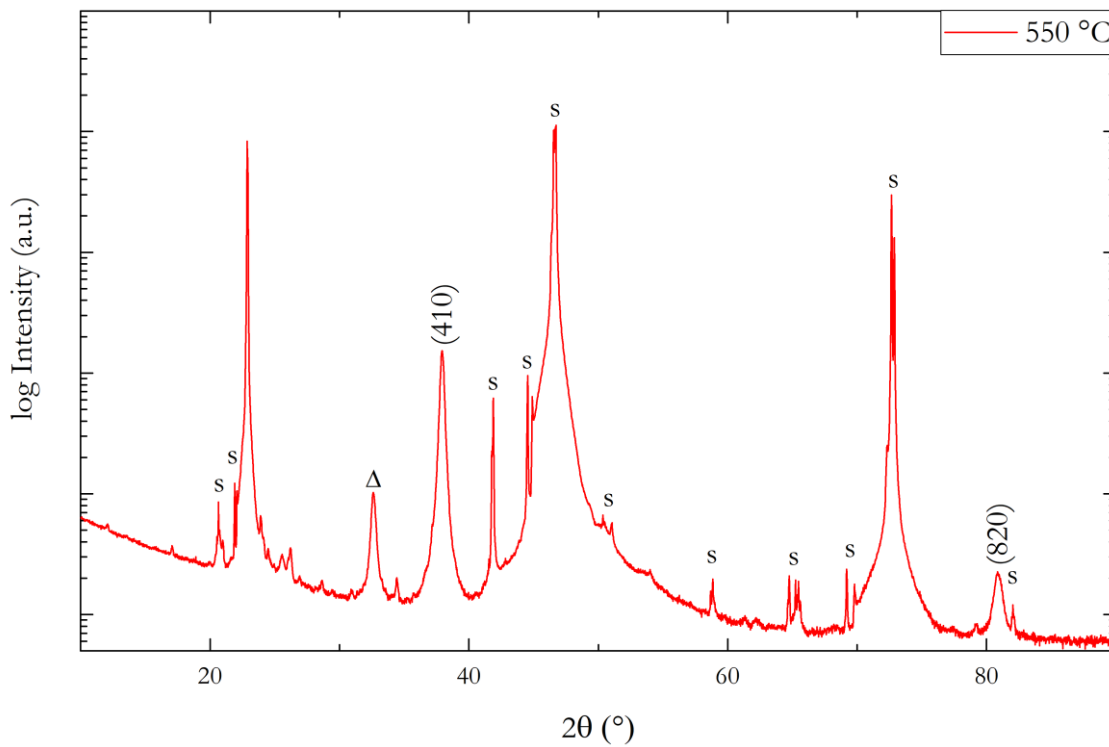


Figure 4.5: Diffractogram of LFP deposited on STO (100) (60 min) at a deposition temperature of 550 °C. The symbols indicate the reflexes of the respective phases : () – LFP, s – substrate, Δ – Fe_2O_3

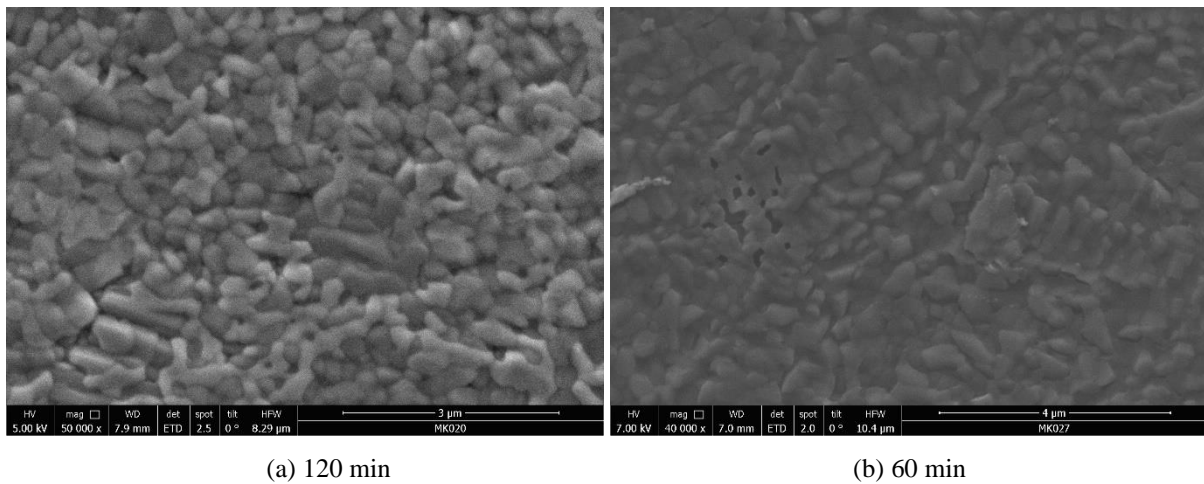


Figure 4.6: SEM images of LFP layers on STO (100) at (a) 120 min and (b) 60 min deposition time.

To highlight the influence of the layer thickness on the morphology, SEM images of the samples with a deposition time of 120 min (left) and 60 min (right) are juxtaposed in figure 6. Optically detectable irregularities of the surface are also reflected in investigations using a profilometer, where a decrease in roughness with a reduction in layer thickness can be observed. Sharp-edged objects in (b) are assumed to be platinum residues, as unsuccessful attempts have been made to apply a Pt-grid to the sample surface. According to the literature [44, 56, 57], the grain-like structure of the surfaces is the expected appearance of LFP under these manufacturing conditions. These findings have now provided the information basis for the deposition of LFP on STO (110) (see further below) and electrically conductive substrates such as Nb:STO (see 4.1.3 for details).

However, due to technical requirements, especially with regard to the heating power, the heating element of the sputtering system had to be redesigned at this point. A wound platinum spiral with a sample support made of a fused silica disc was used (heater-type B). Again, a temperature calibration was performed using a YSZ single crystal to correlate thermocouple and substrate temperature. Figure 4.7 and 4.8 show a comparison of two samples prepared using the nominally same parameters with the two types of heaters. The samples were each deposited at 550 °C (YSZ-calibrated substrate temperature) for 60 min, whereby the production only differed in the size of the substrate (10×10 mm² and 5×5 mm² respectively) and the type of heating configuration used. Looking at the images taken by light microscope in figure 4.7, a distinct difference between the two samples can be seen.

While (a) (fabricated with use of the corundum heater) shows a homogeneous surface, which has a roughness of only ~ 20 nm (examination via profilometer), the crystallisation of (b) (wound platinum wire) appears to be only in the initial stages. The blue dots, which extend over the entire surface, turn out to be elevations from the surface. This supports the hypothesis that these are a kind of crystallisation nuclei, whereas the surface characteristic is therefore an indication that the deposition temperature was below the required crystallisation level. Furthermore, this observation is substantiated by the comparison of the diffractograms of the two samples. (Fig. 4.8). The pattern of the sample prepared using the heating element with the fused silica sample holder hardly shows any reflexes apart from those originating from the substrate. This can be explained by the changed temperature distribution in the substrate compared to previous depositions, resulting from the modification of the heater setup. The conjecture was that due to the spiral shape of the platinum wire, an inhomogeneous heating of the quartz glass disc occurs, transferring this behaviour to the substrate. This resulted in a temperature gradient in the material and although a calibration was performed, the target crystallisation temperature could not be met when using the same parameters as with the previous heater setup, which was illustrated by figure 4.7 and 4.8. For this reason, further depositions were carried out at higher temperatures. However, the problem arose that a potential oxygen leak in the system could lead to the formation of undesired foreign phases through oxidation at elevated temperatures. These indications were counteracted by increasing the argon flow in order to displace a greater amount of oxygen from the sputter chamber.

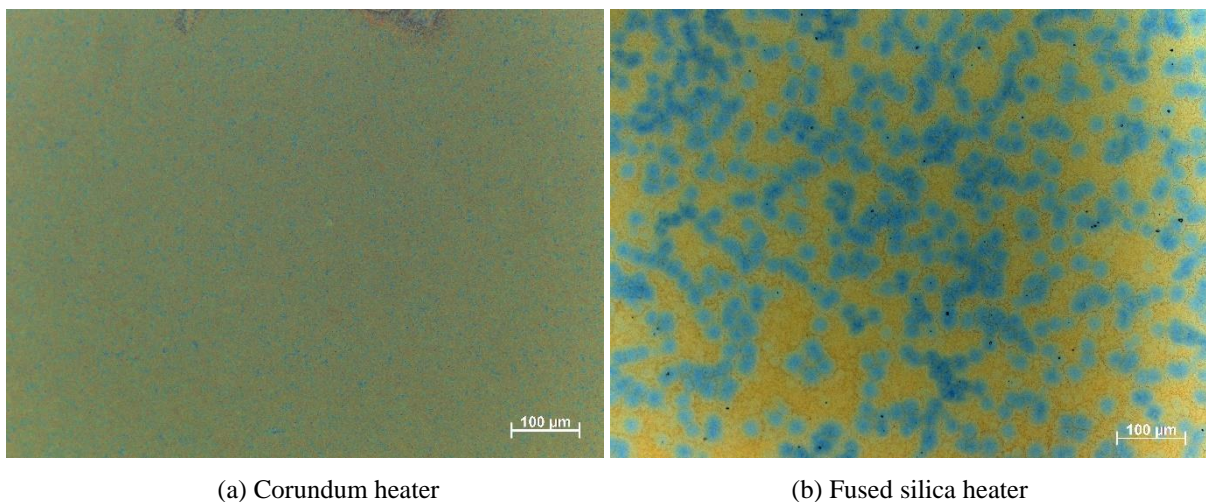


Figure 4.7: Optical light microscope images of LFP layer deposited at 550 °C calibrated substrate temperature on STO (100) using two different heater setups. These are corundum heater, with meandering platinum wire underneath (a) and a wound platinum spiral with a sample stage made of fused silica disc (b).

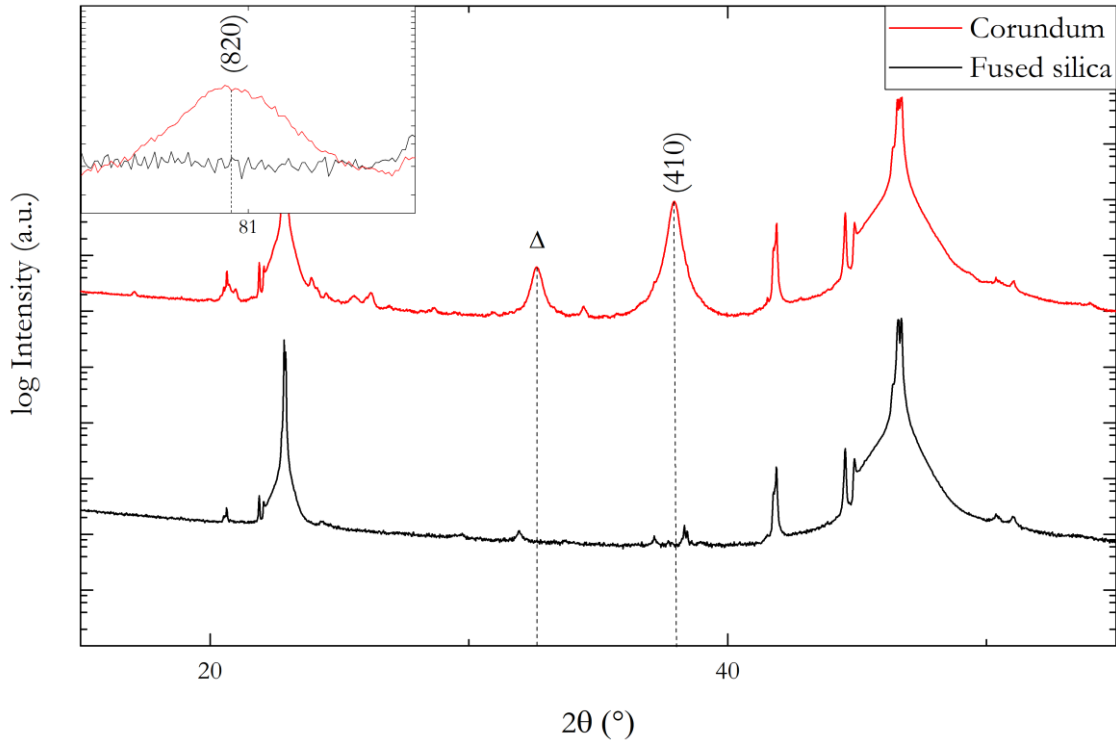


Figure 4.8: Diffractogram of LFP deposited on STO (100) (550 °C, 60 min) using different heater setups. The red line indicates the sample made on the corundum heating element and the black line the one fabricated on the heater using a fused silica disc as a sample stage. () – LFP, Δ – Fe_2O_3

Figure 4.9 shows the juxtaposition of two samples deposited at 600 °C with an argon flow through the chamber of 15 sccm and 50 sccm respectively. In figure 4.9 (a), the reflexes indicating the (410) and (820) plane, respectively, can be distinguished for both examples. Nevertheless, a significant difference in the number of foreign phase peaks can be identified. In 4.9 (b) the relevant range of 10-40 ° is shown enlarged. In addition to the reflexes for substrate (s), Fe_2O_3 (Δ) and the assignable LFP reflexes (*), the number of non-definable features is considerably increased for the sample with an argon flow of 15 sccm compared to 50 sccm. This characteristic can presumably be attributed to the fact that the ingress of oxygen into the chamber promotes oxidation of LFP at high temperatures. However, the foreign phases formed could not be assigned to any particular species on the basis of the diffractograms. The SEM images of the two samples are displayed in figure 4.10. Although the morphology of sample illustrated in figure (b) (50 sccm argon flow) shows irregularities and foreign phase features, the typical grain-like structure of LFP is clearly visible. In depiction (a) (15 sccm argon flow), however, these structures are covered by hexagonal formations that extend over the entire surface.

These results prompted the following experiments to be carried out with an increased argon flow, whereby a reduced flow rate of 45 sccm was chosen as suitable, since on the one hand 50 sccm reflects the maximum of the MFCs capacity and on the other the wear of the turbopump could thus be reduced.

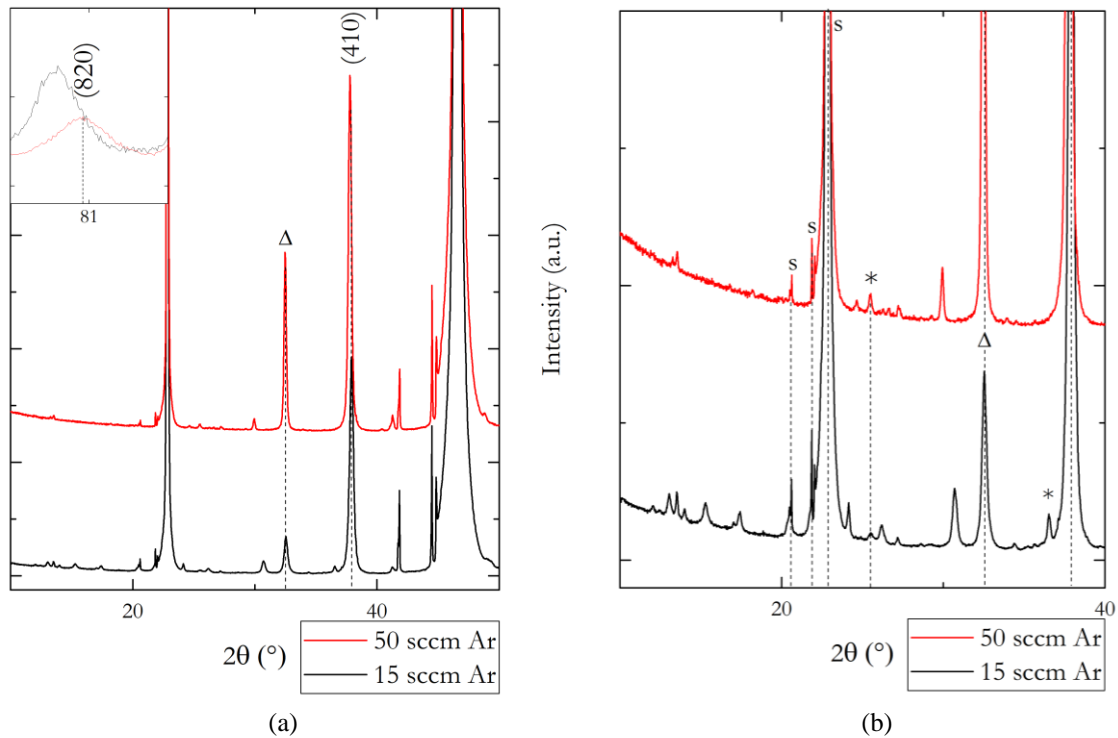
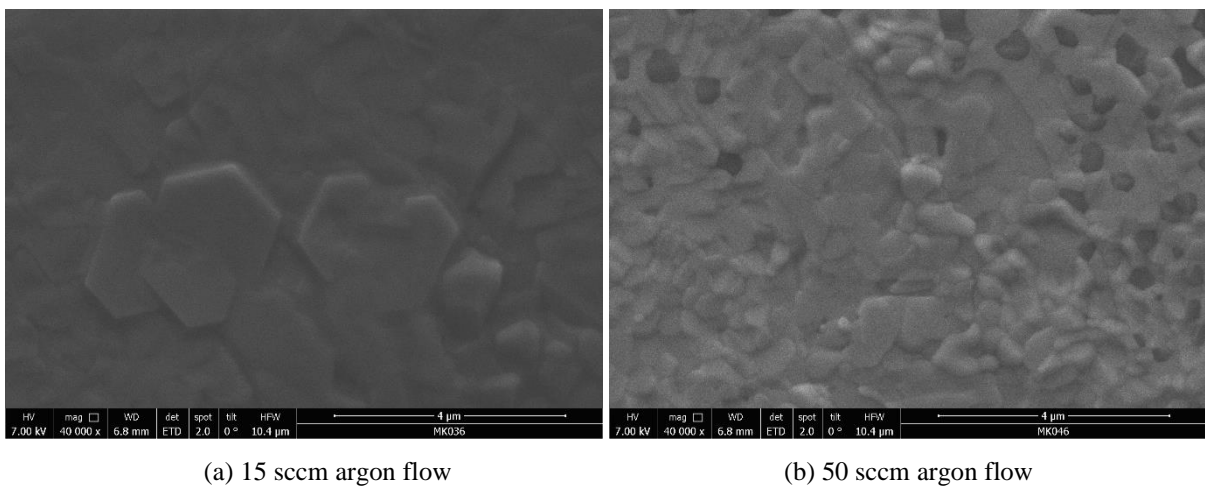


Figure 4.9: Diffraction patterns of LFP deposited on STO (100) (600 °C) with an argon flow of 15 sccm (black) and 50 sccm (red) respectively. (b) represents an enlarged section of the relevant area of the diffractogram (a).

() – LFP, s – substrate, Δ – Fe₂O₃



(a) 15 sccm argon flow

(b) 50 sccm argon flow

Figure 4.10: SEM images of LFP thin films deposited on STO (100) at 600 °C with an argon flow of (a) 15 sccm and (b) 50 sccm, respectively.

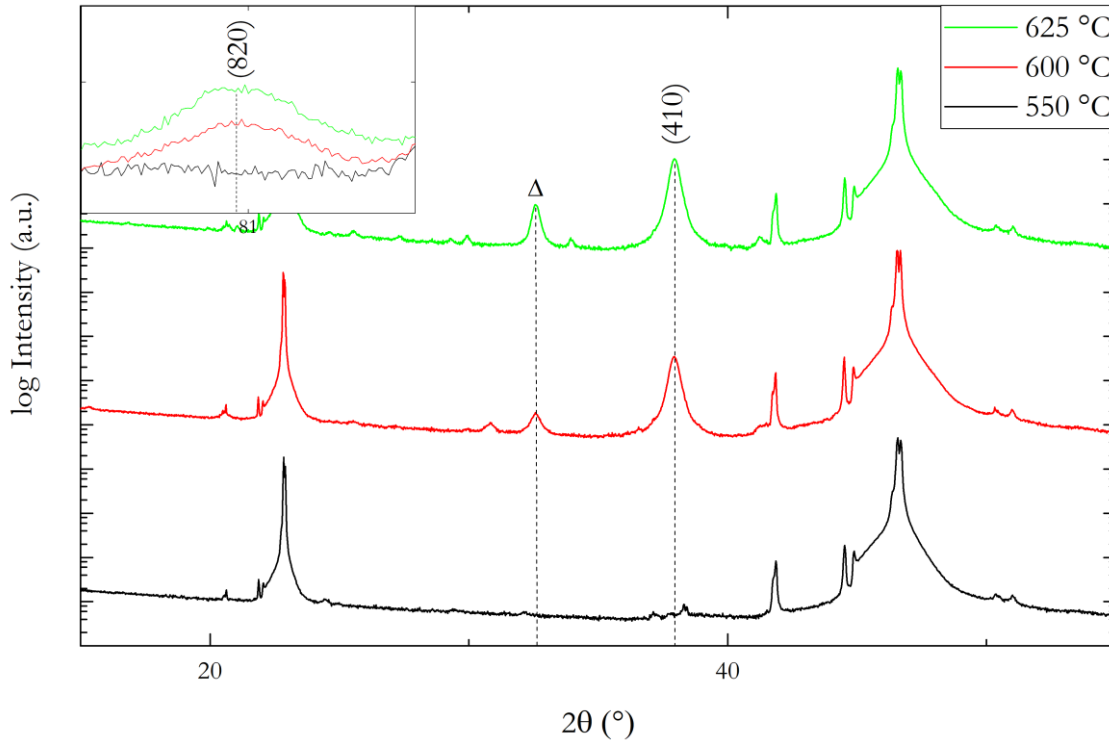


Figure 4.11: Diffraction patterns of LFP deposited on STO (100) at temperatures of 550 (black), 600 (red) and 625 °C (green) for 60 min, respectively. () – LFP, Δ – Fe_2O_3

As explained previously, the effect of the newly established heater on the homogeneity of the temperature distribution in the substrate was not ideal, therefore a further development of the sample holder was carried out, with the aim of increasing this homogeneity. The fused silica disc was coated with LSF on the underside and then annealed (heater-type C). To prevent the surface of the disc from being sputtered with target material, a corundum disc was made as a cover where there was a $\sim 10 \times 10 \text{ mm}^2$ cut-out for the substrate. A temperature calibration for the respective substrates was performed. To investigate the behaviour of the new configuration, a temperature optimisation was carried out, as depicted in figure 4.11. Shown are the diffractograms of three samples deposited on STO (100) ($5 \times 5 \text{ mm}^2$) at 550, 600 and 625 °C for 60 minutes, using a shadow mask to avoid sputtering LFP on the edges of the substrate. This was done in order not to falsify potential further electrochemical investigations by LFP around the edges. The diffraction patterns in figure 4.11 illustrate that after modification of the sample stage, still deposition temperatures of $\sim 600 \text{ °C}$ are required to obtain crystalline LFP films in the expected orientation. With increasing temperature, however, the Fe_2O_3 (Δ) reflex emerges, which, despite the increased argon flow, is due to the enhanced oxidation of the material at high temperatures. A deposition temperature of 550 °C proves again to be insufficient for the crystallisation of LFP in this setup, which is clarified in Figure 4.12.

Optical light microscopy as well as SEM images of the layers deposited at 550 °C and 600 °C demonstrate the behaviour that was already observed with the previous heater configuration (cf. Fig. 4.7). While the microscopy image of the sample produced at 550 °C (a) indicates a type of crystallisation nuclei (blue spots), which could be specified as island-shaped elevations after profilometric examination, the one of the sample deposited at 600 °C (b) shows a comparatively homogeneous surface morphology. Investigations using SEM confirm these observations. In picture 4.12 (d) (600 °C) the desired structure of the LFP material can be observed, but there are also contaminations on the sample. These are not measurement artefacts, as examinations with the profilometer also revealed a very high roughness (~ 60 nm) of the surface. Since the sample deposited at 625 °C also exhibited a high surface roughness, the influence of the shadow mask on the result of the layer production was investigated, as this was suspected to have an effect on the homogeneity of the layer growth.

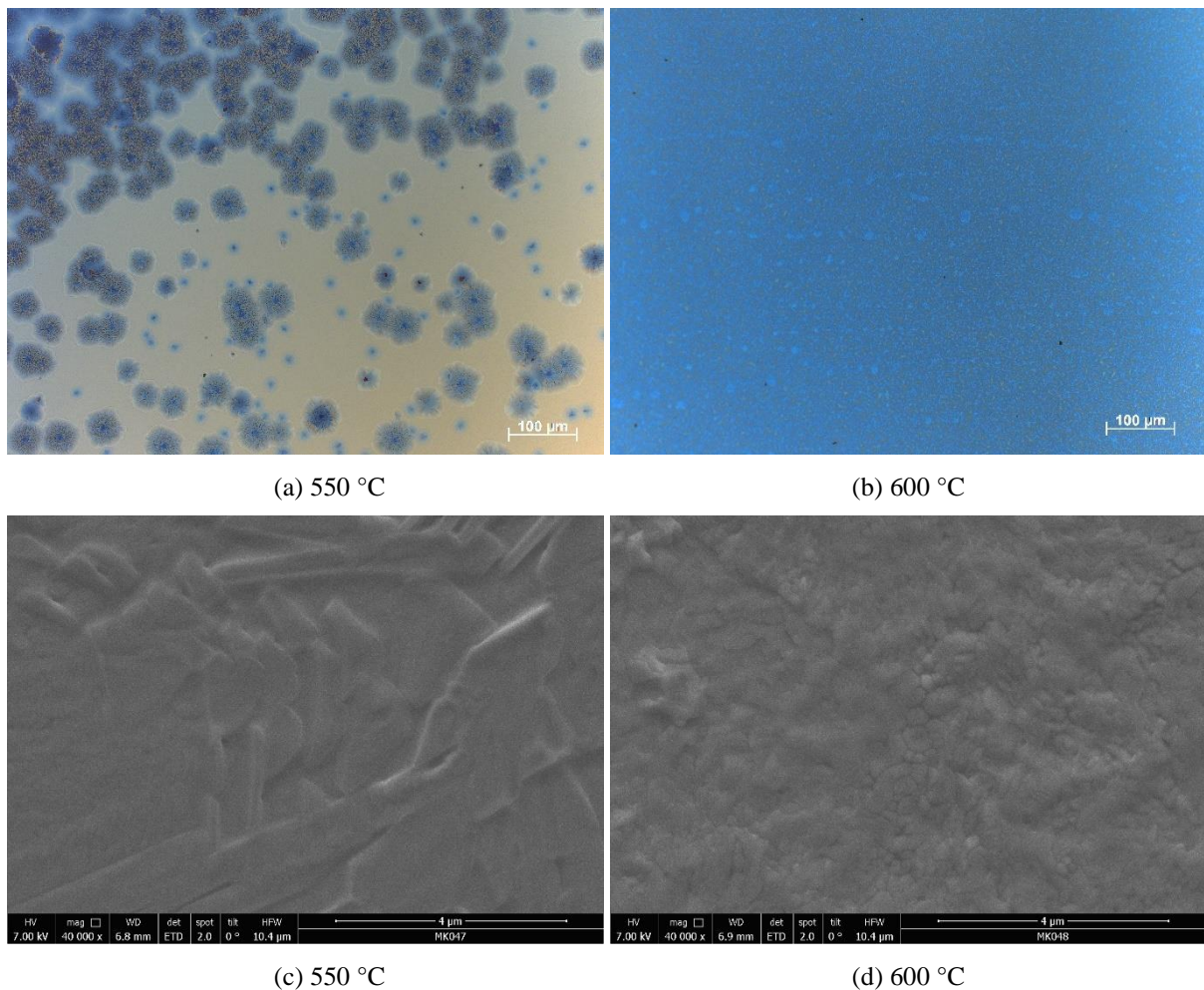


Figure 4.12: Optical light microscope (a, b) and SEM (c, d) images of LFP thin films deposited on STO (100) (60min) at 550 °C and 600 °C.

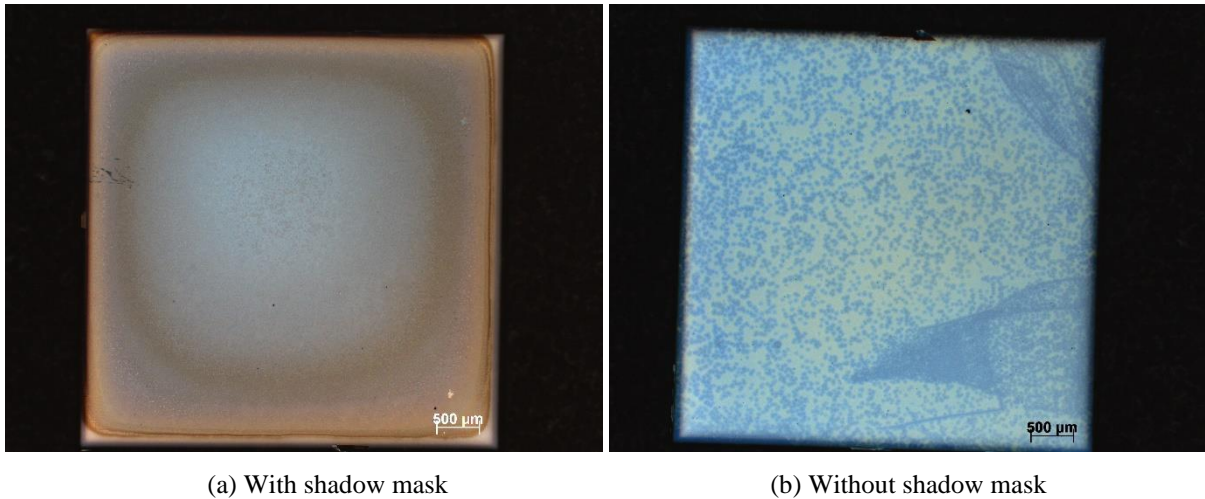


Figure 4.13: LFP samples deposited on STO (100) ($5 \times 5 \text{ mm}^2$) at $625 \text{ }^\circ\text{C}$ with shadow mask (a) to keep edges clear and without shadow mask (b).

In Figure 4.13 the samples deposited at $625 \text{ }^\circ\text{C}$ with (a) and without shadow mask (b) are depicted. A significant difference in the appearance of the layers can be identified, whereby in (a) the influence of the mask is clearly visible at the edges of the surface. This also affects the actual temperature of the substrate, respectively the distribution. Figure 4.13 (b) shows the typical structure of deposition a too low temperature, which is also indicated by the diffractograms of the samples given in figure 4.14 (a). While distinct LFP reflexes can be identified in the sample with a shadow mask, only substrate peaks are appearing in the sample without a shadow mask. In fig. 4.14 (b) the surface of the sample with mask is illustrated by SEM. Here the LFP texture is clearly visible and when comparing with image 4.12 (d) an improvement of the morphology with the temperature can be seen, which was also evident in the diffraction patterns (4.11).

It can be assumed that a further increase in temperature would lead to a refinement of the layer quality, but due to a technical defect of the sputtering device, this was not possible to verify in the course of this work.

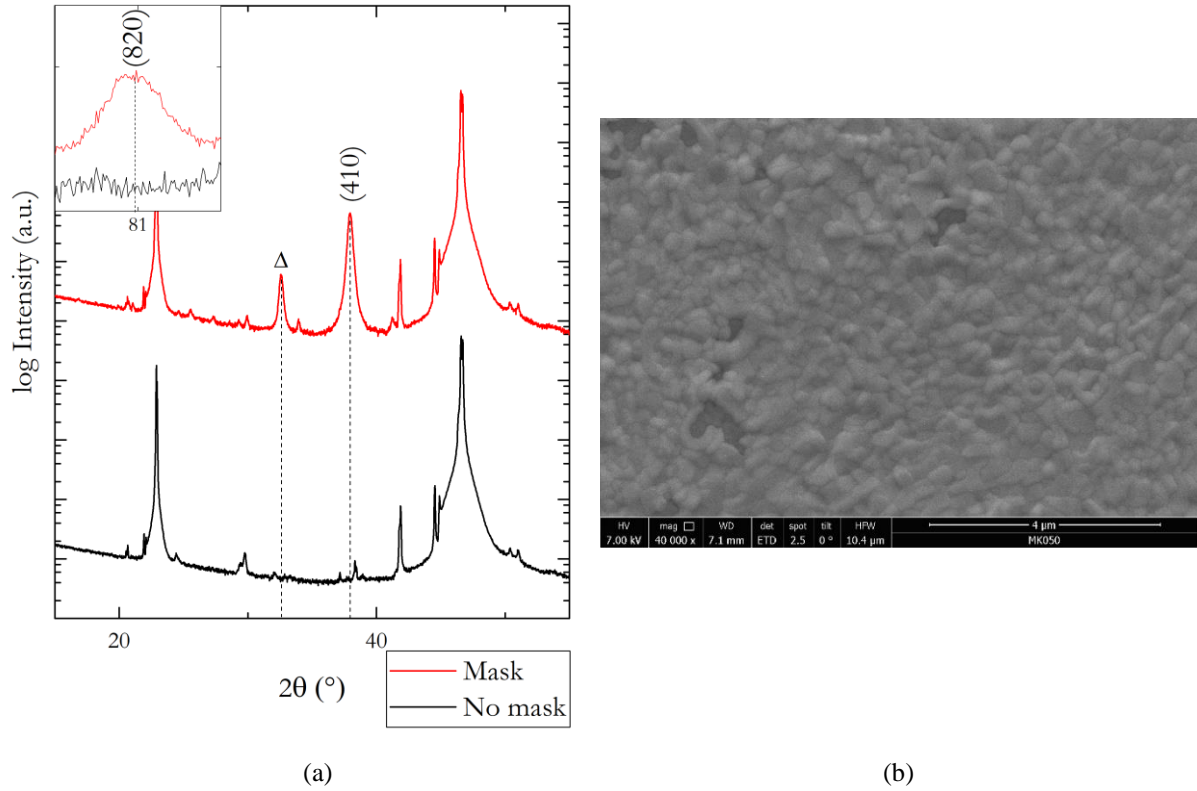


Figure 4.14: Diffractogram of samples prepared on STO (100) ($5 \times 5 \text{ mm}^2$) at $625 \text{ }^\circ\text{C}$ with and without shadow mask (a) and SEM image of the layer with shadow mask (b). () – LFP, Δ – Fe_2O_3

STO (110)

For the investigation of ambipolar diffusion in LiFePO_4 thin films, the preparation of crystallographically oriented films is of crucial importance, since the transport of charge carriers through the crystal structure exhibits anisotropic behaviour. (See section 1.2) Based on information from the literature, STO (110) single crystals were therefore considered as a possible support material. This substrate offered the advantage over STO (100) that, according to the literature, a preferential orientation of the thin-film in the (100) plane could be observed. [58] However, no extensive temperature optimisation was carried out on pristine substrate as previously with STO (100), but instead it was considered for application as a base for electrically conductive layers such as SRO and LNCO. These results are presented in detail in section 4.1.4.

Depositions of LFP on pristine STO (110) ($5 \times 5 \text{ mm}^2$) were performed solely at $550 \text{ }^\circ\text{C}$ and $600 \text{ }^\circ\text{C}$ deposition temperature. Layers were prepared using the heating element made of wound platinum wire with uncoated fused silica disc as sample holder. The obtained diffractograms of the samples (Fig. 4.16) draw a similar picture as on STO (100).

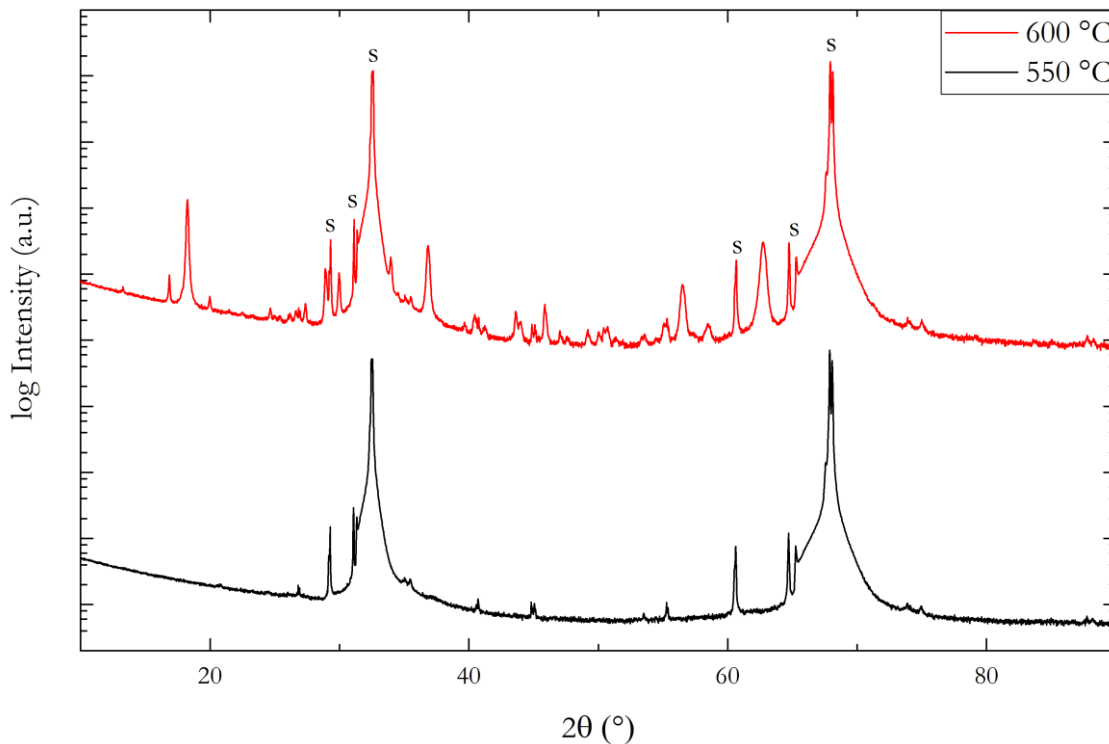


Figure 4.15: LFP deposited on STO (110) ($5 \times 5 \text{ mm}^2$) single crystals at $550 \text{ }^\circ\text{C}$ and $600 \text{ }^\circ\text{C}$. Reflexes marked with (s) indicate the substrate. Further features could not be assigned to distinct phases.

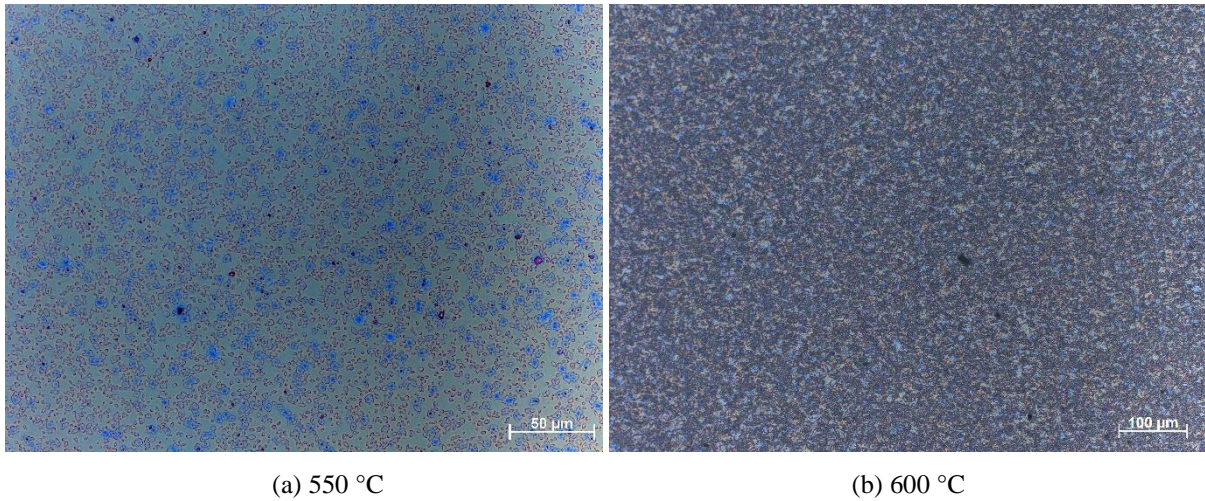


Figure 4.16: Optical light microscope images of samples deposited on STO (110) ($5 \times 5 \text{ mm}^2$) at 550 °C (a) and 600 °C (b).

At 550 °C, as with STO (100), no distinct LFP reflex is assignable, although the surface structure shown in Figure 4.15 (a) differs from that of comparable samples on STO (100) (cf. 4.7 (a) and 4.12 (a), respectively). At a deposition temperature of 600 °C, additional features can be seen in the diffraction pattern, but these cannot be defined with certainty. The microscopy images of this sample indicate that the surface structure of the layer present is not homogeneous, which is supported by the measured roughness ($\sim 200 \text{ nm}$).

With depositions on STO (110)|LNCO, an acceptable layer result could be achieved, which is why equipment problems with samples produced on pristine STO (110) cannot be ruled out. A more significant impact on the layer quality, however, presumably has the interdiffusion that occurs between STO and LFP, which is inhibited by LNCO as a buffer layer. For more details on this occurring phenomenon, see section 4.1.6 TEM.

4.1.3 Nb:STO

Niobium doped STO (100) ($5 \times 5 \text{ mm}^2$) single crystals were used as substrate for LFP thin films due to their electrically conductive properties. In this section, the structural investigation of the films is discussed, while the electrochemical treatment takes place in section 4.2. Based on the positive results obtained from the optimisation process on STO (100), depositions were carried out at nominal YSZ temperatures of $550 \text{ }^\circ\text{C}$ with a deposition time of 60 min and 20 min, respectively. The heater-type A was used. At this stage of the project, the enormous influence of temperature on the coating quality was not yet fully understood, which is why a calibration with a YSZ single crystal was used as a temperature reference. However, the temperature behaviour of Nb:STO and YSZ cannot be treated in the same way, since heat transfer in vacuum mostly occurs via radiation exchange and Nb:STO exhibits increased absorption compared to the transparent YSZ. Therefore, it can be concluded that the actual substrate temperature of the Nb:STO single crystal was higher than determined by the calibration.

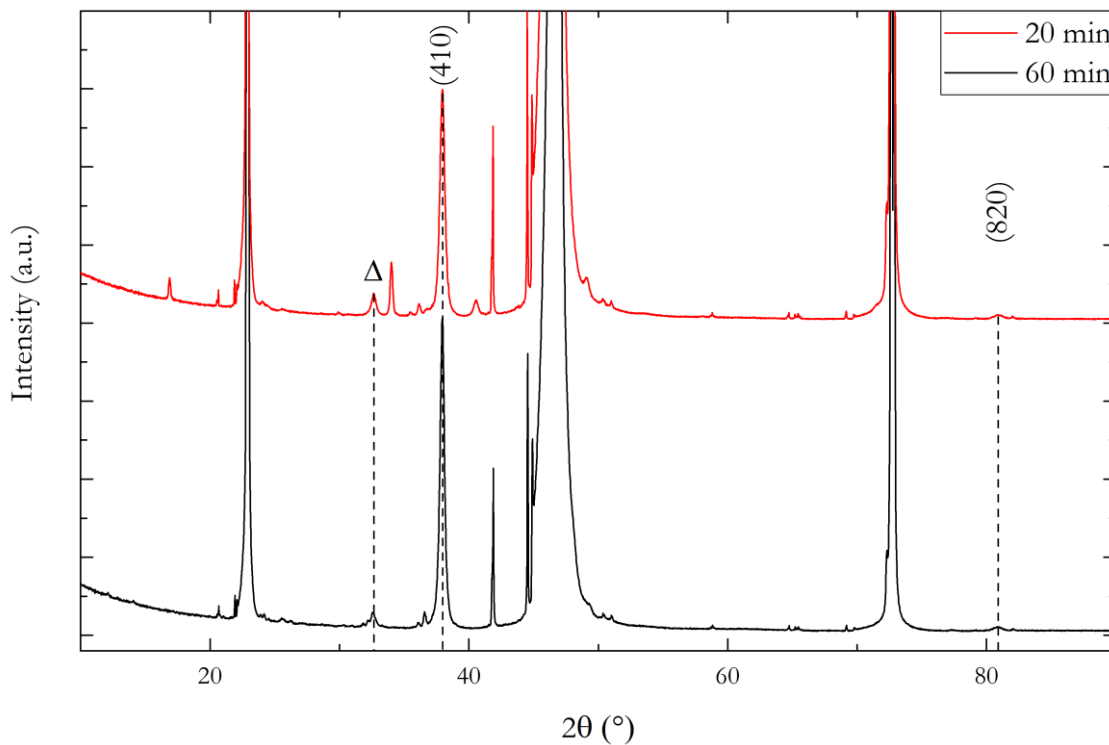
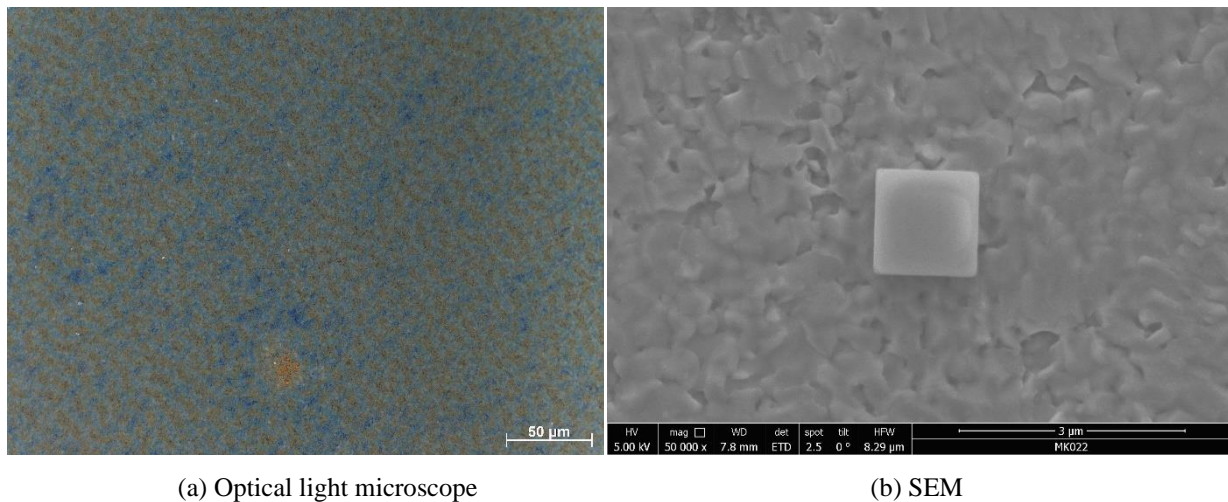


Figure 4.17: Diffractograms of LFP deposited on Nb:STO (100) ($5 \times 5 \text{ mm}^2$) at $550 \text{ }^\circ\text{C}$ for 20 (red) and 60 min (black), respectively. () – LFP, Δ – Fe_2O_3



(a) Optical light microscope

(b) SEM

Figure 4.18: Light microscope (a) and SEM (b) images of LFP deposited on Nb:STO (100) at 550 °C for 60 min.

Diffraction patterns illustrated in figure 4.18 show the samples prepared on Nb:STO. The LFP reflexes of planes (410) and (820), already mentioned with STO (100) can be identified, as well as the Fe_2O_3 reflex. For the thin film deposited for 20 min (red), numerous unassignable peaks are visible. Figure 4.19 displays the thin-film deposited for 60 min, studied via light microscope (a) and SEM (b). In the latter, a cubic structure can be distinguished on the surface. This might be the result of the deposition process, but it might also be an artefact caused by an electrochemical treatment. This sample was investigated in the 'liquid cell' before the diffraction pattern was acquired.

As discussed in section 2.3, it was noticed that a high contact resistance occurred between the platinum wire, which provides the electrical contact of the sample in the liquid cell, and Nb:STO. Therefore, an attempt was made to apply a conductive coating as a buffer layer on the rear of the substrate. LNCO was sputtered onto the bottom side using PLD, covered with a platinum layer and then LFP was deposited on the front side of the Nb:STO (100) (10×10 mm) single crystal. (Fig. 4.20 and 4.21) Here, heater-type B was used. The deposition temperature was 550 °C according to the calibration with a pristine Nb:STO, but due to the LNCO and platinum layer on the backside, the surface temperature of the substrate might have been lower, since the platinum layer in particular contributed to the reflection of the thermal radiation.

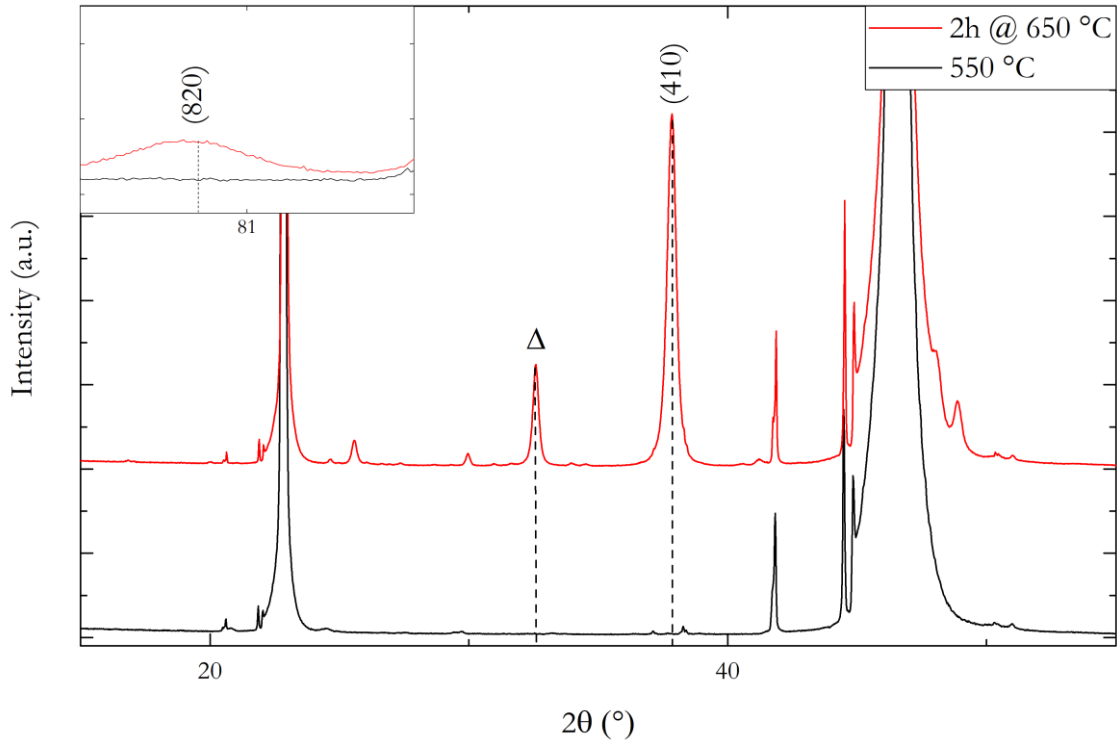
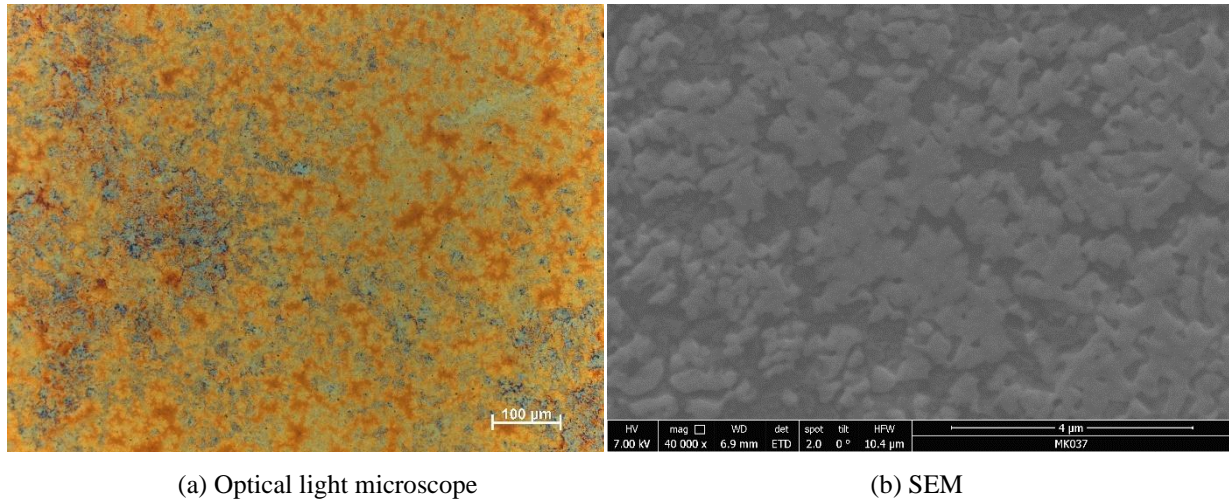


Figure 4.19: Diffraction pattern of LFP deposited on Pt|LNCO|Nb:STO (100) (10x10 mm) at 550 °C (black) and after annealing for 2h at 650 °C under sputter conditions (red). () – LFP, Δ – Fe_2O_3

The assumption that the actual substrate temperature is below the calibrated temperature for the new heater setup is strengthened by consulting the diffractograms shown in Figure 4.21 as a black line. Apart from substrate reflexes, no peaks can be detected, which is an indication of a low deposition temperature. To study the behaviour of the same layer at elevated temperatures, the sample was heated again in the sputtering chamber under given conditions at 650 °C for 2 hours. Under these settings, crystallisation of the amorphous material occurs and the anticipated reflexes emerge. Here again features of foreign phases can be discerned. However, the investigations with both light microscope and SEM demonstrate that the texture of the surface does not resemble the one known from tests on STO (100), although the diffractograms show a similar shape. The irregularity of the surface is also reflected in a roughness of ~ 50 nm. One possible explanation for this behaviour is that the temperature for the annealing step is above a critical temperature and thus homogeneous crystallisation cannot occur, which is potentially enhanced by the repeated heating and cooling steps.



(a) Optical light microscope

(b) SEM

Figure 4.20: Light microscope (a) and SEM (b) images of LFP deposited on Nb:STO (100) at 550 and then annealed for 2h at 650 °C under sputter conditions.

4.1.4 SRO/LNCO

SRO

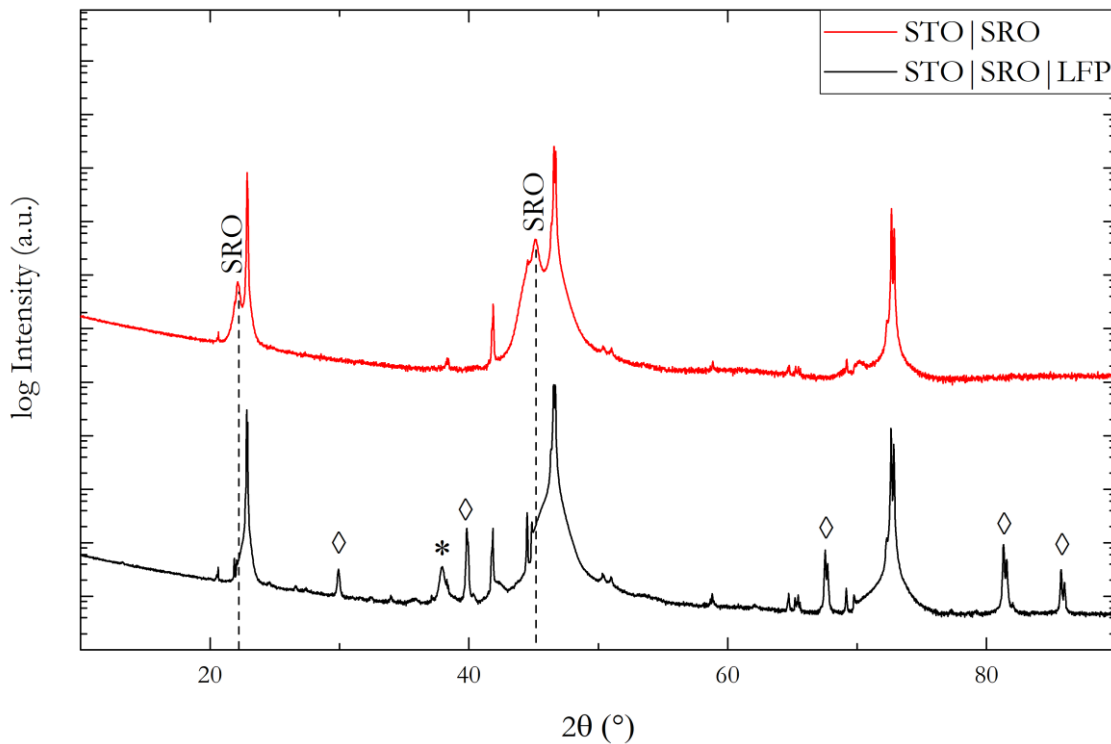


Figure 4.21: Diffraction patterns of SRO deposited (via PLD) on STO (100) (5x5 mm) (red line) and LFP deposited on STO|SRO at 550 °C (black). Peaks originating from platinum paste are indicated with \diamond . * – LFP

A ~50 nm SRO layer was deposited on a STO (100) (5×5 mm²) single crystal using PLD (see Table 3.7 for parameters) to serve as an intermediate layer between STO and LFP. The deposition was carried out at a nominal temperature of 550 °C for 39 min. As with the first samples on Nb:STO, the non-negligible influence of the substrate on the actual deposition temperature was not yet fully understood, so the deposition on SRO was performed using the existing YSZ temperature calibration. As a result, the actual temperature was presumably higher than the nominal 550 °C. The result of the deposition is shown in Figure 4.21 in the form of the diffractogram (black line). For comparison, the diffraction pattern of the SRO layer on STO prior to deposition is also depicted (red line). The reflexes labelled with \diamond are originating from the platinum paste, which was applied to one edge of the sample to electrically connect the front and back side. Highlighted with * is the (410) reflex of LFP, which was expected on STO (100). When comparing the two figures, it is evident that the peaks at ~22.2° and ~45.2° attributable to SRO are not detectable in the diffractogram of the LFP layer, highlighted through the dotted lines.

This behaviour suggests that SRO is not stable under given sputtering conditions. Therefore, a non-ambient XRD measurement was performed at temperatures of 25-700 °C under argon atmosphere. The data obtained are presented in Figure 4.22, with the temperature profile of the measurement programme plotted in Figure 4.23. The plot in Figure 4.22 illustrates that the SRO layer is not stable at elevated temperatures under argon atmosphere, which is expressed by the disappearance of the SRO reflexes in the diffractograms with increasing temperature. Up to a temperature of 500 °C, the SRO reflexes are clearly visible. At 600 °C, there is a noticeable change in shape and a shift in position to higher angles. Ultimately, at 700 °C, there are no more peaks that can be assigned to SRO, which suggests that the stability limit of the material lies at around 600 °C under the given conditions.

The black and olive green graph represent the start and end point of the measurement at 25 °C. (cf. Fig. 4.23) This modification of the layer structure clearly contributes to the loss of electrical conductivity.

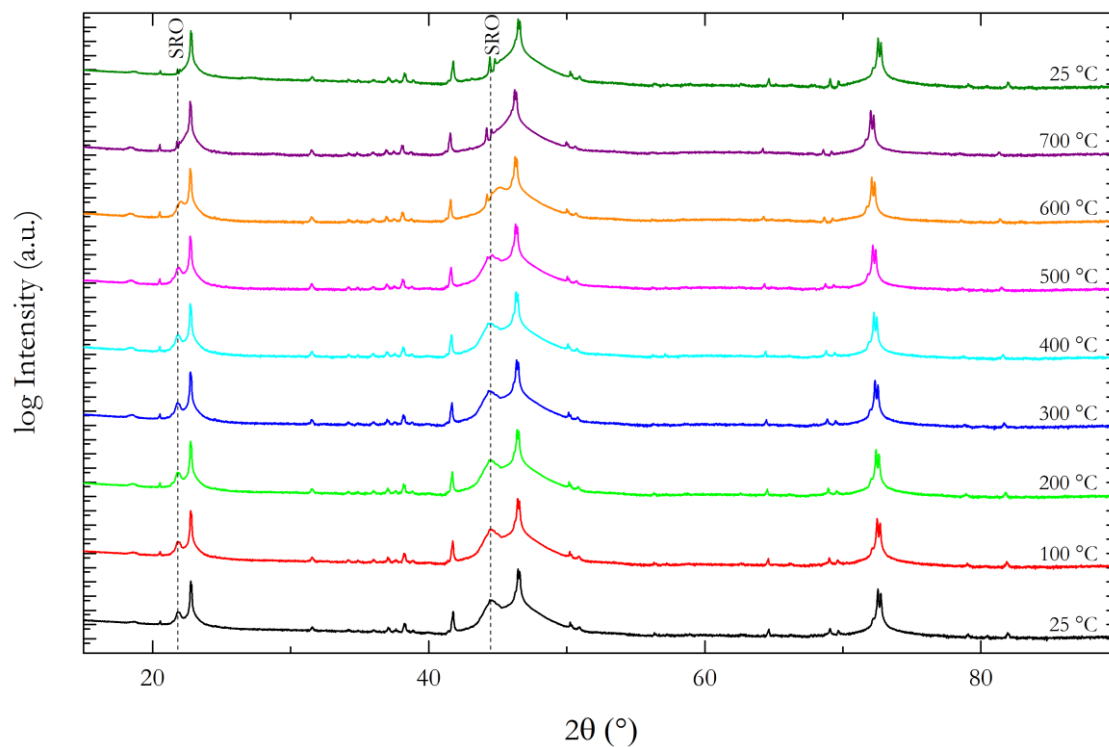


Figure 4.22: Non-ambient temperature XRD measurements of SRO on STO (100) conducted under argon atmosphere for 25-700 °C. The T-profile of the measurement programme is depicted in Fig. 4.24, where each colour represents the corresponding temperature.

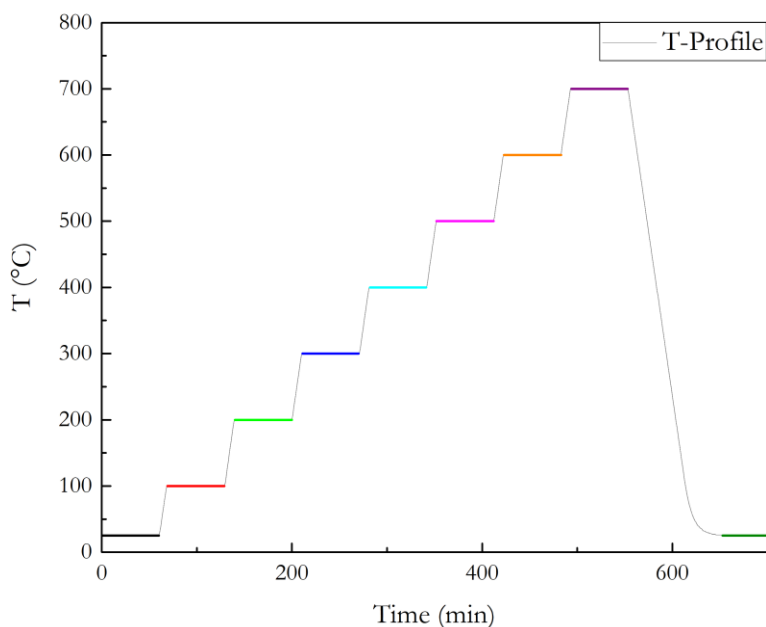


Figure 4.23: Temperature profile for non-ambient XRD measurements of SRO and LNCO, respectively on STO (100). The colour-coded plateaus indicate the respective measuring temperatures.

LNCO

To examine the stability of the LNCO coatings on STO, non-ambient XRD measurements were performed under the same conditions as reported in the previous section. (Ar atmosphere, 25-700 °C). For this reason, LNCO was deposited on an STO (100) ($10 \times 10 \text{ mm}^2$) single crystal and investigated under given conditions. The resulting graphs are illustrated in figure 4.24, whereby for the purpose of simplicity, only the diffraction patterns obtained at the starting and end point (25 °C) are depicted. The dotted lines indicate reflexes originating from LNCO. On the basis of the diffractograms, no qualitative change in the layer structure can be perceived, which allows the conclusion that LNCO retains its stability under given LFP deposition conditions.

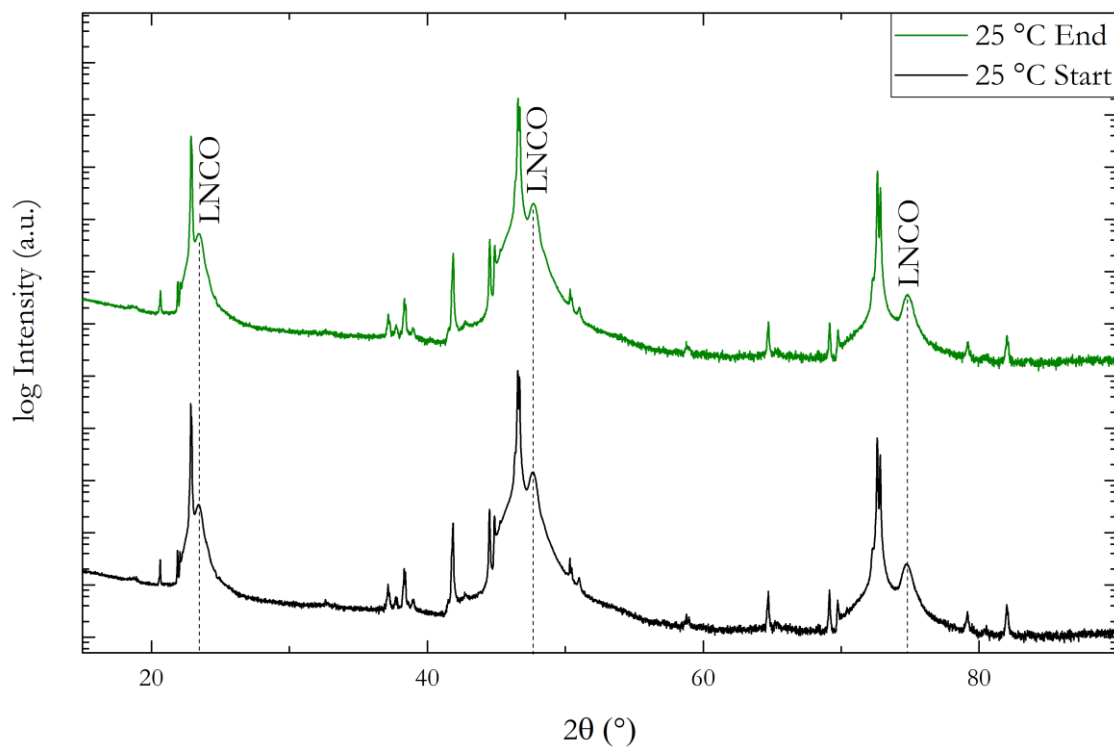
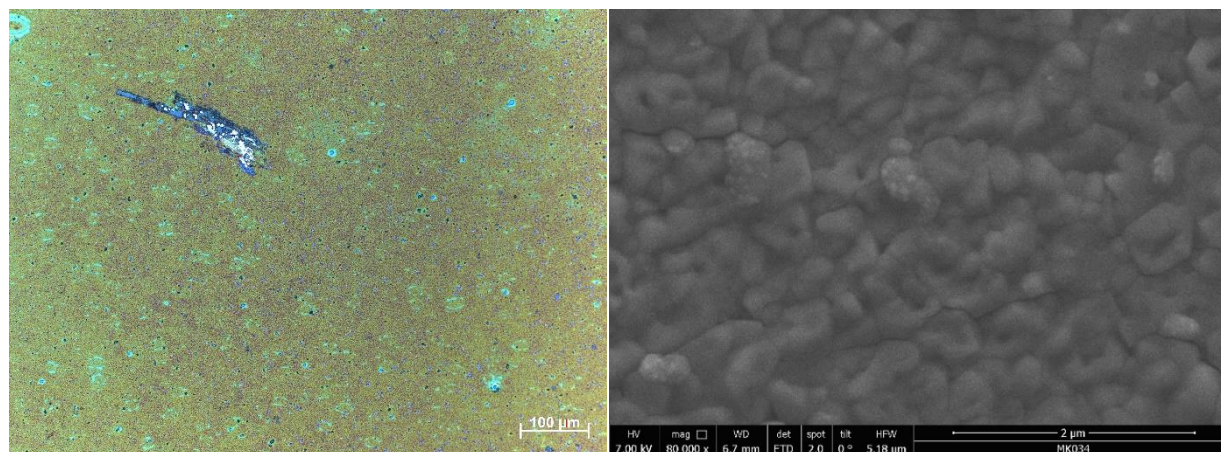


Figure 4.24: Non-ambient temperature XRD measurements of LNCO on STO (100) performed under argon atmosphere. Displayed are diffractograms of starting point (black) and end point (green) at 25 °C. The temperature profile is shown in figure 4.23.



(a) Optical light microscope

(b) SEM

Figure 4.25: Light microscope (a) and SEM (b) images of LFP deposited on STO (110)|LNCO at a deposition temperature of 550 °C for 77 min.

In order to prepare an electrically contactable LFP thin-film electrode, a deposition on STO (110)|LNCO ($5 \times 5 \text{ mm}^2$) was performed, with the results for the sample fabricated at nominally 550 °C for 77 min shown in figure 4.25 and 4.26. The optical microscope image in 4.25 (a) depicts the surface of the deposited LFP layer, with a scratch visible in the upper half of the frame. This is a result of the resistance measurement, which was carried out with a multimeter from "edge to edge". It showed that the in-plane resistance after LFP coating is $\sim 150 \text{ k}\Omega$, which represents a deterioration compared to the uncoated LNCO layer ($\sim 600 \Omega$). From the SEM image in figure 4.25 (b), the surface morphology can be studied and the typical LFP layer structure can be observed, although scattered impurities in the form of bright spots on grains occur. The origin of these phenomena is not understood.

Figure 4.26 shows the diffractogram of the thin-film, where the very dominant reflexes generated by the substrate and the platinum paste can be identified. Therefore, the sample was additionally measured in grazing incidence (GID) mode, as here a smaller angle of incidence of the X-ray beam is used and thus mainly scattering contributions of surface-near structures are detected. When examining the two diffraction patterns, reflexes of the LFP planes (200), (101) and (210) could be specified (~ 17.2 , ~ 20.8 and $\sim 22.8^\circ$) in addition to those from the substrate and platinum paste. As with previous samples, unassignable features are present.

A more detailed electrochemical characterisation of this sample can be found in section 4.2.

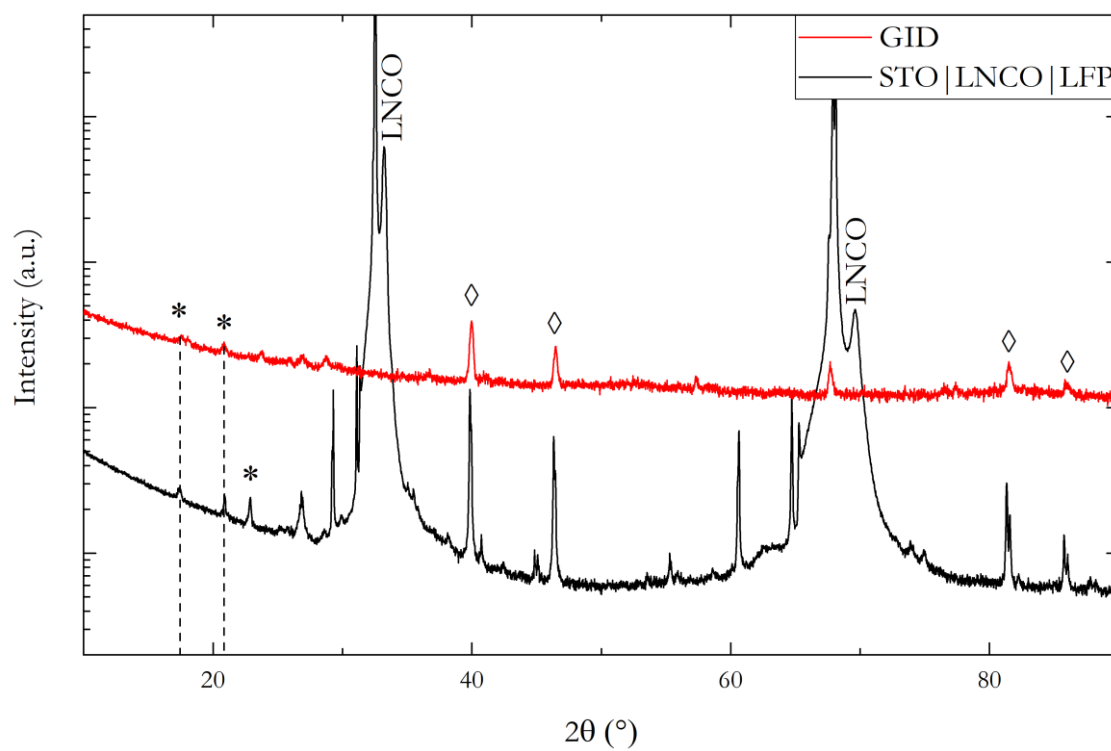
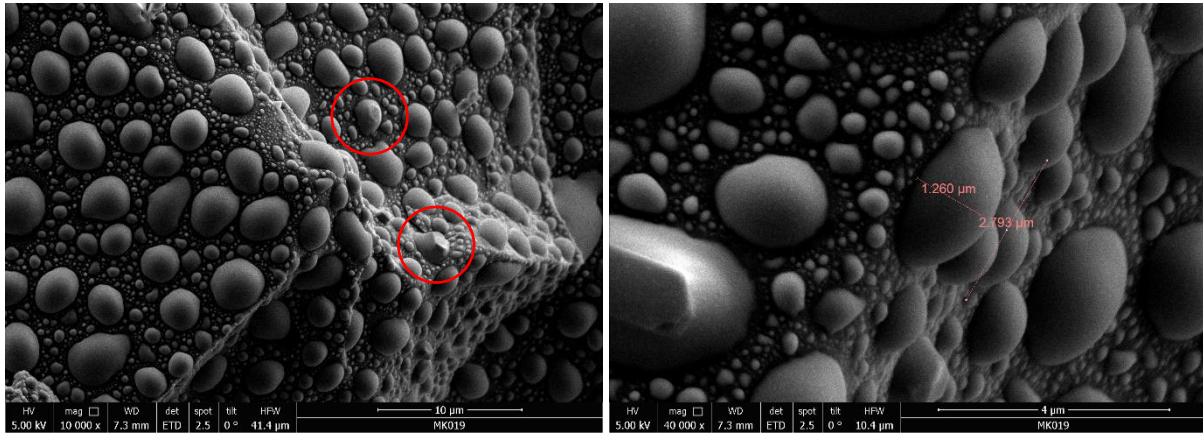


Figure 4.26: X-Ray diffractogram of LFP deposited on STO (110)|LNCO at 550 °C measured in Bragg-Brentano (black) and grazing incidence (GID, red) geometry, respectively. \diamond – Pt, * – LFP

4.1.5 Alternative Conductive Substrates

Glassy carbon



(a) Rim of the substrate

(b) Measured LFP droplet

Figure 4.27: SEM images of LFP deposited on glassy carbon for 120 min. (a) shows an image taken at the rim of the substrate and (b) a magnification with measured LFP droplet. Droplets with structural features are highlighted in red.

In order to study alternatives to the already mentioned electrically conductive substrates, glassy carbon was used as a candidate. While the properties (cf. section 4.2.5) are very interesting, the poor wettability of the surface by melts is a major drawback for the application in this thesis. Nevertheless, a deposition of LFP on glassy carbon ($10 \times 10 \text{ mm}^2$) was carried out at different temperatures. The poor adhesion properties become obvious when the surface is examined more closely using SEM, depicted in figure 4.27. Instead of a homogeneous LFP layer, drops of different sizes are found, distributed over the entire area. Regarding the droplets, two features stand out in particular. The first is size. Derived from the deposition time of 120 min, a layer thickness of $\sim 300 \text{ nm}$ was targeted. If we now look at the measured droplet in 4.27 (b), we see that the material agglomerates during deposition and the resulting structures have a multiple of the targeted thickness. These accumulations, however, appear to represent a foundation for structural growth, as highlighted in red in figure 4.27 (a). Since glassy carbon is an amorphous substance, the material generates a continuous diffractogram, which implies that no sharp reflexes attributable to the substrate occur. (Fig. 4.28) Nevertheless, at $\sim 22.7^\circ$ a feature can be identified which is not entirely superimposed and therefore can be assigned to LFP.

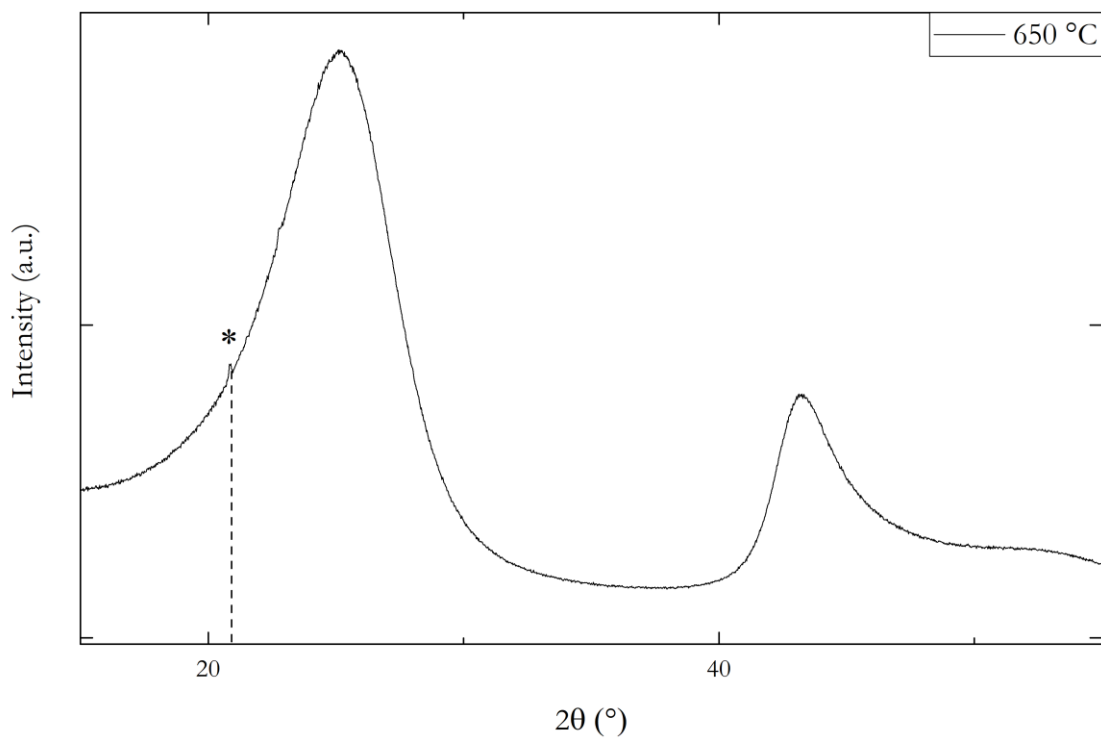


Figure 4.28: Diffractogram of LFP deposited on glassy carbon (10x10 mm²) at 650 °C for 120 min. * – LFP

Al₂O₃|Pt

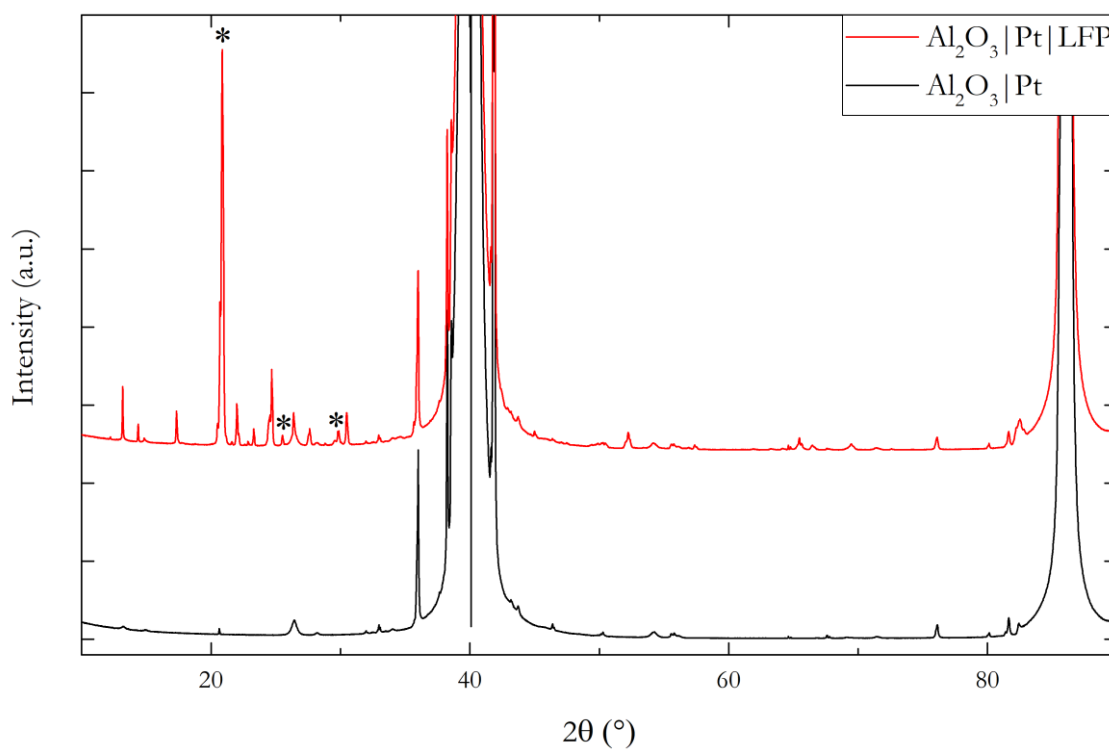


Figure 4.29: LFP deposited on Al₂O₃|Pt at 550 °C for 120 min. The black line indicates the diffractogram of the substrate (Al₂O₃|Pt), while the red line reflects the pattern after deposition of LFP. * – LFP

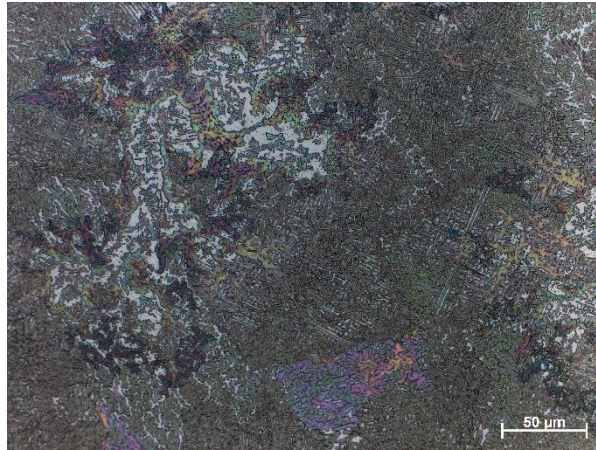


Figure 4.30: Image of LFP deposited on Al₂O₃/Pt at a deposition temperature of 550 °C for 120 min, taken via optical light microscope.

Hot deposited platinum as a foundation for the application of ceramic layers is usually a simple and functional method to achieve electrical conductivity. By depositing the platinum on Al₂O₃/Pt at 1000°C, rather than at room temperature, a defined surface should be ensured in order to subsequently achieve a smooth LFP layer.

LFP was deposited at different temperatures on Pt|Al₂O₃/Pt for 120 min, with exemplary results for a preparation at 550 °C being summarised in figures 4.29 and 4.30. Comparing the diffractograms of the bare substrate and the sample after treatment (Fig. 4.29 black and red, respectively) reveals reflexes originating from LFP, but no preferential orientation is observed. This can be explained by a more detailed examination of the layer under the light microscope (Fig. 4.29), where it is shown that even on this substrate, i.e. on platinum, the adhesion for LFP is very poor. This results in a mosaic-like structure, which makes it unsuitable to use this substrate for the purposes of this work.

4.1.6 Cross-Section Analysis

SEM

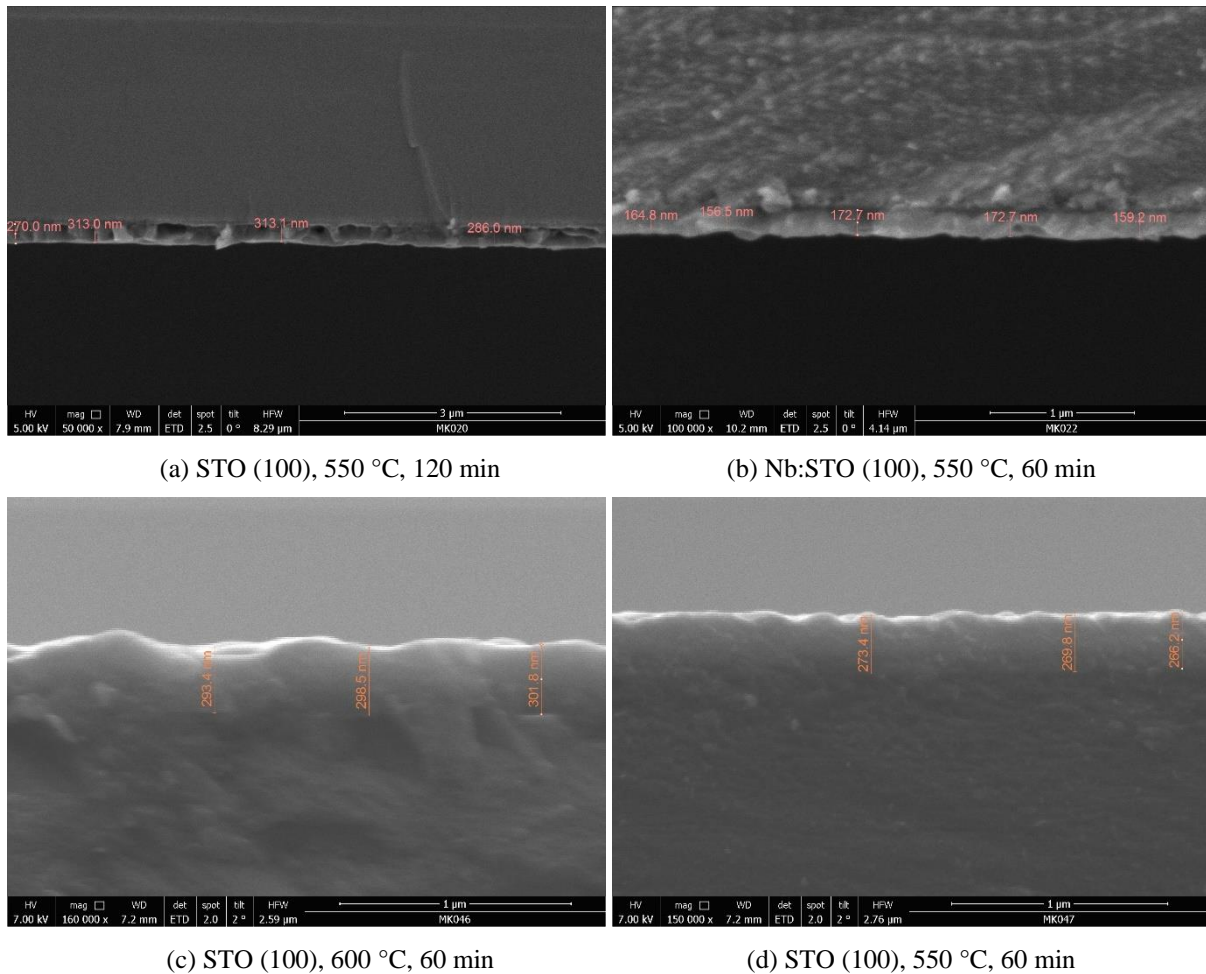


Figure 4.31: Images of LFP thin-film on STO (a, c, d) /Nb:STO (b) in cross-section, taken via SEM.

In order to be able to make a qualitative assessment of the layer properties and to determine an approximate deposition rate, selected samples were analysed in cross-section using SEM. At this point, it must be taken into account that the determination of the thickness by means of a SEM cross-section turned out to be not ideal for these thin-films, since the boundary region between substrate and LFP is affected by an interdiffusion layer, which is formed during deposition. For further details, see the section TEM below.

To examine the samples, they were now pre-sputtered with Au/Pd to ensure the conductivity of the surface. Shown in 4.31 are the representative images of the respective samples with indicated layer thicknesses, which were determined by means of graphical evaluation.

The samples presented in 4.31 (a) and (b) deposited at 550 °C on STO (100) and Nb:STO (100), respectively, were prepared on the heater-type A at the beginning of this project. The top views of these samples are shown in figures 4.6 (a) and 4.18 (b). Using the measured layer thicknesses and the specified deposition times, an approximate deposition rate of 2.6 nm/min can be derived. This value was used to establish a rough relation between duration and layer thickness.

The samples from 4.31 (c) and (d) were prepared at 600 and 550 °C on STO (100) using the heater-type B and C, respectively. The top views of the layers can be found in figure 4.10 (b) and 4.12 (c). If the deposition rates are determined with the help of these thin-films, the values are 4.9 and 4.5 nm/min, respectively.

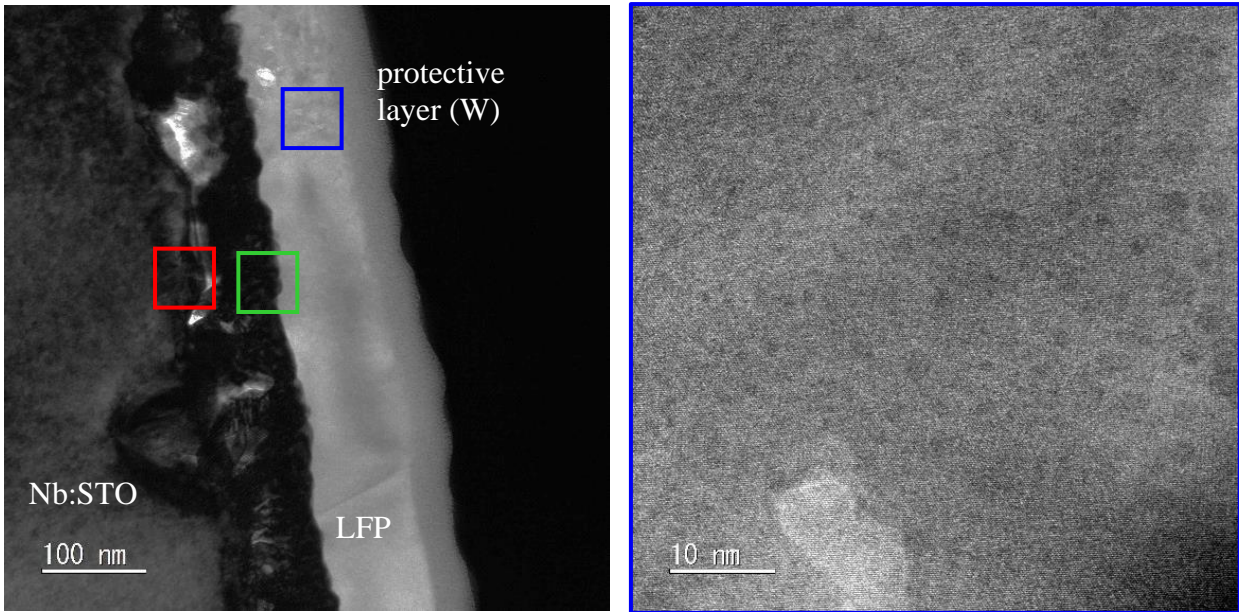
On closer examination of the samples depicted in 4.31 (c) and (d), it is noticeable that the roughness of the layer is linked with the degree of crystallisation, as can be seen from the diffractogram of the sample (4.9 red and 4.11 black line). Accordingly, the sample with higher crystallinity deposited at 600 °C exhibits a higher roughness than that at 550 °C, where the critical crystallisation temperature has not yet been reached. These observations are supported by investigations using the profilometer.

TEM

In order to be able to examine the structural properties of the layer on an atomic level and subsequently make statements about the crystallographic orientation, TEM (transmission electron microscopy) investigations of a sample were carried out. The sample used was LFP deposited on Nb:STO (100) at nominally 600 °C for 60 min, whereby clear LFP reflexes could be assigned in the corresponding diffractogram.

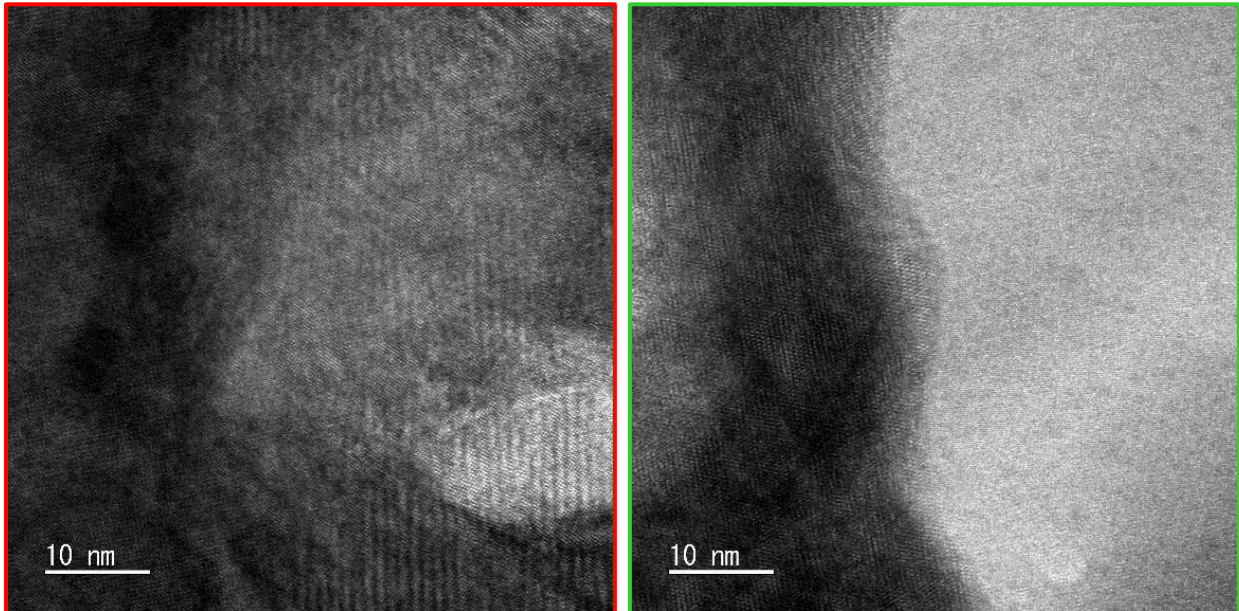
For analysing the cross-section in transmission, a focused ion beam (FIB) was used to cut out a lamella from the centre of the sample, which was subsequently thinned out by ion milling. Figure 4.32 (a) shows the TEM image of the cross-section of Nb:STO|LFP, while in 4.32 (c-d) the enlargements of individual areas are highlighted by colour. Before the crystallographic properties of the thin-film are discussed, the general layer structure must be analysed briefly, as this structure was not entirely to be expected.

Based on the differences in brightness in 4.32 (a), the individual layers can be distinguished from each other, whereby LFP appears brighter due to the Z-contrast ($\text{intensity} \propto 1/Z^2$), as it has the lower mean atomic number Z than Nb:STO.



(a) TEM image of Nb:STO (100)|LFP

(b) LFP layer



(c) Intermediate area of Nb:STO (100) and newly formed phase

(d) Interlayer between LFP and newly formed phase

Figure 4.32: TEM images of Nb:STO|LFP cross-section (a) and colour-coded enlargements of selected areas (c-d).

However, a new phase has formed between the two layers of LFP and Nb:STO. This appearance suggests that interdiffusion between the two materials occurs during the deposition of LFP at high temperatures, which subsequently leads to a significant impact on the electrochemical properties of the thin film.

Looking at the layers and interfaces in detail, 4.32 (b) displays an area of the LFP layer in atomic resolution. At the lower edge of the image, an incorporation of a foreign phase with a lower mean atomic number Z can be seen, which indicates that a phase-pure production of the layer is not entirely achieved. The boundary phase of Nb:STO and the interdiffusion layer (Fig. 4.32 c) shows ordered rows of atoms, illustrated by dots, in addition to foreign phase inclusions. Examination of the diffuse interface between LFP and the interlayer (Fig. 4.32 d) reveals the transition between the ordered atomic rows of the Nb:STO single crystal and the increasingly polycrystalline structure of the LFP thin film. As already mentioned, an explanation for the poor electrochemical properties of this system can be derived on the basis of this phenomenon. One way to counteract this interdiffusion is to apply a protective layer between the substrate and the thin film, where coatings such as SRO or LNCO may be suitable.

STEM-EDX

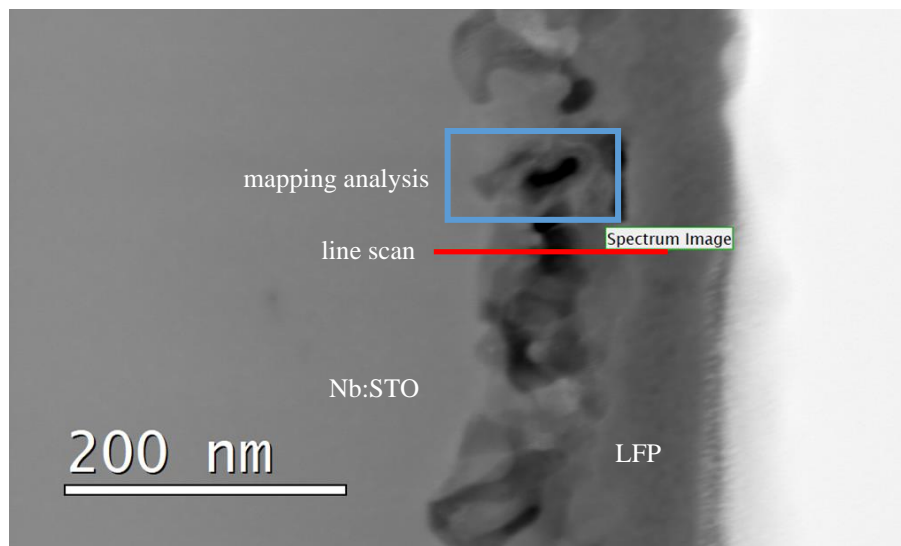


Figure 4.33: HAADF STEM image of Nb:STO|LFP with highlighting of the selected areas for EDX elemental mapping analysis (blue rectangle) and line scan (red line).

The boundary region between Nb:STO and LFP was subjected to STEM-EDX analysis (scanning transmission electron microscopy - energy dispersive x-ray analysis) in order to investigate the distribution of the elements in this area. Figure 4.33 shows a high-angle annular dark-field (HAADF) TEM image of the sample cross-section where the interdiffusion layer between Nb:STO and LFP is clearly identified. Dark areas in this region can be interpreted as cavities or holes, suggesting a porous structure of the layer. The area for 2D chemical mapping analysis is outlined in green, while the red line represents the line scan. The EDX mapping images and line scans for the relevant elements are depicted in figure 4.34 and 4.35, respectively.

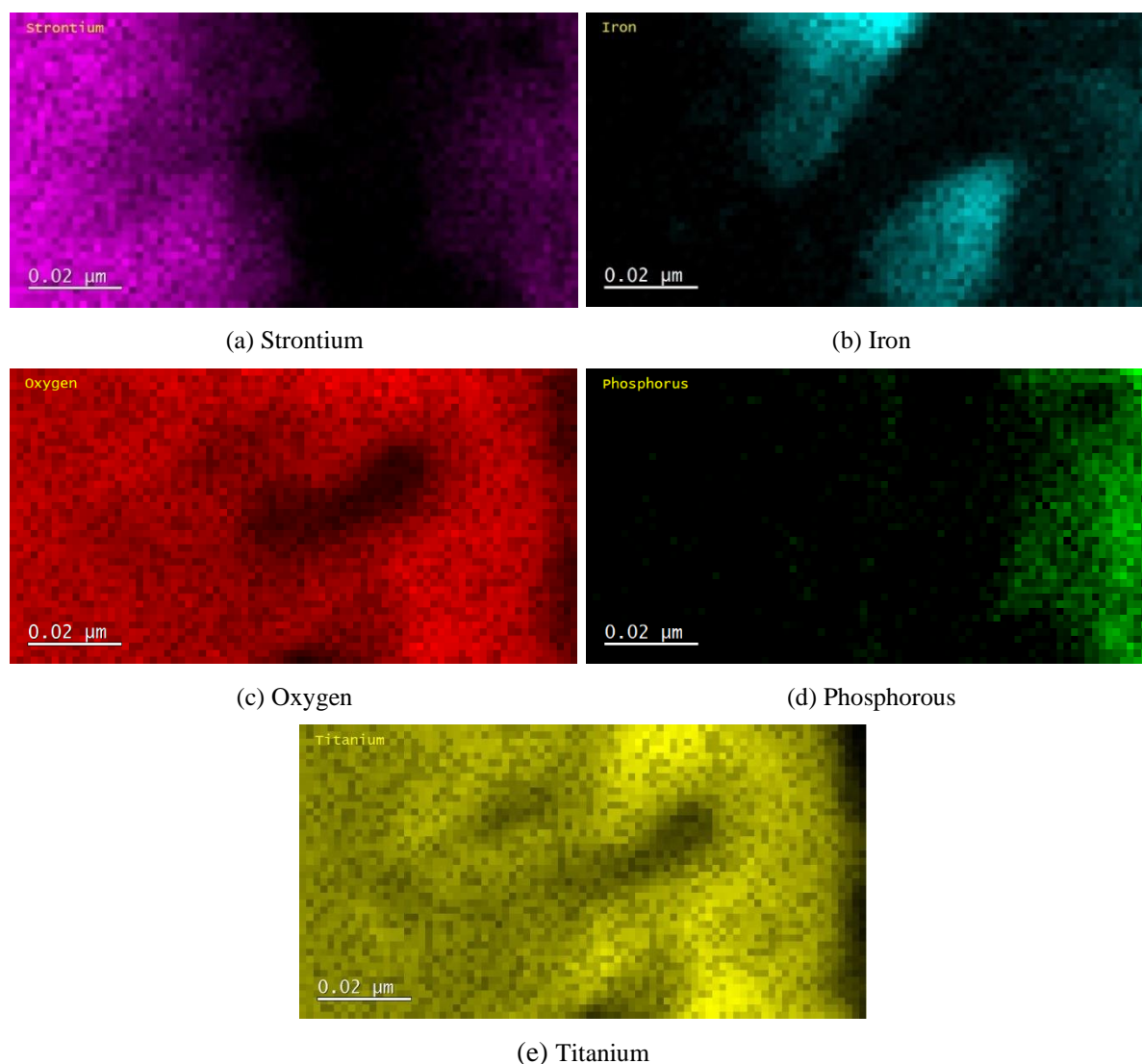


Figure 4.34: EDX maps for relevant elements, representing elemental distribution in the selected area. (cf. 4.33)

The interdiffusion of LiFePO_4 and $\text{Nb}:\text{SrTiO}_3$ can be demonstrated using EDX maps of strontium, iron, oxygen, phosphorus and titanium, where the spatial distribution of the elements is indicated by colour intensity. In particular, the elements strontium and iron (Fig 4.34 a and b) can be used to visualise the result of the diffusion process, as enrichments of the elements occur outside of the corresponding layer. Dark kidney-shaped areas, clearly visible in oxygen (c) and titanium (e), presumably represent cavities or holes, as already mentioned. Accordingly, the intensity measured in these areas is lower. In the case of phosphorus, it can be found that hardly any diffusion takes place into the intermediate layer and that the signal is primarily obtained in the area of the LFP layer.

Another method to investigate the elemental distribution in a selected area of the sample is an EDX line scan. The results are shown in 4.35 and 4.36. The width of the electron beam was $\sim 1\text{nm}$.

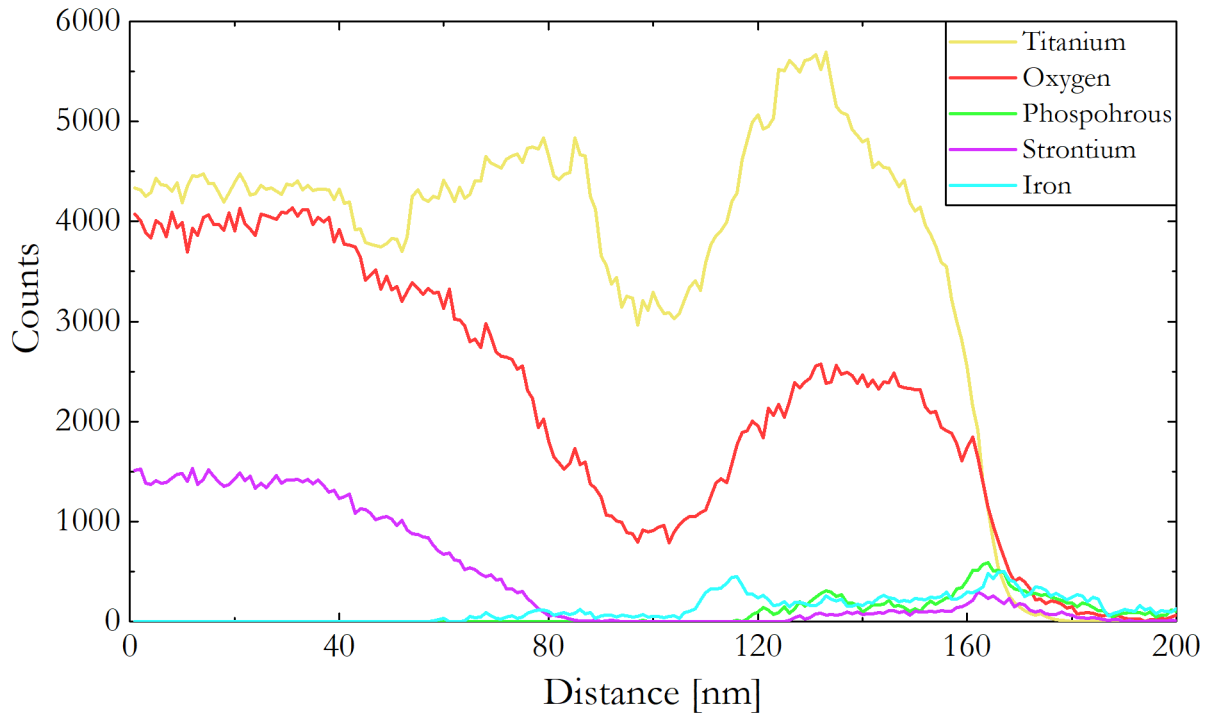


Figure 4.35: EDX line scans of relevant elements in the selected domain. (cf. 4.33)

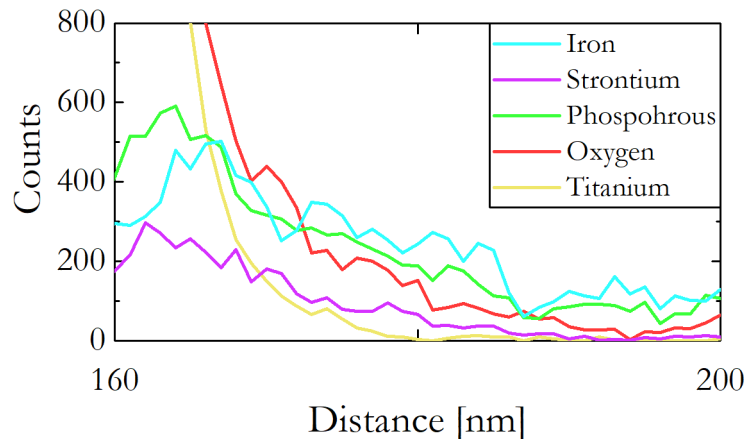


Figure 4.36: Magnification of the EDX line scans from figure 4.35 for the range 160-200 nm.

The enrichment of the elements outside their origin can also be observed from the line scans, whereby iron in particular can be found far outside the LFP layer. The drop at ~ 100 nm is presumably due to a hole, as can also be seen in figure 4.33. Furthermore, the low intensity from ~ 160 nm onwards may be related to beam damage, whereas upon enlarged observation of this range, the elements Fe, P and O, which are attributable to LFP, can be detected. This indicates that in this area the transition to the pure LFP layer is taking place.

4.2 Conclusion of the Thin-Film Preparation

Since the production of the LiFePO_4 thin films and the optimisation of the deposition parameters represent a central issue within the scope of this thesis, it is appropriate at this point to classify the results achieved so far.

LFP was deposited by RF magnetron sputtering on various substrates at different temperatures. It has been demonstrated that of the substrates tested, STO (100) and Nb:STO (100) are the most favourable for the fabrication of crystallographically oriented and morphologically suitable LFP thin films. For the assessment of these characteristics, XRD and SEM were primarily used, where a preferred orientation of the layer in the (410) lattice plane could be specified. Depending on the configuration of the heating element used, a deposition temperature of 550 °C and 600 °C, respectively, proved to be optimal, whereby it became apparent that the actual substrate temperature and the temperature distribution in particular play an important role in promoting the crystallisation of the layer in the desired manner. Furthermore, the oxygen content in the deposition chamber is a factor that must be monitored in order to prevent degradation of the layer at high temperatures.

By characterising an Nb:STO|LFP system using TEM, it was established that interdiffusion occurs between LFP and STO during deposition at high temperatures. This phenomenon might be responsible for the high surface roughness of the layers. Furthermore, this interlayer is a contributing factor to the poor electrochemical properties of the electrode when studied in cross-plane geometry. In-plane impedance measurements, on the other hand, should not be affected by this interdiffusion layer, as here the direction of measurement is parallel to the surface.

Following on from these results, the electrochemical investigations of the prepared electrodes are discussed in the next section.

4.3 Electrochemical Characterisation

As already explained in detail in section 3.4, there were two different approaches regarding the experimental set-up for the electrochemical investigation of the fabricated samples. On the one hand, the liquid cell, where charge-discharge experiments, cyclic voltammetry and cross-plane impedance measurements were conducted in the environment of an aqueous electrolyte. And on the other hand, the microcontact configuration, where in-plane impedance measurements were performed to characterise the thin-film properties.

4.3.1 Liquid Cell

Before going into a detailed discussion of the results, the electrochemical stability of the electrolyte needs to be addressed. Figure 4.37 shows the cyclic voltammogram of 1M aqueous LiNO_3 at a scan rate of 0.1 mV/s, with a platinum wire as WE and CE, respectively. As can be clearly seen, the stability window of the electrolyte lies between 3.4 and 4.0 V vs. Li/Li^+ . The potential of LFP vs. Li/Li^+ , however, is 3.45 V, as depicted in the diagram. Therefore, the electrochemical activity region of LFP is at the edge of the stability range of the $\text{LiNO}_3 (\text{H}_2\text{O})$ electrolyte, which can lead to complications in measurements and in the interpretation of the results, especially for the reduction of $\text{FePO}_4 \rightarrow \text{LiFePO}_4$.

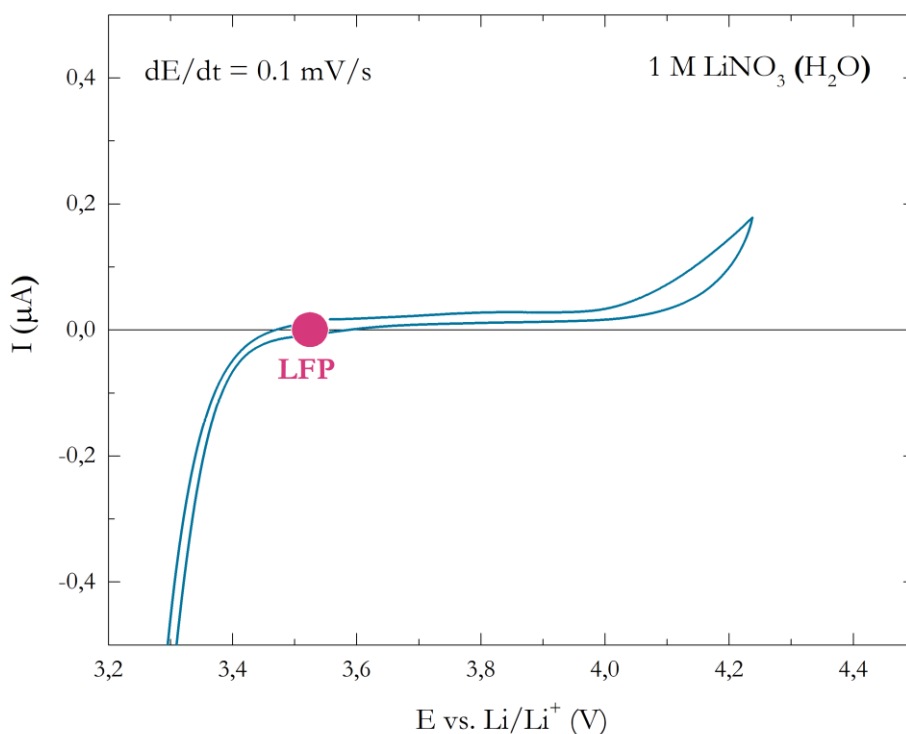


Figure 4.37: Electrochemical stability range of LiNO_3 (1M in H_2O). Potential of LFP vs. Li/Li^+ is highlighted.

Charge-Discharge Experiments

In order to alter the lithium stoichiometry in the electrode material, an attempt was made to acquire charge-discharge curves. However, for the produced samples, it was not feasible to record charge/discharge cycles in a sufficient quality, due to the poor transport kinetics of the thin-films. Figure 4.38 provides a representative diagram for the respective steps, which can be applied to all measured thin-film electrodes. The sample, which is presented here as an example, is LFP deposited on STO(100)|SRO, with the back and edge treated with Ti/Pt and Pt paste, respectively. The charge/discharge current (I_{CD}) was 500 nA and the selected potential limits were 3.34 and 4.14 vs. Li/Li⁺, respectively.

It can be observed that the potential rapidly approaches the limit value during both charge and discharge step, with a sharp increase/decrease at first, which gradually flattens out. This behaviour towards the end of the sequences can be explained by the instability of the electrolyte discussed in the previous section. Outside the stability window, redox processes begin to occur in the electrolyte, which can be misinterpreted as an onset of a plateau, especially in the discharge step. However, if the potential of LFP is added to the diagram (dotted line), it then becomes apparent that this behaviour refers to the beginning decomposition of the aqueous electrolyte and not to a change in lithium stoichiometry of LFP.

At this point it has to be mentioned that when measuring the open circuit voltage (OCV) at the beginning of each experiment, a potential of ~3.5 V vs. Li/Li⁺ was registered, which corresponds to the resting potential of LFP. Therefore, it can be concluded that a reasonable Li chemical potential has been established during preparation and characterisation is possible, but the behaviour observed is a result of the poor kinetics of the layer.

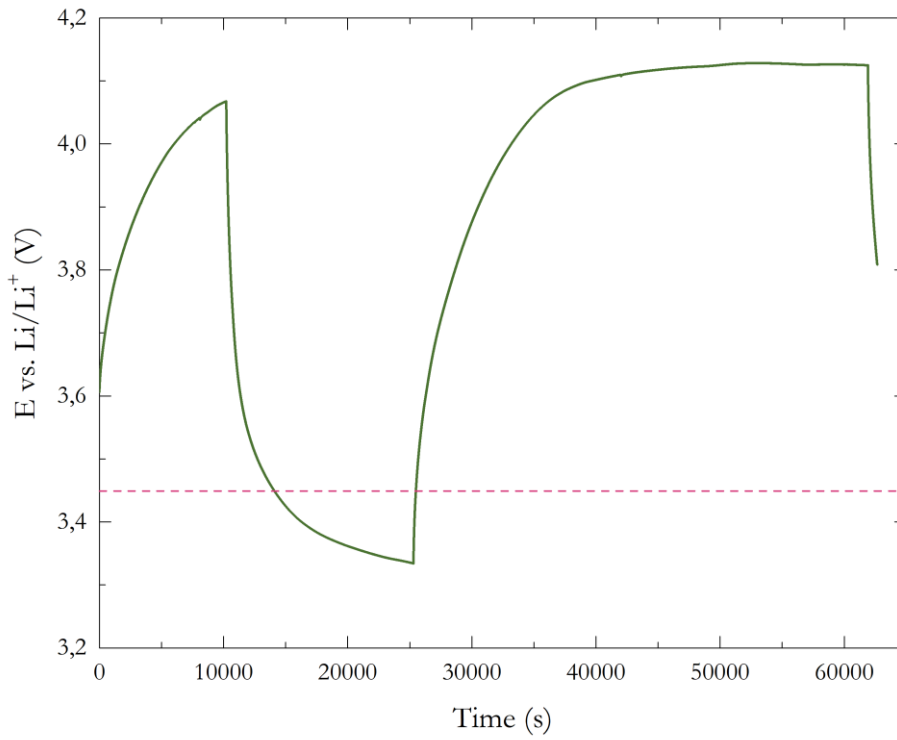


Figure 4.38: Charging or discharging step of an exemplary LFP sample on $\text{STO}(100)|\text{SRO}$ with $I_{\text{CD}} = 500$ nA.

Cyclic Voltammetry

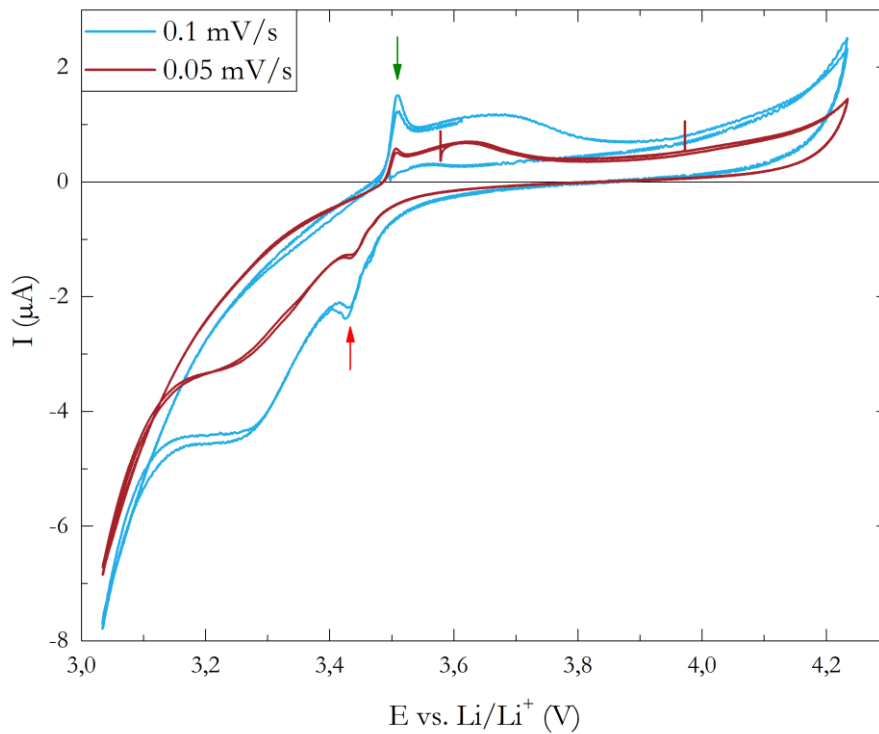


Figure 4.39: Cyclic voltammogram of LFP on $\text{STO}(110)|\text{LNCO}$ with a scan-rate of 0.05 and 0.01 mV/s respectively. Oxidative (green) and reductive (red) peaks corresponding to LFP are highlighted.

Cyclic voltammetry measurements were used to investigate whether redox processes that can be assigned to the LFP are observed. Due to the aforementioned difficulties, the measurement of the cyclic voltammograms was also affected. However, for one thin-film electrode redox peaks could be identified, which could be attributed to LFP. Figure 4.39 shows the corresponding graphs. For the investigated sample, LFP had been deposited at 550 °C on STO(110)|LNCO, with the back and edge of the substrate treated with Ti/Pt and Pt paste, respectively. For a detailed structural analysis of the sample, please refer to section 4.1.4 LNCO. The cyclic voltammograms were recorded at a scan rate of 0.1 and 0.05 mV/s for two cycles each.

As illustrated in figure 4.39, for the first time, an electrochemically reversible behaviour of a LFP thin-film electrode could be observed. The anodic peak, which indicates oxidation of LFP at ~3.51 V, is highlighted with a green arrow, while the cathodic peak, representing reduction at ~3.43 V, is labelled with red. The small overpotential of the redox peaks also indicates a high layer quality. Additional features in the cathodic region from ~3.3 V can be attributed to the instability of the electrolyte, while that anodic peak at about 3.7 V is of unknown origin.

The novel observation of redox activity associated with LFP, contrary to the results obtained so far, can be explained by the assumption that LNCO serves not only as a contact promoter but in this case also as a protective layer between STO and LFP, which might counteract interdiffusion and thus facilitate electron transport across this boundary.

Cross-Plane Impedance Spectroscopy

With the given set-up, no reasonably interpretable cross-plane impedance measurements could be performed, as exemplified by figure 4.40. Therefore, in-plane impedance measurements were subsequently brought into consideration. (see 4.3.2) Three main issues are considered to be responsible for the fact that electrochemical characterisation is not properly feasible with the existing setup. First of all, it is the poor general transport properties of LFP [25, 26] that lead to increased resistance during measurement. Secondly, the electrical contacting of the system consisting of substrate and LFP layer is a significant issue. Here, especially the contact resistance between platinum and Nb:STO is noteworthy. Thirdly, investigations using TEM have revealed that the interlayer that forms between STO and LFP during deposition can be a serious obstacle to investigations in cross-plane geometry.

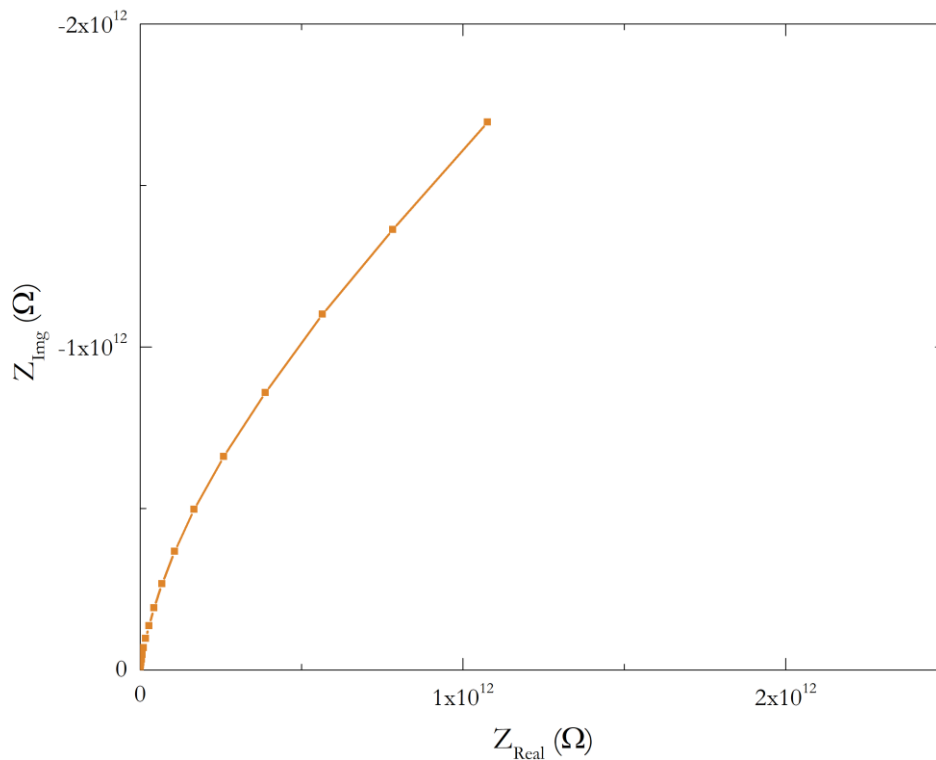
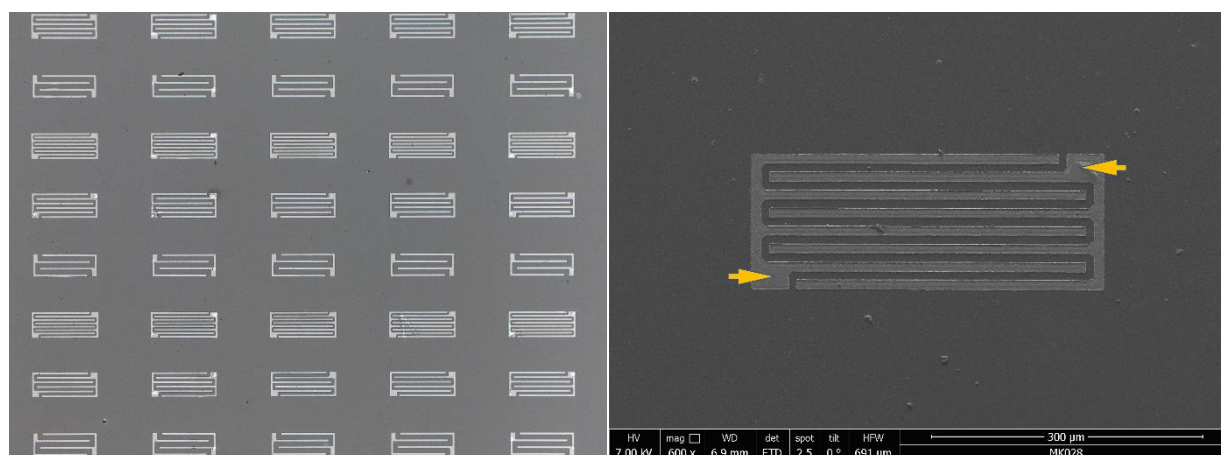


Figure 4.40: Impedance spectrum of an exemplary LFP sample on STO(110)|LNCO

4.3.2 Microcontact Setup

In-Plane Impedance Spectroscopy



(a) Section of the sample surface.

(b) Microelectrode with a finger distance of 10 µm.

Figure 4.41: (a) Arrangement of the platinum finger electrodes on the sample surface. (b) SEM image of an electrode with a finger spacing of 10 µm, with contact points marked in orange.

As cross-plane impedance measurements of the thin film electrodes could not be performed due to the issues discussed in the previous section, a modification of the measurement geometry to in-plane was made.

The sample subjected to the investigation was LFP deposited at 550 °C for 20 min on STO (100). Based on the deposition time and the derived deposition rate (cf. 4.1.6), this results in a layer thickness of approximately 50 nm. For a detailed structural analysis of the sample, please refer to section 4.1.2. The microelectrodes placed on the surface by photolithography exhibited finger distances of 10, 15 and 28 µm, systematically distributed over the entire surface, as illustrated in figure 4.41 (a). Figure 4.41 (b) shows a SEM image of a microelectrode with an inter-finger-distance of 10 µm, where the contacting sites of the gold needles are highlighted with arrows.

The impedance measurements were carried out with electrodes distributed across the entire surface at set heater temperatures from 22 °C (rt) to 450 °C. This not only provided information about the impedances of the layer, but also allowed its homogeneity to be investigated at the same time.

In order to be able to make a statement about the measured total conductivities as well as the electronic and ionic contributions, the obtained impedance spectra were evaluated using the programme ZView (Scribner Associates, Vers. 3.5h).

Beforehand the general appearance of the spectra must be discussed in order to elucidate the difficulties that arise when measuring the impedance of systems with a very high overall resistance. Figure 4.42 visualises the spread of impedance when analysing different electrodes with constant finger spacing ($15\ \mu\text{m}$) at room temperature.

The total resistance at room temperature is in a very high range of $10^{11}\ \Omega$, which leads to difficulties especially when measuring the low-frequency region, as illustrated in figure 4.41.

$$\tau \propto \frac{L^2}{D} \quad (4.1)$$

Individual processes involved in the charge transport in this electrode have very high time constants τ at room temperature (formula 4.1, L is diffusion length, D is diffusion coefficient), which leads to the fact that at low frequencies, i.e. long observation periods, processes with a time constant $>100\text{s}$ ($10^{-2}\ \text{mHz}$) can no longer be registered at all or not in a precise manner. This results in a missing separation of individual processes at room temperature, which is why only a single semicircle is recognisable. The time constants of the processes can be decreased by either reducing L (given by gap between finger electrodes) or by increasing the temperature, which leads to an acceleration of the processes.

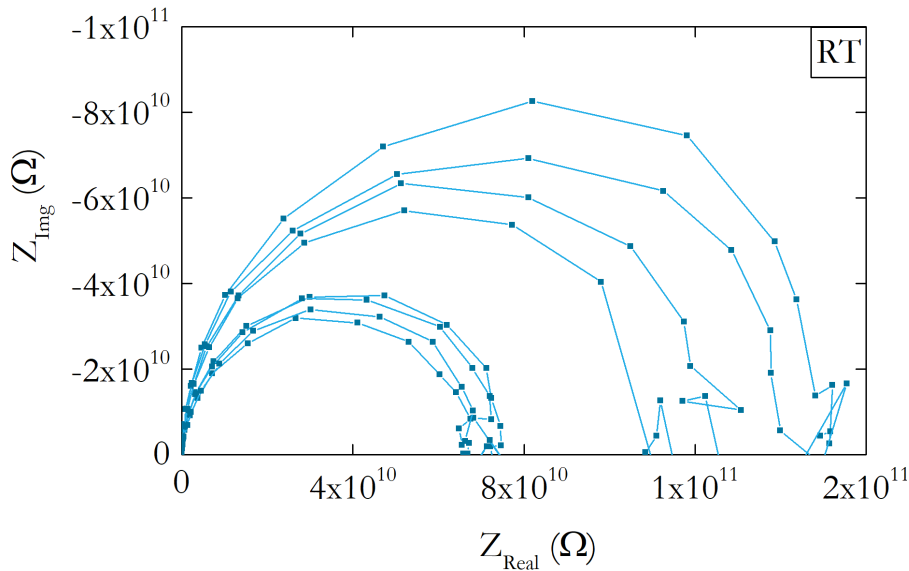


Figure 4.42: Scatter of the impedance of a microelectrode with a finger spacing of $15\ \mu\text{m}$ measured at room temperature

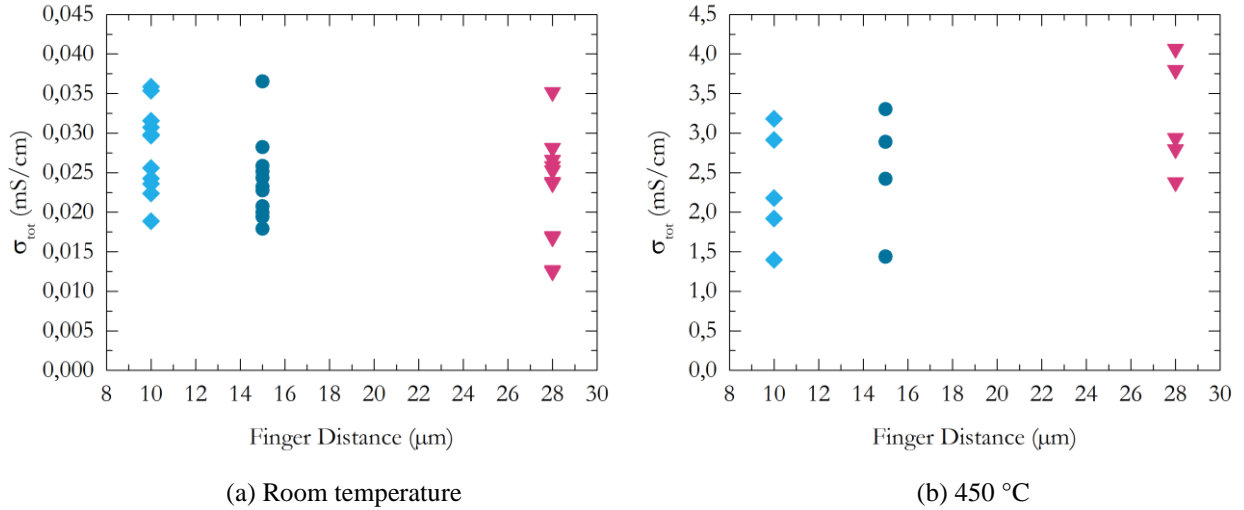


Figure 4.43: Spread of the determined total normalised conductivity with respect to the type of microelectrode, displayed for room temperature (a) and 450 °C (b)

The distorted form of the spectra at low frequencies is due to measurement artefacts, as the system reaches its measurement limits at such high resistances and is therefore susceptible to interference, which is reflected as shown.

In order to present the variance visually, the total conductivities σ_{tot} of the three types of electrodes at room temperature and 450 °C are depicted in figure 4.43. The resistance values (R) were determined by evaluating the dominant semicircle manually with ZView (feature 'Fit Circle'). This is equivalent to a simulation using an R||C element. In order to calculate the area-specific conductivities (S/cm), the values were normalised according to formula 4.2. Here d is the finger spacing and A the cross-section, calculated from the layer thickness and meander length. The latter is explained in figure 4.44.

$$R = \frac{1}{\sigma} \frac{d}{A} \quad (4.2)$$

Figure 4.43 demonstrates that the calculated total conductivity differs only slightly within one electrode type distributed over the sample surface, whereby no significant difference in the variance at room temperature (a) and 450 °C (b) can be identified here.



Figure 4.44: Microelectrode with drawn-in meander length (dotted line).

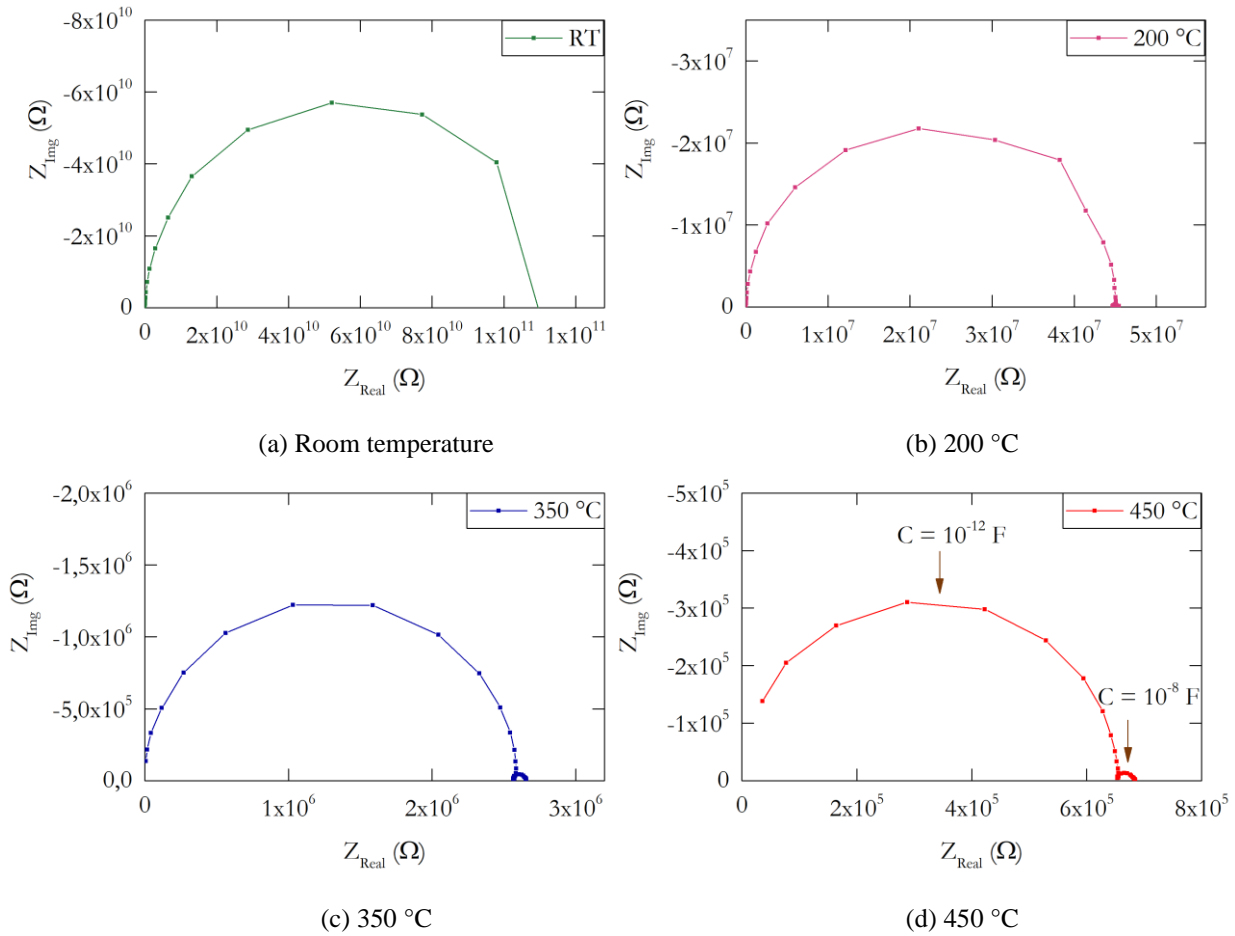
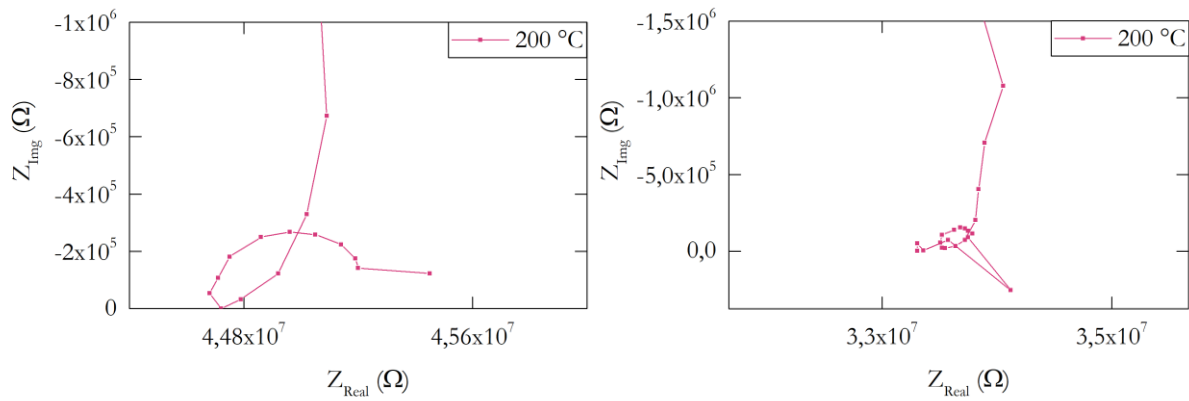


Figure 4.45: Impedance spectra of the same microelectrode with a finger spacing of 15 μm at room temperature (a), 200 °C (b), 350 °C (c) and 450 °C (d).

In order to investigate the temperature dependence of the transport properties and to extract electronic and ionic contributions, the impedance spectra measured at temperatures from room temperature to 450 °C were evaluated. Representative spectra of one electrode with medium (15 μm) finger distance, depicted in figure 4.45 at different temperatures provide a visualisation of the sample's behaviour. At room temperature, the familiar shape with a very high total resistance could be observed. When increasing the temperature to 200 °C (4.44 b), apart from a significant reduction of the resistance, an additional feature at low frequencies could be identified for the first time, which is magnified in figure 4.46 (a). The capacitances determined were 10^{-12} F for the first and 10^{-8} F for the low frequency semicircle, respectively, as depicted representatively in 4.45 (d). If the temperature was raised further, the ratio of the two semicircles changed increasingly in favour of the smaller one at low frequencies, while the total resistance decreased to $< 10^6 \Omega$ at 450 °C, compared to $\sim 10^{11} \Omega$ at rt. This characteristic allowed the reliable evaluation of the properties of the second semicircle at temperatures above 250 °C, since at 200 °C a representative fit could only be performed in individual cases (cf. Fig. 4.46).

Figure 4.46 shows two examples of the low-frequency feature of spectra recorded at 200 °C. An emerging development of a second semicircle is clearly visible, but only in certain cases it is pronounced enough to perform a reliable fit of the data. The loop like behaviour is possibly an artefact due to the in-plane measurement mode. [59, 60] In order to obtain electronic and ionic contributions in addition to the total conductivity, the relationship between the resistance and the conductivity shown in figure 4.47, derived from Nenning et al. (2017) [55], was applied. Here the low frequency semicircle of a measurement at 450 °C is plotted. (Enlarged from 4.45 d).



(a) Enlargement of 4.42 (b).

(b) Low frequency feature at 200 °C.

Figure 4.46: Magnification of the feature at low frequencies in impedance spectra recorded at 200 °C

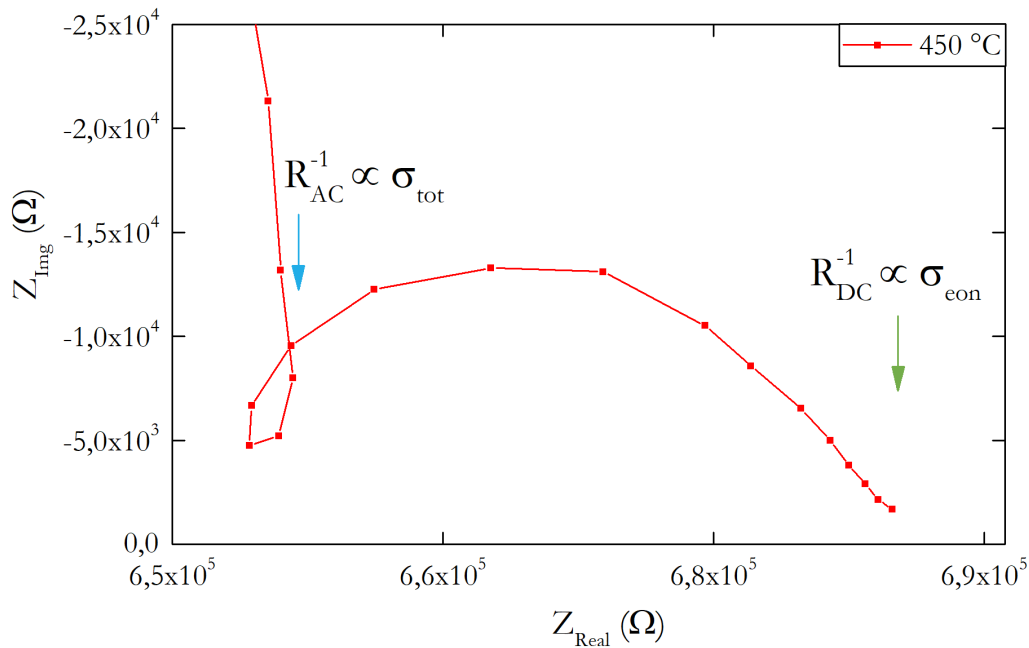


Figure 4.47: Representation of the low-frequency semicircle of an impedance measurement at 450 °C (enlarged from 4.41 d). The AC and DC resistance are labelled with blue and green arrows, respectively.

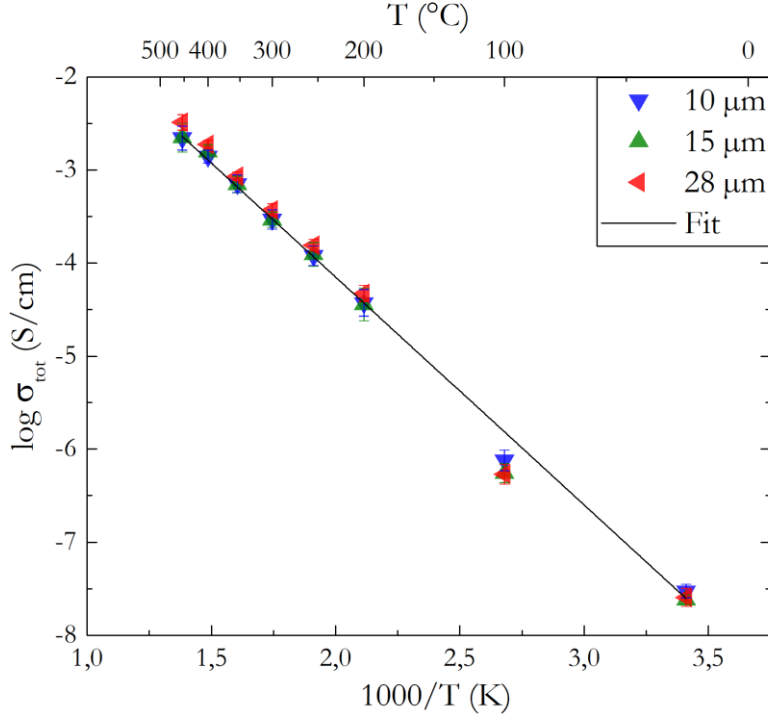


Figure 4.48: Arrhenius plot of total conductivity, with colour coding of data obtained by different types of electrodes. The error bars displayed represent the standard deviation.

The resistance measured at the transition from the first to the second semicircle, marked with a blue arrow, corresponds to the alternating current resistance R_{AC} . Both electrons and ions of the total system contribute to this resistance, which is why it can be regarded as the total resistance. According to formula 4.2, this results in the total conductivity σ_{tot} . For the DC case, i.e. at very low frequencies, it can be assumed that only electrons contribute to this resistance (R_{DC} , green arrow), which is why it can be regarded as a purely electronic resistance or conductivity. Using these values, the ionic conductivity can now be calculated with the help of formula 4.3.

$$\sigma_{tot} = \sigma_{eon} + \sigma_{ion} \quad (4.3)$$

Due to measurement artefacts and non-ideal data, the evaluation of the ionically induced semicircle in particular proved to be non-trivial. Nevertheless, the conductivities obtained were plotted in logarithmic form against the reciprocal temperature in an Arrhenius plot, with total conductivity in figure 4.48 and electronic and ionic conductivity in figure 4.49 (a) and (b), respectively. In order to be able to distinguish the data obtained by measuring different types of electrodes, they were colour-coded. In the Arrhenius plot of the total conductivity (Fig. 4.48), a linear relationship with respect to the temperature can be observed, whereby no significant difference can be found between the types of electrodes. Accordingly, it can be assumed that an approximate normalisation with formula 4.2 is acceptable.

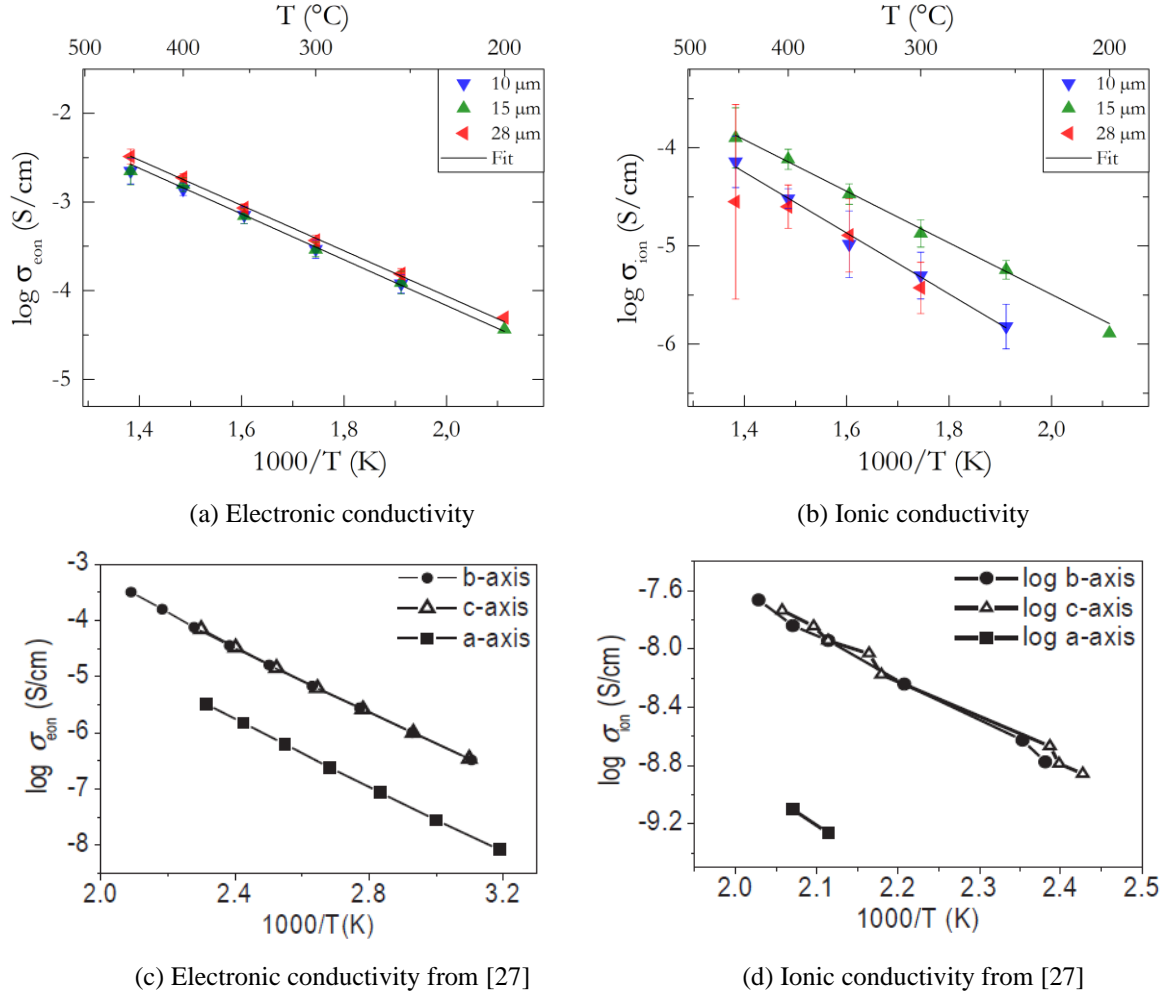


Figure 4.49: Arrhenius plots obtained from measured data for electronic (a) and ionic (b) conductivity, with colour coding for different types of electrodes. Plots (c) and (d) (electronic resp. ionic conductivity) allow visual comparison of the values obtained with the literature. (Maier et al. (2014) [27])

Figure 4.49 shows the Arrhenius plots for electronic (a) and ionic (b) conductivities. To the best of the authors knowledge, this is the very first data on the conductivity of LFP thin-films.

Figure 4.49 also displays plots from Maier et al. (2014) [27] (c and d) measured on LFP single crystals juxtaposed for simplified interpretation of the data. For a detailed discussion, see section 1.2. From this comparison, the following findings can be derived. As expected from the literature and already graphically evident from figures 4.45 and 4.47, the electronic conductivity is significantly higher than the ionic conductivity, with a difference of 1 to 2 orders of magnitude. Furthermore, it can be observed that electronic contributions in the material account for the largest share of the total conductivity.

Apart from the qualitative agreement, also a quantitative congruence of the measured data with those from the literature can be found for the electronic conductivity. When extrapolating the figures into a relevant temperature range, comparable results can be observed.

Determining the experimental values at $\frac{1000}{T} = 2.1$ (corresponding to 200 °C), one obtains $\sim 4 \times 10^{-5}$ S/cm for the thin-film conductivity. For the single crystals, values of $\sim 3 \times 10^{-4}$ S/cm (b-c axis) and $\sim 1 \times 10^{-5}$ S/cm (a axis) can be estimated.

However, a significant difference between the thin film data obtained and the literature data can be found for the ionic conductivity. Here, thin-film values at $\frac{1000}{T} = 2.1$ amount to $\sim 1 \times 10^{-6}$ S/cm (15 μm finger spacing) and $\sim 3 \times 10^{-7}$ S/cm (10 and 28 μm , extrapolated), respectively. These are considerably higher than the conductivities determined for single crystals, which are $\sim 1 \times 10^{-8}$ S/cm (b-c axis) and $\sim 6.3 \times 10^{-10}$ S/cm (a axis). One possible explanation for the deviation of the ionic conductivities is as follows.

As already mentioned, in the publication consulted, single crystals were used for the investigations. These presumably react more sensitively to $\text{Li}_{\text{Fe}}\text{-Fe}_{\text{Li}}$ antisite defects, which results in the blocking of Li^+ -channels throughout the crystal, which has a negative effect on the transport properties.

The deviation in figure 4.49 (a) and (b) with respect to the type of microelectrode can be attributed to the varying quality of the separation of the semicircles in the evaluated impedance spectra.

Using the Arrhenius equation (formula 4.4 and 4.5), the activation energies can be calculated, with σ_0 being the limiting conductivity, k_B the Boltzmann constant, T the temperature and E_A the activation energy.

$$\sigma = \sigma_0 e^{\frac{-E_A}{k_B T}} \quad (4.4)$$

$$\ln(\sigma) = \ln(\sigma_0) - \frac{E_A}{k_B} \frac{1}{T} \quad (4.5)$$

For the activation energy, a value of 0.49 eV, calculated on the basis of the total conductivity, is obtained. For electrons, the determined activation energies are 0.49 eV (large finger distance) and 0.51 eV (small and medium finger distance), whereas for ions we found 0.62 eV (medium finger distance) and 0.52 eV (small and large finger distance). For comparison, the values from the literature are for 0.6 eV electronic and 0.62 eV (bc-axis) for ionic transport, i.e. again reasonable agreement is found. [27]

5 Conclusion

In the course of this thesis, the preparation of LiFePO_4 thin-films by means of RF magnetron sputtering was performed, whereby the focus of attention was on the optimisation of this deposition process. Depending to the requirements, different substrates were applied, whereas a further electrochemical characterisation was targeted by the choice of an electrically conductive material. For this purpose, two different experimental set-ups were used, with the measurements being carried out either in an aqueous or inert environment, referred to as cross-plane and in-plane measurement geometry.

Within this project, LFP thin-films were successfully fabricated in a crystallographically preferred orientation in the (410) lattice plane on substrates such as STO (100) or Nb:STO (100), with structural characteristics monitored by methods such as XRD and SEM. New insights regarding the temperature sensitivity of the material during layer deposition could be gained in the course of this process. These results suggest that not only the actual deposition temperature, which was eventually found to be within an optimal window at around 600 °C, but also the temperature distribution in the substrate, influenced by the heater configuration used, and the oxygen content, i.e. argon mass flow, play a decisive role in terms of thin-film quality.

Although thin-film electrodes of crystallographically and morphologically sufficient quality were fabricated on the electrically conductive substrate Nb:STO (100), electrochemical investigations in cross-plane geometry in aqueous electrolyte (1M LiNO_3) were inconclusive. In addition to the high contact resistance to platinum, which was used for contacting on the part of the liquid cell, TEM analyses revealed that interdiffusion occurs during high-temperature deposition of LFP on STO. The resulting porous intermediate layer affects the electrical material properties of the system. This phenomenon can presumably be counteracted by using a buffer layer.

As an alternative electrically conductive substrate, among others, a system composed of STO|LNCO was designed, which was intended to solve the contact problem with platinum in the cross-plane setup. The investigation by means of cyclic voltammetry demonstrated that for the first time an electrochemically active LFP layer could be achieved. Not yet known at this point, LNCO presumably served as the above-mentioned buffer layer. This result serves as an essential reference point for further research in this field.

Nevertheless, to circumvent the difficulties of cross-plane measurements in aqueous electrolyte, platinum finger microelectrodes were applied by photolithography on a defined LFP layer (~50 nm) on STO (100) and investigated using a microcontact setup. In-plane impedance measurements were performed under argon atmosphere at temperatures ranging from room temperature to 450 °C.

These results demonstrate that the LFP system exhibits a very high total resistance of $\sim 10^{11} \Omega$ at room temperature and only one impedance semicircle is discernible. Measurements at higher temperatures revealed that not only is the total resistance reduced as expected, $< 10^6 \Omega$ at 450 °C, but also a low-frequency semicircle emerges, which is caused by an ionic contribution to the overall conductivity. This allows a separate examination of electronic and ionic transport properties. From the determined conductivities at different temperatures, the activation energies could be calculated for the total conductivity and separately for the electron and ion conductivity. The absolute values of the electronic conductivity in these thin-films are in good agreement with literature data for single crystals, while the ionic conductivity turns out to be higher in the thin-films, compared to single crystals.

These in-plane impedance measurements have the significant disadvantage that a control of Li-stoichiometry of the LFP compound is not an option. To make this feasible, the focus needs therefore to be on cross-plane studies. Initial findings outside the scope of this thesis show that, on the one hand, the contact resistance to Nb:STO can be reduced by using stainless steel instead of platinum. Furthermore, investigations in organic electrolytes are advantageous due to the higher stability compared to aqueous electrolytes, especially in the low potential range, i.e. in the region of the rest potential of LFP (~ 3.45 V vs. Li/Li⁺).

As already mentioned, the application of a suitable electrically conductive interlayer can on the one hand counteract interdiffusion and on the other hand enable electrochemical characterisation of the LFP thin-film electrode.

List of Abbreviations

AC	Alternating Current
CE	Counter Electrode
CPE	Constant-Phase Element
CV	Cyclic Voltammetry
DC	Direct Current
EDX	Energy Dispersive X-Ray Analysis
EIS	Electrochemical Impedance Spectroscopy
EV	Electric Vehicle
FIB	Focused Ion-Beam
GHG	Greenhouse Gas
GID	Grazing Incidence
HAADF	High-Angle Annular Dark-Field
LFP	LiFePO ₄
LIB	Lithium-Ion Battery
LMB	Lithium Metal Battery
LNCO	LaNi _{0.5} Co _{0.5} O ₂
LSF	La _{0.6} Sr _{0.4} FeO ₃
MFC	Mass-Flow Controller
MIEC	Mixed Ionic-Electronic Conductor
Nb:STO	Niobium doped SrTiO ₃
OCV	Open Circuit Voltage
PEIS	Potentiostatic Electrochemical Impedance Spectroscopy
PLD	Pulsed Laser Deposition
PVD	Physical Vapour Deposition
RE	Reference Electrode
RF	Radio Frequency
RT	Room Temperature
sccm	Standard Cubic Centimeters per Minute

List of Abbreviations

SE	Secondary Electrons
SEM	Scanning Electron Microscopy
SRO	SrRuO ₃
STEM	Scanning Transmission Electron Microscopy
STO	SrTiO ₃
TEM	Transmission Electron Microscopy
USTEM	University Service Facility for Transmission Electron Microscopy
WE	Working Electrode
XRC	X-Ray Centre
XRD	X-Ray Diffraction
YSZ	Yttrium-stabilised Zirconia

List of Figures

Figure 1.1: Schematic illustration of a typical lithium-ion battery. [11]	2
Figure 1.2: Crystal structure of LiFePO_4 . [27]	6
Figure 1.3: Arrhenius plot for electronic (left) and ionic (right) conductivity for nominally pure LiFePO_4 [27].....	7
Figure 1.4: Phase distribution diagrams of LiFePO_4 . [31].....	8
Figure 2.1: Illustration of the Randles circuit (a) [39] and simulated impedance spectra of the model (b).	13
Figure 2.2: Generalised equivalent circuit for a mixed ionic and electronic conductor.	14
Figure 2.3: Schematic illustration of magnetron sputter target. 1 – target, 2 – magnetic circuit, 3 – erosion zone.	16
Figure 2.4: Schematic illustration of a Schottky contact of a metal and a n-type semiconductor. Φ_B – barrier height, E_F – Fermi-niveau, E_C – lower level of the conduction band, E_v – upper level of the valence band. [52].....	17
Figure 3.1: Schematic illustration of the different heating units. (a) Corundum sample stage, on top of meandering platinum wire (heater-type A). (b) Fused silica disc, with wound platinum spiral (heater-type B/C). 1 – corundum sample holder, 2 – platinum wire, 3 – fused silica disc, 4 – platinum spiral	19
Figure 3.2: Schematic illustration of cross-plane and in-plane measurement geometry	29
Figure 3.3: Schematic representation of the "liquid cell". RE – reference electrode, CE – counter electrode, WE – working electrode, 1 – platinum wire, 2 – separator, 3 – beaker, 4 – aqueous electrolyte	30
Figure 3.4: Transmission line equivalent circuit for electrolyte MIEC electrode, derived from figure 2.2.	32
Figure 3.5: Schematic illustration of the microcontact measurement setup. 1 – microscope, 2 – adjustable micromanipulator with gold-plated steel needle, 3 – platinum electrode, 4 – LFP thin-film on substrate, 5 – heating stage	33
Figure 3.6: Workflow of ion beam etching photolithography (left) and fabricated platinum microelectrodes (right).....	34
Figure 3.7: Transmission line equivalent circuit for electrode MIEC electrode, derived from figure 2.2.	36
Figure 4.1: Image of an LFP layer deposited at 650 °C on Al_2O_3 (0001) taken via an optical light microscope.	37
Figure 4.2: Comparison of X-Ray diffractograms of LFP deposited on Al_2O_3 for different deposition temperatures. Reflexes originating from LFP are indicated by the dotted lines.....	38

Figure 4.3: X-Ray diffractograms of LFP deposited on Al_2O_3 for deposition temperatures of 550 °C (red) and 500 °C (black), respectively. Reflexes originating from the substrate are marked with (*), while (s) is assigned to LFP and (°) to FePO_4 .	39
Figure 4.4: Diffractograms of LFP deposited on STO (100) (550 °C) for deposition times of 120 (black), 60 (red) and 20 min (green) . The symbols indicate the reflexes of the respective phases : () – LFP, Δ – Fe_2O_3 .	41
Figure 4.5: Diffractogram of LFP deposited on STO (100) (60 min) at a deposition temperature of 550 °C. The symbols indicate the reflexes of the respective phases : () – LFP, s – substrate, Δ – Fe_2O_3 .	41
Figure 4.6: SEM images of LFP layers on STO (100) at (a) 120 min and (b) 60 min deposition time.	42
Figure 4.7: Optical light microscope images of LFP layer deposited at 550 °C calibrated substrate temperature on STO (100) using two different heater setups. These are corundum heater, with meandering platinum wire underneath (a) and a wound platinum spiral with a sample stage made of fused silica disc (b).	43
Figure 4.8: Diffractogram of LFP deposited on STO (100) (550 °C, 60 min) using different heater setups. The red line indicates the sample made on the corundum heating element and the black line the one fabricated on the heater using a fused silica disc as a sample stage. () – LFP, Δ – Fe_2O_3 .	44
Figure 4.9: Diffraction patterns of LFP deposited on STO (100) (600 °C) with an argon flow of 15 sccm (black) and 50 sccm (red) respectively. (b) represents an enlarged section of the relevant area of the diffractogram (a). () – LFP, s – substrate, Δ – Fe_2O_3 .	45
Figure 4.10: SEM images of LFP thin films deposited on STO (100) at 600 °C with an argon flow of (a) 15 sccm and (b) 50 sccm, respectively.	45
Figure 4.11: Diffraction patterns of LFP deposited on STO (100) at temperatures of 550 (black), 600 (red) and 625 °C (green) for 60 min, respectively. () – LFP, Δ – Fe_2O_3 .	46
Figure 4.12: Optical light microscope (a, b) and SEM (c, d) images of LFP thin films deposited on STO (100) (60min) at 550 °C and 600 °C.	47
Figure 4.13: LFP samples deposited on STO (100) ($5 \times 5 \text{ mm}^2$) at 625 °C with shadow mask (a) to keep edges clear and without shadow mask (b).	48
Figure 4.14: Diffractogram of samples prepared on STO (100) ($5 \times 5 \text{ mm}^2$) at 625 °C with and without shadow mask (a) and SEM image of the layer with shadow mask (b). () – LFP, Δ – Fe_2O_3 .	49
Figure 4.15: LFP deposited on STO (110) ($5 \times 5 \text{ mm}^2$) single crystals at 550 and 600 °C. Reflexes marked with (s) indicate the substrate. Further features could not be assigned to distinct phases.	50

Figure 4.16: Optical light microscope images of samples deposited on STO (110) (5x5 mm ²) at 550 °C (a) and 600 °C (b).	51
Figure 4.17: Diffractograms of LFP deposited on Nb:STO (100) (5x5 mm ²) at 550 °C for 20 (red) and 60 min (black), respectively. () – LFP, Δ – Fe ₂ O ₃	52
Figure 4.18: Light microscope (a) and SEM (b) images of LFP deposited on Nb:STO (100) at 550 °C for 60 min.	53
Figure 4.19: Diffraction pattern of LFP deposited on Pt LNCO Nb:STO (100) (10x10 mm) at 550 °C (black) and after annealing for 2h at 650 °C under sputter conditions (red). () – LFP, Δ – Fe ₂ O ₃	54
Figure 4.20: Light microscope (a) and SEM (b) images of LFP deposited on Nb:STO (100) at 550 and then annealed for 2h at 650 °C under sputter conditions.....	55
Figure 4.21: Diffraction patterns of SRO deposited (via PLD) on STO (100) (5x5 mm) (red line) and LFP deposited on STO SRO at 550 °C (black). Peaks originating from platinum paste are indicated with ◇. * – LFP	55
Figure 4.22: Non-ambient temperature XRD measurements of SRO on STO (100) conducted under argon atmosphere for 25-700 °C. The T-profile of the measurement programme is depicted in Fig. 4.24, where each colour represents the corresponding temperature.....	57
Figure 4.23: Temperature profile for non-ambient XRD measurements of SRO and LNCO, respectively on STO (100). The colour-coded plateaus indicate the respective measuring temperatures.	57
Figure 4.24: Non-ambient temperature XRD measurements of LNCO on STO (100) performed under argon atmosphere. Displayed are diffractograms of starting point (black) and end point (green) at 25 °C. The temperature profile is shown in figure 4.23.....	58
Figure 4.25: Light microscope (a) and SEM (b) images of LFP deposited on STO (110) LNCO at a deposition temperature of 550 °C for 77 min.	59
Figure 4.26: X-Ray diffractogram of LFP deposited on STO (110) LNCO at 550 °C measured in Bragg-Brentano (black) and grazing incidence (GID, red) geometry, respectively. ◇ – Pt, * – LFP	60
Figure 4.27: SEM images of LFP deposited on glassy carbon for 120 min. (a) shows an image taken at the rim of the substrate and (b) a magnification with measured LFP droplet. Droplets with structural features are highlighted in red.....	61
Figure 4.28: Diffractogram of LFP deposited on glassy carbon (10x10 mm ²) at 650 °C for 120 min. * – LFP.....	62
Figure 4.29: LFP deposited on Al ₂ O ₃ Pt at 550 °C for 120 min. The black line indicates the diffractogram of the substrate (Al ₂ O ₃ Pt), while the red line reflects the pattern after deposition of LFP. * – LFP	62

Figure 4.30: Image of LFP deposited on Al ₂ O ₃ Pt at a deposition temperature of 550 °C for 120 min, taken via optical light microscope.....	63
Figure 4.31: Images of LFP thin-film on STO (a, c, d) /Nb:STO (b) in cross-section, taken via SEM.....	64
Figure 4.32: TEM images of Nb:STO LFP cross-section (a) and colour-coded enlargements of selected areas (c-d).....	66
Figure 4.33: HAADF STEM image of Nb:STO LFP with highlighting of the selected areas for EDX elemental mapping analysis (blue rectangle) and line scan (red line).....	67
Figure 4.34: EDX maps for relevant elements, representing elemental distribution in the selected area. (cf. 4.33)	68
Figure 4.35: EDX line scans of relevant elements in the selected domain. (cf. 4.33).....	69
Figure 4.36: Magnification of the EDX line scans from figure 4.35 for the range 160-200 nm.....	69
Figure 4.37: Electrochemical stability range of LiNO ₃ (1M in H ₂ O). Potential of LFP vs. Li/Li ⁺ is highlighted.....	71
Figure 4.38: Charging or discharging step of an exemplary LFP sample on STO(100) SRO with I _{CD} = 500 nA.....	73
Figure 4.39: Cyclic voltammogram of LFP on STO(110) LNCO with a scan-rate of 0.05 and 0.01 mV/s respectively. Oxidative (green) and reductive (red) peaks corresponding to LFP are highlighted.....	73
Figure 4.40: Impedance spectrum of an exemplary LFP sample on STO(110) LNCO.....	75
Figure 4.41: (a) Arrangement of the platinum finger electrodes on the sample surface. (b) SEM image of an electrode with a finger spacing of 10 μm, with contact points marked in orange.....	76
Figure 4.42: Scatter of the impedance of a microelectrode with a finger spacing of 15 μm measured at room temperature	77
Figure 4.43: Spread of the determined total normalised conductivity with respect to the type of microelectrode, displayed for room temperature (a) and 450 °C (b).....	78
Figure 4.44: Microelectrode with drawn-in meander length (dotted line).....	78
Figure 4.45: Impedance spectra of the same microelectrode with a finger spacing of 15 μm at room temperature (a), 200 °C (b), 350 °C (c) and 450 °C (d).....	79
Figure 4.46: Magnification of the feature at low frequencies in impedance spectra recorded at 200 °C	80
Figure 4.47: Representation of the low-frequency semicircle of an impedance measurement at 450 °C (enlarged from 4.41 d). The AC and DC resistance are labelled with blue and green arrows, respectively.	80

Figure 4.48: Arrhenius plot of total conductivity, with colour coding of data obtained by different types of electrodes. The error bars displayed represent the standard deviation.....81

Figure 4.49: Arrhenius plots obtained from measured data for electronic (a) and ionic (b) conductivity, with colour coding for different types of electrodes. Plots (c) and (d) (electronic resp. ionic conductivity) allow visual comparison of the values obtained with the literature. (Maier et al. (2014) [27]).....82

List of Tables

Table 1.1: Characteristics of conventional anode and cathode materials.[9, 15-17]	4
Table 3.1: Parameters for deposition of LFP on Al ₂ O ₃ single crystals.....	21
Table 3.2: Parameters for deposition of LFP on STO single crystals.....	22
Table 3.3: Parameters for deposition of LFP on Nb:STO single crystals.....	22
Table 3.4: Parameters for deposition of platinum (200 nm).....	24
Table 3.5: Parameters for deposition of LFP on STO (110) LNCO and STO (100) LNCO.	24
Table 3.6: Parameters for deposition of LFP on STO SRO.....	25
Table 3.7: Parameters for PLD deposition of SRO and LNCO.....	25
Table 3.8: Parameters for deposition of LFP on glassy carbon.	26
Table 3.9: Parameters for deposition of titan and platinum.....	27
Table 3.10: Parameters for deposition of LFP on platinum.....	27
Table 3.11: Parameters used for photolithography	35
Table 3.12: Parameters used for ion beam etching.....	35

Bibliography

- [1] D.-G. f. C. A. European Commission, "Stepping up Europe's 2030 climate ambition Investing in a climate-neutral future for the benefit of our people.," 2020.
- [2] S.-G. European Commission, "'Fit for 55': delivering the EU's 2030 Climate Target on the way to climate neutrality.," 2021.
- [3] E. E. Agency, "Trends and drivers of EU greenhouse gas emissions.," EEA Report 2020, doi: 10.2800/19800.
- [4] E. E. Agency, "Monitoring CO₂ emissions from passenger cars and vans in 2018," EEA Report 2020, doi: 10.2800/19757.
- [5] G. Erbach, "Energy storage and sector coupling," *EPRS*, 2019.
- [6] E. Commission, "Energy storage – the role of electricity," 2017.
- [7] T. D. Tsiropoulos I., Lebedeva N., "Li-ion batteries for mobility and stationary storage applications – Scenarios for costs and market growth," *Publications Office of the European Union*, 2018, doi: 10.2760/87175.
- [8] E. Commission, "EUROPE ON THE MOVE Sustainable Mobility for Europe: safe, connected and clean," 2018.
- [9] J.-K. Park, *Principles and Applications of Lithium Secondary Batteries*. Wiley-VCH, 2012.
- [10] M. Armand and J.-M. Tarascon, "Building better batteries," *Nature*, vol. 451, pp. 652-657, 2018.
- [11] H. Lee, M. Yanilmaz, O. Toprakci, K. Fu, and X. Zhang, "A review of recent developments in membrane separators for rechargeable lithium-ion batteries," *Energy Environ. Sci.*, vol. 7, no. 12, pp. 3857-3886, 2014, doi: 10.1039/c4ee01432d.
- [12] C. Julien, A. Mauger, A. Vijh, and K. Zaghib, *Lithium Batteries: Science and Technology*. Springer International Publishing, 2016.
- [13] G. Zubi, R. Dufo-López, M. Carvalho, and G. Pasaoglu, "The lithium-ion battery: State of the art and future perspectives," *Renewable and Sustainable Energy Reviews*, vol. 89, pp. 292-308, 2018, doi: 10.1016/j.rser.2018.03.002.
- [14] A. Manthiram, "An Outlook on Lithium Ion Battery Technology," *ACS Cent Sci*, vol. 3, no. 10, pp. 1063-1069, Oct 25 2017, doi: 10.1021/acscentsci.7b00288.
- [15] M. Armand, P. Axmann, D. Bresser, M. Copley, K. Edström, C. Ekberg, D. Guyomard, B. Lestriez, P. Novák, M. Petranikova, W. Porcher, S. Trabesinger, M. Wohlfahrt-Mehrens, and H. Zhang, "Lithium-ion batteries – Current state of the art and anticipated developments," *Journal of Power Sources*, vol. 479, pp. 1-26, 2020, Art no. 228708, doi: 10.1016/j.jpowsour.2020.228708.
- [16] A. M. Science, "Nanomaterials for Energy Conversion and Storage," *Material Matters™*, vol. 7, no. 4, 2012.
- [17] M. Li, J. Lu, Z. Chen, and K. Amine, "30 Years of Lithium-Ion Batteries," *Adv Mater*, vol. 30, pp. 1-24, 2018, Art no. 1800561, doi: 10.1002/adma.201800561.

- [18] L. Croguennec and M. R. Palacin, "Recent achievements on inorganic electrode materials for lithium-ion batteries," *J Am Chem Soc*, vol. 137, no. 9, pp. 3140-56, Mar 11 2015, doi: 10.1021/ja507828x.
- [19] R. Younesi, G. M. Veith, P. Johansson, K. Edström, and T. Vegge, "Lithium salts for advanced lithium batteries: Li-metal, Li-O₂, and Li-S," *Energy & Environmental Science*, vol. 8, no. 7, pp. 1905-1922, 2015, doi: 10.1039/c5ee01215e.
- [20] A. K. Padhi, K. S. Nanjundaswamy, and J. B. Goodenough, "Phospho-olivines as Positive-Electrode Materials for Rechargeable Lithium Batteries," *Journal of The Electrochemical Society*, vol. 144, 1997.
- [21] Z. Ruopeng, X. Shouhong, Z. Qing, S. Chunran, and W. Huanwei, "Review on electrochemical energy storage technology in power system and relevant materials," *IOP Conference Series: Earth and Environmental Science*, vol. 829, 012004, 2021.
- [22] J. Wang and X. Sun, "Olivine LiFePO₄: the remaining challenges for future energy storage," *Energy & Environmental Science*, vol. 8, no. 4, pp. 1110-1138, 2015, doi: 10.1039/c4ee04016c.
- [23] C. M. Schwarzer, "Elektroautos: Die Budget-Batterie," *ZEIT ONLINE*, 2021.
- [24] R. Amin, P. Balaya, and J. Maier, "Anisotropy of Electronic and Ionic Transport in LiFePO₄ Single Crystals," *Electrochemical and Solid-State Letters*, vol. 10, no. 1, 2007, doi: 10.1149/1.2388240.
- [25] R. Malik, A. Abdellahi, and G. Ceder, "A Critical Review of the Li Insertion Mechanisms in LiFePO₄ Electrodes," *Journal of The Electrochemical Society*, vol. 160, no. 5, pp. A3179-A3197, 2013, doi: 10.1149/2.029305jes.
- [26] R. Malik, D. Burch, M. Bazant, and G. Ceder, "Particle size dependence of the ionic diffusivity," *Nano Lett*, vol. 10, no. 10, pp. 4123-7, Oct 13 2010, doi: 10.1021/nl1023595.
- [27] M. Gaberšček;, J. Jamnik;, K. Weichert;, D. Samuelis;, and J. Maier, "LiFePO₄: From an Insulator to a Robust Cathode Material," *Pan Stanford Publishing* pp. 259-297, 2014.
- [28] R. Amin, J. Maier, P. Balaya, D. P. Chen, and C. T. Lin, "Ionic and electronic transport in single crystalline LiFePO₄ grown by optical floating zone technique," *Solid State Ionics*, vol. 179, no. 27-32, pp. 1683-1687, 2008, doi: 10.1016/j.ssi.2008.01.079.
- [29] A. Van der Ven and M. Wagemaker, "Effect of surface energies and nano-particle size distribution on open circuit voltage of Li-electrodes," *Electrochemistry Communications*, vol. 11, no. 4, pp. 881-884, 2009, doi: 10.1016/j.elecom.2009.02.015.
- [30] J. Maier and R. Amin, "Defect Chemistry of LiFePO₄," *Journal of The Electrochemical Society*, vol. 155, no. 4, 2008, doi: 10.1149/1.2839626.
- [31] C. Delacourt, P. Poizot, J.-M. Tarascon, and C. Masquelier, "The existence of a temperature-driven solid solution in Li_xFePO₄ for 0 ≤ x ≤ 1," *Nature Materials*, vol. 4, no. 3, pp. 254-260, 2005, doi: 10.1038/nmat1335.
- [32] J. L. Dodd, R. Yazami, and B. Fultz, "Phase Diagram of Li_xFePO₄," *Electrochemical and Solid-State Letters*, vol. 9, no. 3, 2006, doi: 10.1149/1.2164548.

- [33] H. Raj, S. Rani, and A. Sil, "Two-Phase Composition (LiFePO₄/FePO₄) and Phase Transformation Dependence on Charging Current: In Situ and Ex Situ Studies," *Energy & Fuels*, vol. 34, no. 11, pp. 14874-14881, 2020, doi: 10.1021/acs.energyfuels.0c02455.
- [34] C. Delmas, M. Maccario, L. Croguennec, F. Le Cras, and F. Weill, "Lithium deintercalation in LiFePO₄ nanoparticles via a domino-cascade model," *Nat Mater*, vol. 7, no. 8, pp. 665-71, Aug 2008, doi: 10.1038/nmat2230.
- [35] V. Srinivasan and J. Newman, "Existence of Path-Dependence in the LiFePO₄ Electrode," *Electrochemical and Solid-State Letters*, vol. 9, no. 3, 2006, doi: 10.1149/1.2159299.
- [36] D. Li, T. Zhang, X. Liu, P. He, R. Peng, M. Wang, M. Han, and H. Zhou, "A hybrid phase-transition model of olivine LiFePO₄ for the charge and discharge processes," *Journal of Power Sources*, vol. 233, pp. 299-303, 2013, doi: 10.1016/j.jpowsour.2013.01.133.
- [37] D. Li and H. Zhou, "Two-phase transition of Li-intercalation compounds in Li-ion batteries," *Materials Today*, vol. 17, no. 9, pp. 451-463, 2014, doi: 10.1016/j.mattod.2014.06.002.
- [38] C. Knoblauch, "Impedanzspektroskopie – Ein Überblick von der Theorie bis zur Anwendung," *WOMag*, vol. 4, no. 9, pp. 31-39, 2015.
- [39] C. Ho, I. D. Raistrick, and R. A. Huggins, "Application of A-C Techniques to the Study of Lithium Diffusion in Tungsten Trioxide Thin Films," *Journal of The Electrochemical Society*, vol. 127, no. 2, pp. 343-350, 1980/02/01 1980, doi: 10.1149/1.2129668.
- [40] W. Lai and S. M. Haile, "Impedance Spectroscopy as a Tool for Chemical and Electrochemical Analysis of Mixed Conductors: A Case Study of Ceria," *Journal of the American Ceramic Society*, vol. 88, no. 11, pp. 2979-2997, 2005, doi: 10.1111/j.1551-2916.2005.00740.x.
- [41] J. Hong, C. Wang, N. J. Dudney, and M. J. Lance, "Characterization and Performance of LiFePO₄ Thin-Film Cathodes Prepared with Radio-Frequency Magnetron-Sputter Deposition," *Journal of The Electrochemical Society*, vol. 154, no. 8, pp. A805-A809, 2007, doi: 10.1149/1.2746804.
- [42] J. Wu, W. Cai, and G. Shang, "In situ Electrochemical-AFM Study of LiFePO₄ Thin Film in Aqueous Electrolyte," *Nanoscale Res Lett*, vol. 11, no. 1, p. 223, Dec 2016, doi: 10.1186/s11671-016-1446-1.
- [43] J. Xie, N. Imanishi, T. Zhang, A. Hirano, Y. Takeda, and O. Yamamoto, "Li-ion diffusion kinetics in LiFePO₄ thin film prepared by radio frequency magnetron sputtering," *Electrochimica Acta*, vol. 54, no. 20, pp. 4631-4637, 2009, doi: 10.1016/j.electacta.2009.03.007.
- [44] X.-J. Zhu, L.-B. Cheng, C.-G. Wang, Z.-P. Guo, P. Zhang, G.-D. Du, and H.-K. Liu, "Preparation and Characteristics of LiFePO₄ Thin Film by Radio Frequency Magnetron Sputtering for Lithium Microbatteries," *The Journal of Physical Chemistry C*, vol. 113, no. 32, pp. 14518-14522, 2009/08/13 2009, doi: 10.1021/jp902560q.

- [45] A. Baptista, F. Silva, J. Porteiro, J. Míguez, and G. Pinto, "Sputtering Physical Vapour Deposition (PVD) Coatings: A Critical Review on Process Improvement and Market Trend Demands," *Coatings*, vol. 8, no. 11, pp. 1-22, 2018, Art no. 402, doi: 10.3390/coatings8110402.
- [46] R. D. A. P.J. Kelly, "Magnetron sputtering: a review of recent developments and applications," *Vacuum*, vol. 56, pp. 159-172, 2000.
- [47] R. T. Tung, "The physics and chemistry of the Schottky barrier height," *Applied Physics Reviews*, vol. 1, pp. 1-54, 2014, Art no. 011304, doi: 10.1063/1.4858400.
- [48] A. Tsurumaki-Fukuchi, Y. Tsuta, M. Arita, and Y. Takahashi, "Controlled Current Transport in Pt/Nb:SrTiO₃ Junctions via Insertion of Uniform Thin Layers of TaO_x," *physica status solidi (RRL) – Rapid Research Letters*, vol. 13, no. 7, pp. 1-5, 2019, Art no. 1900136, doi: 10.1002/pssr.201900136.
- [49] R. Schafranek, S. Payan, M. Maglione, and A. Klein, "Barrier height at(Ba,Sr)TiO₃/Pt interfaces studied by photoemission," *Physical Review B*, vol. 77, no. 19, pp. 1-13, 2008, Art no. 195310, doi: 10.1103/PhysRevB.77.195310.
- [50] N. Ohashi, H. Yoshikawa, Y. Yamashita, S. Ueda, J. Li, H. Okushi, K. Kobayashi, and H. Haneda, "Determination of Schottky barrier profile at Pt/SrTiO₃:Nb junction by x-ray photoemission," *Applied Physics Letters*, vol. 101, no. 25, pp. 1-5, 2012, Art no. 251911, doi: 10.1063/1.4772628.
- [51] Z. Li, S. Yasui, S. Takeuchi, A. Creuziger, S. Maruyama, A. A. Herzing, I. Takeuchi, and L. A. Bendersky, "Structural study of epitaxial LiCoO₂ films grown by pulsed laser deposition on single crystal SrTiO₃ substrates," *Thin Solid Films*, vol. 612, pp. 472–482, 2016, doi: 10.1016/j.tsf.2016.05.017.
- [52] "Schottky barrier: Wikipedia." https://en.wikipedia.org/wiki/Schottky_barrier#/media/File:Schottky_barrier_zero_bias.svg (accessed 07.09.2021).
- [53] J. Jamnik and J. Maier, "Treatment of the Impedance of Mixed Conductors: Equivalent Circuit Model and Explicit Approximate Solutions," *Journal of The Electrochemical Society*, vol. 146, no. 11, pp. 4183-4188, 1999.
- [54] J. Jamnik and J. Maier, "Generalised equivalent circuits for mass and charge transport: chemical capacitance and its implications," *Physical Chemistry Chemical Physics*, vol. 3, no. 9, pp. 1668-1678, 2001, doi: 10.1039/b100180i.
- [55] A. Nennung, L. Volgger, E. Miller, L. V. Mogni, S. Barnett, and J. Fleig, "The Electrochemical Properties of Sr(Ti,Fe)O_{3.8} for Anodes in Solid Oxide Fuel Cells," *Journal of The Electrochemical Society*, vol. 164, no. 4, pp. F364-F371, 2017, doi: 10.1149/2.1271704jes.
- [56] P. He, X. Zhang, Y.-G. Wang, L. Cheng, and Y.-Y. Xia, "Lithium-Ion Intercalation Behavior of LiFePO₄ in Aqueous and Nonaqueous Electrolyte Solutions," *Journal of The Electrochemical Society*, vol. 155, no. 2, pp. A144-A150, 2008, doi: 10.1149/1.2815609.
- [57] H. C. Shin, W. I. Cho, and H. Jang, "Electrochemical properties of the carbon-coated LiFePO₄ as a cathode material for lithium-ion secondary batteries," *Journal of Power Sources*, vol. 159, no. 2, pp. 1383-1388, 2006, doi: 10.1016/j.jpowsour.2005.12.043.

- [58] N. Dupré, M. Cuisinier, Y. Zheng, V. Fernandez, J. Hamon, M. Hirayama, R. Kanno, and D. Guyomard, "Evolution of LiFePO_4 thin films interphase with electrolyte," *Journal of Power Sources*, vol. 382, pp. 45-55, 2018, doi: 10.1016/j.jpowsour.2018.02.029.
- [59] J.-S. Lee, J. Fleig, J. Maier, D.-Y. Kim, and T.-J. Chung, "Local Conductivity of Nitrogen-Graded Zirconia," *Journal of the American Ceramic Society*, vol. 88, no. 11, pp. 3067-3074, 2005, doi: 10.1111/j.1551-2916.2005.00593.x.
- [60] J. Lee, J. Fleig, J. Maier, T. Chung, and D. Kim, "Microcontact impedance spectroscopy in nitrogen-graded zirconia," *Solid State Ionics*, vol. 176, pp. 1711-1716, 2005, doi: 10.1016/j.ssi.2005.04.036.